

Computational Modelling of  
Magneto-Hydrodynamic Mode  
Conversion in Sunspot  
Atmospheres



A thesis submitted for the degree of  
**Doctor of Philosophy**

by

**Carlos Jon Rijs**

B.Sc. (Hons)

Supervisor: Prof. Paul S. Cally

Associate Supervisor: Dr. Hamed Moradi

Monash Centre for Astrophysics

School of Mathematical Sciences

Monash University, Australia

September, 2016

© The author 2016. Except as provided in the Copyright Act 1968, this thesis may not be reproduced in any form without the written permission of the author.

# Contents

<b>I</b>	<b>MHD Waves and Sunspot Atmospheres</b>	<b>1</b>
<b>1</b>	<b>Introduction</b>	<b>2</b>
1.1	Photospheric Oscillations	3
1.2	Active Regions and Sunspot Models	6
1.2.1	Umbral/penumbral structure and magnetic features	6
1.2.2	Numerical modelling of sunspots	11
1.3	Helioseismic Inversions and their Successes	14
1.4	Waves in Magnetised Plasmas	17
1.4.1	The dispersion relation	18
1.4.2	Acoustic waves	20
1.4.3	Shear Alfvén waves.	20
1.4.4	Magneto-acoustic waves.	21
1.5	MHD Mode Conversion	22
1.5.1	Fast-slow mode conversion and transmission	22
1.6	Thesis Outline and Basis for this Research	25
<b>II</b>	<b>The Acoustic Halo</b>	<b>31</b>
<b>2</b>	<b>Simple Modelling of the Acoustic Halo</b>	<b>32</b>
2.1	Observations of the Acoustic Halo	32
2.2	Mechanisms for Halo Formation	39
2.2.1	Fast-slow MHD mode conversion as a halo mechanism	40
2.3	Forward Modelling with the SPARC Code	42

2.3.1	Sunspot atmospheres . . . . .	44
2.3.2	Geometry and boundary conditions . . . . .	47
2.3.3	A pulse wave driver . . . . .	47
2.3.4	Alfvén speed limiter . . . . .	51
2.4	Simulation Results . . . . .	52
2.4.1	Evidence of a halo . . . . .	53
2.4.2	Testing the hypothesis . . . . .	56
2.4.3	Spectral structure . . . . .	61
2.5	What Can We Conclude? . . . . .	64
<b>3</b>	<b>Distributed Source Simulations . . . . .</b>	<b>67</b>
3.1	Approximating the Photosphere with SPARC . . . . .	68
3.2	Extracting Observables . . . . .	72
3.3	Comparisons with Observations . . . . .	75
3.3.1	Spectral structure . . . . .	78
3.4	The Halo Formation Mechanism . . . . .	86
3.5	Fast-Alfvén Conversion and Halo Structure . . . . .	88
3.6	Discussion and Ramifications . . . . .	92
<b>III</b>	<b>Fast-Alfvén Conversion - A Twisted Approach . . . . .</b>	<b>97</b>
<b>4</b>	<b>Alfvén Waves in a Twisted Magnetic Field . . . . .</b>	<b>98</b>
4.1	Background Discussion . . . . .	99
4.1.1	Coronal wave observations . . . . .	99
4.1.2	Fast-Alfvén mode conversion and resonant absorption . . . . .	102
4.2	A Twisted Field Atmospheric Model . . . . .	108
4.2.1	The uniform twist magnetic field . . . . .	109
4.2.2	Density stratification and Alfvén speed . . . . .	112
4.2.3	Solving the equations of motion . . . . .	115
4.2.4	Geometry and boundary/initial conditions . . . . .	116

## CONTENTS

---

4.2.5	Preliminary ray-path calculations . . . . .	118
4.3	Simulation Results . . . . .	120
4.3.1	The parameter study and its goal . . . . .	120
4.3.2	Examining the fast wave . . . . .	123
4.3.3	Alfvén wave production . . . . .	125
4.4	A Summary and Discussion of Results . . . . .	139
<b>5</b>	<b>Concluding Remarks . . . . .</b>	<b>144</b>
5.1	The Acoustic Halo . . . . .	145
5.2	Fast-Alfvén Mode Conversion . . . . .	147

# Abstract

An enhancement in high-frequency time-averaged Doppler velocity and intensity Fourier power (with respect to quiet-Sun values) is commonly observed amongst the weak and highly inclined field around the penumbra of sunspots and active regions in the solar photosphere and chromosphere. This well documented phenomenon is known as the acoustic (or seismic) halo.

In this thesis we attempt to model the halo numerically by initiating 3D linear wave modelling in a realistic magneto-hydrostatic sunspot atmosphere. It is our goal to ascertain whether the formation of the acoustic halo in regions of moderate and inclined magnetic field is caused by the refraction and return of fast waves via fast-slow MHD mode conversion.

We begin (chapter 2) by initiating a very simple wavelet pulse source below the photospheric surface of our sunspot atmosphere and analysing the structure of the power enhancements that form. In this scenario we observe a strong halo-like enhancement that exhibits many observationally verified characteristics. In particular we find a strong spatial relationship between halo formation and the equipartition surface at which the Alfvén speed  $a$  matches the sound speed  $c$ . This is significant as the  $a = c$  layer is where the fast-slow mode conversion takes place and so this correlation lends weight to the mode conversion halo mechanism. It also explains the fact that the halo is seen to undergo a spreading with height.

In order to model halos that are directly comparable to observations we also utilise a realistic wave source, designed to mimic the wave bath of the solar photosphere (chapter 3). We directly compare these enhancements with multi-height SDO halo observations of an active region similar (in size and field strength) to our simulated sunspot. We find that these more realistic simulated halos are in good qualitative agreement with observations, except for the fact that the simulation halo magnitudes are consistently greater than those observed. We discuss at length why this may be the case. Significantly, in simulations (both in the pulse source and realistic stochastic source cases) where we have capped the atmospheric Alfvén speed such that waves are not permitted to refract and return downwards after reaching the  $a = c$  height, halos are non-existent; indeed the halo magnitude itself seems to be a

smooth function of the height at which the cap is implemented, which suggests that the power enhancement is wholly dependent on returning fast waves. In addition, we also find strong evidence that fast-Alfvén mode conversion plays a significant role in the structure of the halo, taking energy away from photospheric and chromospheric heights in the form of field-aligned Alfvén waves. This conversion process may explain the observed dual-ring halo structure that we see at higher ( $> 8$  mHz) frequencies.

Finally (chapter 4) we sidestep somewhat from the large-scale numerical to the semi-analytical regime. Here we investigate the efficiency of the fast-Alfvén mode conversion process in the chromosphere in the context of a simplified force-free *twisted* magnetic field in a gravitationally stratified cold plasma. The validity of Alfvén wave production at photospheric and chromospheric heights is a contested issue, and our simple study only aims to highlight the conditions under which the conversion is most efficient in the twisted field, stratified case.

We find that the production of the upwards-travelling Alfvén wave is maximised in the weakly twisted case where the field is largely vertical. However the conversion is identically zero in the case where the field is precisely vertical. The conversion is also strongly dependent on the wavevector-to-field attack angle ( $\phi$ ) when the wave reaches the fast wave reflection height, being maximised when  $\phi = 90^\circ$ . Finally, the upwards (field-aligned) Alfvén wave appears to be strongly favoured by fast waves with  $\phi < 90^\circ$ , i.e. with a component in the direction of the field, rather than against it. These results more or less match the conclusions of Cally & Hansen (2011) who conducted a similar parameter study in uniform *untwisted* field.

# General Declaration

## Monash University

### Declaration for thesis based or partially based on conjointly published or unpublished work

In accordance with Monash University Doctorate Regulation 17.2 Doctor of Philosophy and Research Masters regulations the following declarations are made:

I hereby declare that this thesis contains no material which has been accepted for the award of any other degree or diploma at any university or equivalent institution and that, to the best of my knowledge and belief, this thesis contains no material previously published or written by another person, except where due reference is made in the text of the thesis.

This thesis includes 2 original papers published in peer reviewed journals and 1 unpublished publication. The core theme of this thesis is mode conversion and its effects around solar active regions. The ideas, development and writing up of all the papers in the thesis were the principal responsibility of myself, the candidate, working within the School of Mathematical Sciences under the supervision of Prof. Paul S. Cally and Dr Hamed Moradi.

The inclusion of co-authors reflects the fact that this work came from active collaboration between researchers and acknowledges input into team-based research.

In the case of chapters 2-3 my contribution to the work involved the following:

Thesis chapter	Publication title	Publication status	Nature and extent of candidate's contribution
2	MHD Wave Refraction and the Acoustic Halo Effect Around Solar Active Regions: A 3D Study	Published, 2015 ApJ, 801, 27R	Key ideas, code development, produced all results, writing of the paper.
3	3D Simulations of Realistic Power Halos in Magnetohydrostatic Sunspot Atmospheres: Linking Theory and Observation	Published, 2016 ApJ, 817, 45R	Key ideas, code development, produced all results, writing of the paper.

I have renumbered sections of submitted or published papers in order to generate a consistent presentation within the thesis.

Carlos Jon Rijs

30/08/16

# Acknowledgements

I would firstly like to express my profound gratitude to my academic supervisors Prof Paul Cally and Dr Hamed Moradi. Their patience with me during the journey down this long and arduous road has been nothing short of extraordinary. It has been a real pleasure to learn from such world-class solar physicists over the course of my candidature.

To Nadia Turner – the person who has been in the unenviable position of living with a PhD student for the last 4 years – I am forever indebted to you, my love, for your constant support and wise words.

I am forever grateful to my father, Gerry, and my mother, Julie. I would (figuratively and literally) not be here without them and their support during a difficult last decade cannot be understated.

There are a host of others who encouraged and helped me along the way. My sincere thanks extends to Triloki Dash, Karl Scofield and Jools the dog and as well as all the music (from Tchaikovsky to Trent Reznor) that has sustained me for year after year. Finally all of my friends and associates at Monash really made the journey fly by: Dave Kinniburgh, David Martin, Tim Dolley, Kyle Talbot, Jacob Crossett, Amelia Fraser-McKelvie, Dane Kleiner, David Palamara, Nicolas Bonne, Rebecca Nealon, Chris Hanson, Leo Brewin, Simon Teague, Daniel Tokarev and of course, the members of the legendary and exclusive 500 club: Damien Przybylski, Steven Edwards, Chloe Lerebours, Joe Bunton, Simon Bowly and Calum Robertson. You guys are the best.

# Part I

## MHD Waves and Sunspot Atmospheres

# Chapter 1

## Introduction

The goal of this section is to introduce the basic physics of the photosphere and low-chromosphere of the Sun.

We begin in (§1.1) by describing the oscillations present on the observable solar surface, how they are observed and how they may be expressed mathematically.

In (§1.2) we move on to a discussion of the magnetic structures in the photosphere, including active regions and sunspots and how one may approach modelling them numerically, while (§1.3) describes some of the successes that helioseismic and forward modelling techniques have had in explaining the interactions of  $p$ -mode waves and active regions.

We then provide a mathematical treatment of the wave types present in the magnetised plasma of the photosphere (§1.4) before introducing the basic concepts of fast-slow MHD mode conversion (§1.5).

## 1.1 Photospheric Oscillations

Oscillations throughout the quiet (weakly magnetic) solar photosphere were originally shown by Leighton et al. (1962) to exhibit a broad spectral profile with a peak frequency of around  $\nu = \omega/2\pi = 3.3$  mHz. These five-minute period oscillations were subsequently shown to be standing waves (Leibacher & Stein, 1971) which were suggested to be driven by turbulent excitation from the sub-photospheric convection zone (Goldreich & Keeley, 1977).

Spatio-temporal fourier analysis of surface wave power later showed that oscillations also have discrete ridges in frequency-wavenumber space (Ulrich, 1970; Deubner, 1975). Such a discrete oscillation pattern suggests that very specific physics is in play regarding the geometry of the photospheric wave domain. Figure 1.1 shows a relatively recent example of these photospheric mode ridges both from ground and space-based observatories.

Physically, the sound waves are trapped in a cavity lying beneath the solar photosphere. The oscillations are bounded by the Lamb depth below, where the horizontal phase speed equals the sound speed. The downwards travelling waves will undergo refraction and eventually reflect back upwards as determined by the increasing sound-speed profile which forces the longitudinal pressure oscillations back to shallower depths. Wave propagation above the cavity is halted by the presence of the adiabatic acoustic cut-off frequency ( $\nu_c$ ) and is dependent on the wave frequency and wavenumber. The configuration results in standing wave oscillations at modes favoured by the geometry of the cavity, which is what we observe as the photospheric wave field.

The non-radial (normal) oscillations of a sphere can be characterised by a spherical harmonic degree ( $\ell$ ) and radial order ( $n$ ).  $\ell$  is proportional to the horizontal component of the wavenumber and roughly corresponds to how many wavelengths would be present around the circumference of the Sun. In general  $\ell^2 + n^2 = R_{\text{sun}}^2 k_h^2$  where  $R_{\text{sun}} \approx 6.955 \times 10^5$  km is the solar radius and  $k_h = \sqrt{k_x^2 + k_y^2}$  is the horizontal component of the wavenumber,  $k$  (where  $k = \sqrt{k_h^2 + k_z^2}$ ). For high  $\ell$  oscillations the expression simplifies to  $\ell \approx R_{\text{sun}} k_h$ , demonstrating a constant proportionality between the two quantities  $\ell$  and  $k_h$ .

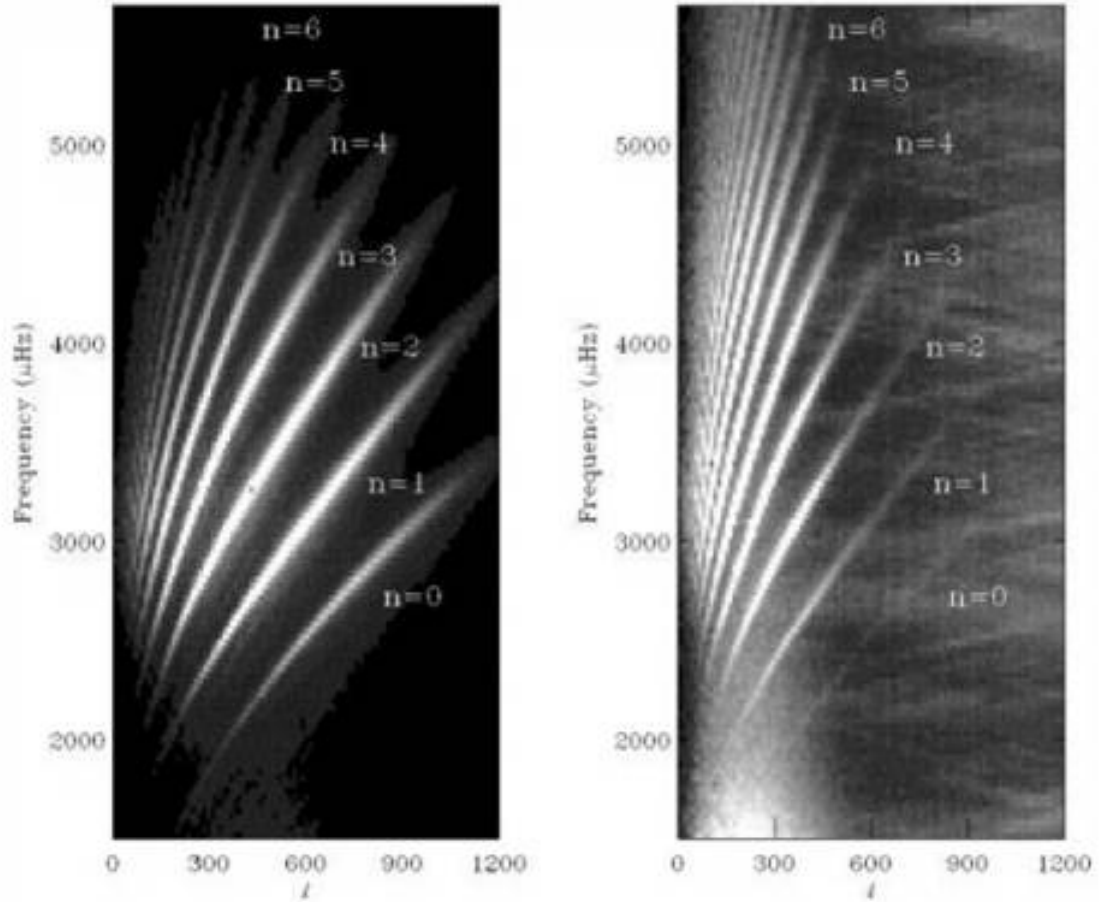


Figure 1.1: Azimuthally averaged power spectra in  $\nu$ - $\ell$  space from the *Michelson Doppler Imager* (MDI) onboard the *Solar and Heliospheric Observatory* (SOHO) (left panel) and from the ground-based *Taiwan Oscillation Network* (TON) (right panel) (Gonzalez Hernandez et al., 1998).

In contrast, the radial order  $n$  corresponds to the number of radial nodes of the oscillation. The ridges in figure 1.1 each correspond to a particular value of  $n$  which may have a range of values in  $\nu$ - $\ell$  (or equivalently  $\omega$ - $k_h$ ) space. The  $n = 0$  mode is known as the fundamental mode (or  $f$ -mode);  $f$ -modes are the typical ‘surface waves over deep water’ which are observable at the surface of most fluids (i.e. at the interface between two fluids of differing densities) under the force of gravity. These horizontally propagating waves are incompressible and have an exponentially decaying amplitude with depth - they are surface modes concentrated at the surface.

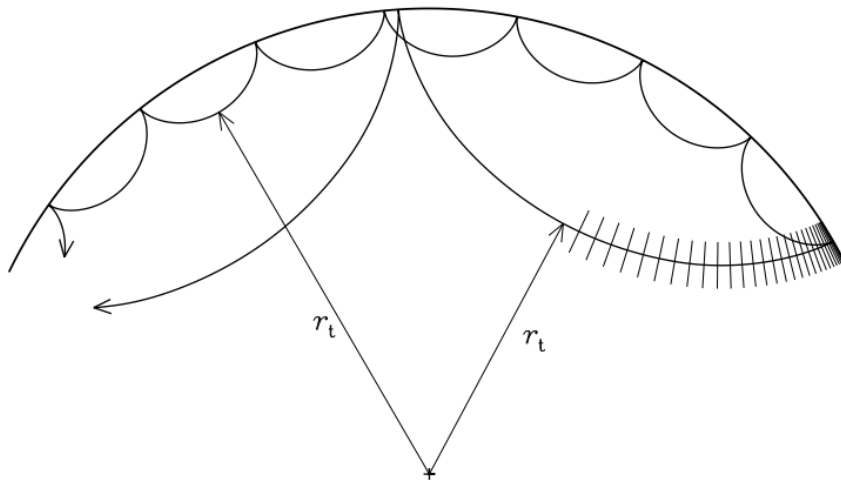


Figure 1.2: A simple sketch of the wave paths travelled by low- $\ell$  and high- $\ell$  waves (at the same frequency). The low- $\ell$  wave samples deeper into the interior. The lower turning point at  $r_t$  is the depth where  $k_z = 0$ . The waves are reflected back downwards by the acoustic cutoff (figure taken from ‘Lecture Notes on Stellar Oscillations’ by Christensen-Dalsgaard, J).

All of the other ridges for  $n \geq 1$  are the result of pressure modes (or  $p$ -modes).  $p$ -modes are pressure driven acoustic wave modes (modified by gravity and even the local magnetic field) and make up the bulk of the observable photospheric wavefield. In general lower  $\ell$  waves (at a given frequency) will sample deeper into the solar interior before being upwardly refracted due to the increasing sound speed caused by the gravitational stratification.

Figure 1.2 shows a simple schematic diagram of this behaviour very simply. Each ray corresponds to a wave of a single initial  $k$  and  $\nu$  value. The lower turning point ( $r_t$ ) is inversely proportional to  $k_h$  and is therefore dependent on the horizontal wavelength ( $\lambda_h = 2\pi/k_h$ ). This property is very useful to helioseismologists, as one may isolate waves that have sampled various depths by applying phase speed filters to time series observations in order to infer subsurface properties.

In general, photospheric oscillations exhibit amplitudes of around 0.1 - 0.2 km/s and increase in magnitude in inverse proportion to the density, reaching 0.4 - 0.5 km/s

in the low chromosphere (Priest, 1982). Although waves have a greater amplitude at chromospheric heights, there is generally much less wave energy at these heights, even though the 5-minute oscillation is still clearly present (in the lower chromosphere at least).

## 1.2 Active Regions and Sunspot Models

### 1.2.1 Umbral/penumbral structure and magnetic features

A sunspot is a surface manifestation of large-scale magnetic flux penetration through the photosphere of the sun and above. Strong magnetic fields inhibit the transfer of energy by convection, disrupting the normal granular pattern of the quiet sun and resulting in the cooler (and thus darker in intensity) regions seen in the photosphere. Sunspots in general manifest as part of larger *bipolar* magnetic active regions. Active regions indicate areas with one or more sunspots or a large amount of magnetic flux and solar activity.

In general these regions exist in a state of near-magneto-hydrostatic equilibrium, with the umbral magnetic pressure and gas pressure exerting a mechanical force on the surrounding field-free gas. A spot may remain stable for days, weeks or even months in this configuration as it rotates across the solar disk. The presence of the magnetic pressure leads to a gas pressure and density deficit in the sunspot umbra, along with the already reduced temperature. This deficit results in the well observed Wilson depression, i.e. the umbra is generally sunken with respect to the penumbra and the outer extent of the spot and as such the photosphere takes the form of a contour which can dip some hundreds of km in depth at its centre.

Topologically, a sunspot consists of the umbra, which is the central dark region where the field is strongest and most vertical, and the penumbra, the slightly brighter and more structured region sitting between the umbra and the regular granulation of the quiet-Sun. The brightness emanating from penumbral and umbral regions is reduced by around 25% and 75% respectively (with respect to the surrounding quiet-sun photosphere) (Jahn & Schmidt, 1994; Borrero & Ichimoto, 2011).

A typical sunspot is shown in figure 1.3, observed with the Swedish Solar

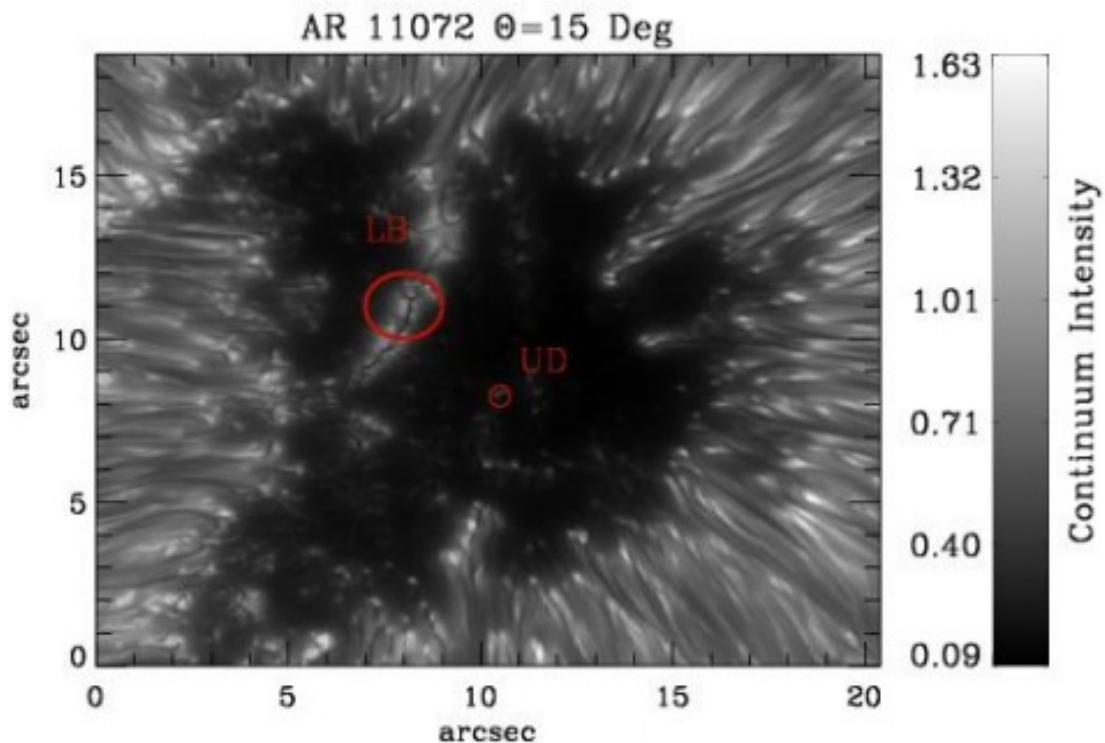


Figure 1.3: SST Ca  $H$  intensity image showing the umbra and penumbral boundary with some small-scale structure evident, including a light bridge and umbral dots (denoted in red) (Scharmer et al., 2011; Borrero & Ichimoto, 2011).

Telescope (SST) (Scharmer et al., 2011; Borrero & Ichimoto, 2011), with the penumbra exhibiting the well-known structure consisting of light *spines* and dark *intraspines* (Scharmer et al., 2002; Bellot Rubio et al., 2004). Spines exhibit a field vector which is strong and largely vertical, whereas the intraspines are more horizontal and significantly weaker in strength, with studies showing up to a  $60^\circ$  difference in field inclination between the filaments (Weiss et al., 2004; Thomas et al., 2006). The intraspines will generally form a canopy and then return to the solar surface whereas the spines may extend out to form coronal loops over the whole active region (Ruedi et al., 1998). This structure persists even after time averaging, suggesting that it is not a short lived phenomenon.

In order to fully resolve the filamentary structure, a spatial resolution of less than 0.5 arcsec is generally required. At coarser resolutions than this the penumbra appears as an essentially uniform region with a brightness somewhere in between

the granulation of the sun and the dark umbra. With a current resolution limit of around 0.3 arcsec, it has been shown that the striated pattern observed in the intensity continuum is also mirrored in both the magnetic field configuration and the velocity flow field (Title et al., 1993; Bellot Rubio, 2007). The plasma flow direction in the penumbra is primarily radially outward. That is, there is a small component of plasma velocity in the upward vertical direction at the inner penumbra boundary and a downward vertical component at the outer boundary (Schlichenmaier & Schmidt, 2000; Tritschler et al., 2004). This radially outward flow is known as the Evershed flow and was first observed by Evershed (1909).

Umbral dots (Danielson, 1964) are a feature which exist as bright points of around 0.5 to 0.7 Mm in size which lay in the otherwise dark sunspot umbra. Figure 1.3 shows several typical examples of these unexpected intensity enhancements. The dots are observed in nearly all sunspots and pores and can contribute between 10 and 20 % of the total umbral brightness (Sobotka et al., 1993). The dots have been shown to exhibit a significant temperature increase over the surrounding umbra of between 500 K (Grossmann-Doerth et al., 1986; Riethmüller et al., 2008) and 1500 K (Tritschler et al., 2004), while the magnetic field strength of the dots themselves has been problematic to obtain, with some studies reporting no difference relative to the umbra (Lites et al., 1989; Tritschler & Schmidt, 1997) and others finding a clear reduction (Wiehr & Degenhardt, 1993; Socas-Navarro et al., 2004; Riethmüller et al., 2008). Both the temperature and magnetic field measurements were shown in these studies to be extremely sensitive to the local optical depth however, with the temperature enhancement vanishing some 200 km above the surface  $\tau = 1$  layer. In any case, prominent upflows on the order of several hundred m/s in the proximity of the dots (Socas-Navarro et al., 2004; Rimmele, 2004; Bharti et al., 2007; Rimmele, 2008) would suggest that there are small-scale breakdowns in the magnetic field structure around the umbral dots and convection is free to transport heat and energy to the surface in a similar manner to the mechanism that drives the quiet-Sun.

Light bridges are somewhat larger structures than umbral dots and may be visible in some sunspots as a bridge of bright material that divides a single umbra into two separate parts. A light bridge is also shown in figure 1.3 and the objects seem to share some similarities with umbral dots. Recent observations suggest fine

structure with upflows in the dark central regions and downflows in the slightly brighter outer regions (Hirzberger et al., 2002; Berger & Berdyugina, 2003; Rouppe van der Voort et al., 2010).

### Measuring magnetic structure

Magnetic fields are generally observationally inferred by measuring the Zeeman splitting of spectral lines, a process first performed by Hale (1908). In the modern era of spaced-based observations, the full field vector  $\mathbf{B}$  is also obtainable via integration of the radiative transfer equation (RTE). The solution to the RTE is the Stokes vector for a given wavelength, which is a function of the physical parameters of the atmosphere, including the optical depth. Solving the RTE is non-trivial, and tackling the equation has involved work over many decades (Beckers, 1969; Stenflo, 1971; Rees et al., 1989; Bellot Rubio et al., 1998).

The work in this thesis involves extensive modelling of wave propagation through numerical magnetic structures at photospheric and chromospheric heights. As such we are very much interested in the field strength and inclination profiles of sunspots (radially, vertically and azimuthally) at these layers of the atmosphere. An example of these properties, for the active region AR 10923, is shown in figure 1.4, with an emphasis on the magnetic field strength and inclination. The top-left panel shows the intensity continuum at 6300 Å which is essentially at the base of the photosphere, where  $\tau = 1$  (where  $\tau$  is the optical depth scale for a given frequency and a value of unity implies that radiation is free to escape at that frequency). The boundary between the umbra and penumbra is in this case defined as the radius at which the field is inclined by roughly 40-45° from the vertical and is denoted in the figure by the white contours. One can also clearly make out the umbral, penumbral and quiet-Sun boundaries in the intensity continuum here. The field strength and inclination drop off fairly monotonically with radius, from peak strength and vertical field in the umbra to weak and horizontal outside of the penumbra. The spine-intraspine penumbral structure is also clear, as is the azimuthal field inclination variation resulting from it.

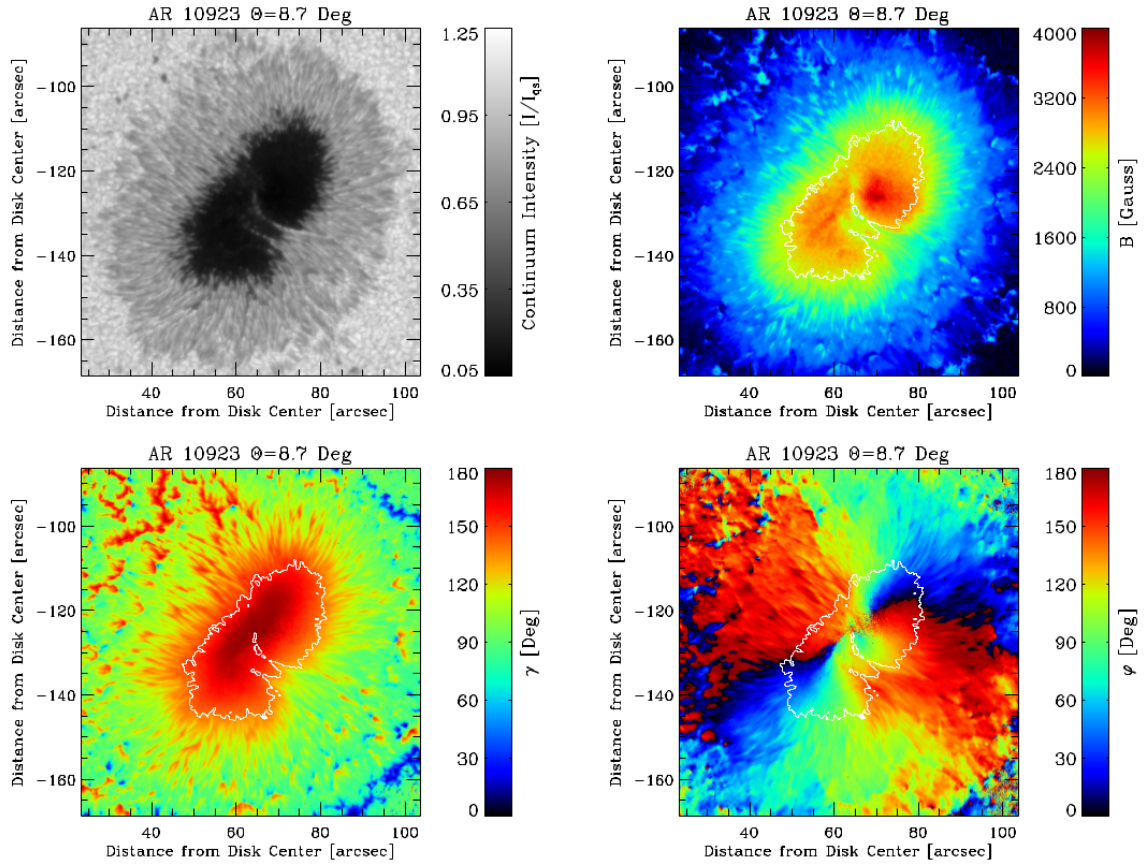


Figure 1.4: Quiet-sun scaled 6300 Å continuum intensity ( $I/I_c$ , upper-left panel), total magnetic field strength ( $B$ , upper-right panel), field inclination from observer's line-of-sight ( $\gamma$ , bottom left panel) and the azimuth angle of the magnetic field vector in the plane perpendicular to the line of sight ( $\varphi$ , bottom right panel) for the sunspot AR 10923 (Borrero & Ichimoto, 2011). Observations were taken at an angle of  $\Phi = 8.7^\circ$  from disk centre. White contours indicate a rough umbral-penumbral boundary.

### 1.2.2 Numerical modelling of sunspots

There are a vast range of approaches to modelling sunspots numerically. The pertinent question to ask is: ‘to what extent do we wish to reproduce observed sunspot features?’ When performing helioseismological calculations for instance, it is essential to have an accurate physical sunspot model to use in conjunction with inversions. When conducting forward modelling of wave-sunspot interactions it is also important to have at least on-average similarities between observed and simulated spots.

Here we provide a brief description of the magneto-hydrostatic (MHS hereafter) class of sunspot models, which are the basis for the simulations performed in chapters 2 and 3. Detailed descriptions of the theory behind other classes of models can be easily found, for example in the reviews by Fan (2004), Moradi et al. (2010), Rempel & Schlichenmaier (2011) and Reale (2014).

#### Force-free and potential models

MHS sunspot models are static, background sunspot atmospheres that consist of a field in equilibrium with some quiet-Sun non-magnetised atmosphere. The goal of these models is not to capture the small-scale magnetic or thermal features present in a sunspot in the way a radiative simulation might. Instead the point is to model a reasonably realistic on-average thermal and magnetic field structure with an inclination and field strength profile comparable to what we would observe in a roughly symmetrical sunspot. The thermal structure of a sunspot varies significantly from that in the quiet-Sun of course, particularly in the umbra where the Wilson depression is evident. Both the thermal and magnetic structure are known to induce strong positive and negative phase shifts, which need to be accounted for when performing local helioseismic time-distance calculations (Cally, 2009; Lindsey et al., 2010).

The dynamical time scale for magnetoacoustic waves to cross sunspot-sized areas of the photosphere is of the order of hours. Sunspots are generally stable over time periods of many days or even weeks, which is long-lived with respect to the corresponding local photospheric wave travel time. It thus makes sense to forego any time evolution of a model sunspot and enforce the MHS constraint (in cgs units),

$$-\nabla p + \rho \mathbf{g} + \frac{1}{4\pi} (\nabla \times \mathbf{B}) \times \mathbf{B} = \mathbf{0}, \quad (1.1)$$

along with the divergence-free field condition

$$\nabla \cdot \mathbf{B} = 0,$$

where  $p$  is the gas pressure,  $\rho$  is the gas density,  $\mathbf{g}$  is the gravitational acceleration and  $\mathbf{B}$  is the background magnetic field vector.  $(\nabla \times \mathbf{B})/4\pi$  is the electric current density,  $\mathbf{J}$  (by Amperes law) and  $((\nabla \times \mathbf{B}) \times \mathbf{B})/4\pi$  is the the Lorentz force. In the simplest case, the field will be described in a cylindrical geometry  $(r, \Phi, z)$  where all variables are independent of the azimuthal ( $\Phi$ ) component. This approximates the ideal azimuthally symmetrical sunspot, separated from any other small-scale magnetic structure or convective effects, with no field twist of any kind. The sunspot in this case is essentially unipolar, with its bipolar component at some significant distance away.

As can be seen from equation 1.1, if there is no corresponding energy equation, then either  $\mathbf{B}$  or  $p$  must be prescribed beforehand, ideally with an accompanying equation of state. As such the force balance is usually calculated independently of the energy balance. The equation can be simplified considerably in a low- $\beta$  atmosphere, such as in the upper chromosphere and corona where the gas pressure becomes negligible. Sunspot fields at these heights have the property of being near force-free (Wiegmann & Sakurai, 2012), in which case the force balance simply satisfies

$$\nabla \times \mathbf{B} = \alpha \mathbf{B},$$

where  $\alpha$  is constant along field lines. Therefore

$$(\nabla \times \mathbf{B}) \times \mathbf{B} = \mathbf{0},$$

as  $\mathbf{B}$  and  $\nabla \times \mathbf{B}$  are aligned in direction. Furthermore if  $\alpha = 0$  then the field is potential and solutions may be calculated by solving Laplaces equation for a scalar potential,  $\phi$ , where  $\mathbf{B} = -\nabla\phi$ . These models of course include no information regarding the thermodynamical properties of sunspot atmospheres and cannot include any magnetic/field-free boundaries, however purely potential-field models have had success in modelling pores (Simon & Weiss, 1970; Spruit, 1976; Meyer et al., 1977; Simon et al., 1983). Current-sheet models, which consist of a purely potential magnetic flux tube surrounded by a sheet of current and a field-free atmosphere have also been

applied to sunspots (Jahn, 1989). Sunspot fields are almost certainly not potential or field-free in the photosphere or lower chromosphere – the plasma  $\beta$  may even be greater than unity inside a photospheric umbra (Solanki et al., 1993; Solanki, 2003; Borrero & Ichimoto, 2011) – however there are entire analytical classes of constant  $\alpha$  and non-constant  $\alpha$  force-free field solutions which have been used to model fields well above surface heights with reasonable success (Martens et al., 1996; Neukirch & Martens, 1998).

### **Current-distributed MHS models**

Monolithic MHS sunspot models that do not satisfy  $(\nabla \times \mathbf{B}) \times \mathbf{B} = \mathbf{0}$  are more suited to photospheric and sub-photospheric modelling, where the field is not force-free. The sunspot model used in chapters 2 and 3 is a current-distributed model. These atmospheres do not have a current sheet or a sharp magnetic/non-magnetic boundary but instead consist of a field that merges smoothly into a field-free atmosphere through a smoothly varying and monotonic field strength and inclination profile.

The exact sunspot model formulation which we use is based on the work of Khomenko & Collados (2008) and came about as a result of the initial work of Low (1975). Pizzo (1986) subsequently developed a method whereby the pressure is initially specified as a boundary condition in the far quiet-Sun and in the sunspot umbra. Above the photosphere such thermodynamic distributions are readily available from observations. The magnetic field and the pressure are then iteratively determined subject to the condition that a force balance is achieved.

For the sub-photosphere we are limited to helioseismic inferences for thermodynamical distributions. This is not a problem in quiet-Sun regions, where the distribution of pressure, sound speed and density have been accurately determined (Christensen-Dalsgaard et al. (1985) for example) however the on-axis magnetic profiles are still largely unknown (Kosovichev, 2002; Couvidat et al., 2006). For this reason the self-similar approach of Low (1980) is used to generate a deep field, to an arbitrary depth.

The overall sunspot atmosphere consists of the concatenation of the deep self-similar model onto the photospheric pressure distributed model (Khomenko & Collados, 2008; Przybylski et al., 2015).

## 1.3 Helioseismic Inversions and their Successes

There are two primary and complementary approaches available when undertaking the study of solar phenomena on the local scale: helioseismic inversions and forward modelling. The work in this thesis is entirely based around numerical forward modelling, however local helioseismological techniques have uncovered much of the subsurface structure and explained many observed phenomena and so it is worth briefly discussing some significant helioseismological findings.

Global helioseismology uses the (predominantly low- $\ell$ ) oscillatory modes of the sphere to accurately ascertain large-scale sub-surface structure. It has been an incredibly successful field of research, with breakthroughs accurately revealing the profile of the quiet-Sun sound speed as a function of depth (Christensen-Dalsgaard et al., 1985), the depth of the convective zone (Christensen-Dalsgaard et al., 1991; Basu & Antia, 1997) and properties of solar differential rotation (Brown et al., 1989; Charbonneau et al., 1999). Inversions using such global modes are incapable of resolving small scale structure however and do not allow an interpretation of the full surface wave-field.

The techniques of local helioseismology were constructed to provide a full view of the subsurface including the deeper structure of sunspots and how flows and waves interact with this structure. The primary local helioseismic inversion techniques have all brought about significant contributions to our understanding. The methods all have different strengths and weaknesses and not all techniques are applicable to all problems.

Time-Distance Helioseismology (Duvall et al., 1993; D'Silva, 1996; D'Silva et al., 1996; Duvall et al., 1997) for example measures travel times between wavepackets at two (or more) locations. By comparing the travel times with known values (usually from an analytic model) a travel time perturbation can be calculated which can be interpreted as some form of subsurface inhomogeneity. Solving an inverse problem then yields the specific structure of the interior (Jensen, 2003). Fourier-Hankel analysis (Braun et al., 1987) provided one of the first breakthroughs of local helioseismology when it was shown that sunspots absorb the power of acoustic  $f$  and  $p$ -modes. By decomposing the oscillations around a sunspot penumbra into outgoing and incoming

waves, absorptions of between 50% (Braun et al., 1987) and 70 % (Braun & Duvall, 1990) were measured. The absorption coefficient was also shown to increase as a function of  $k$  (Braun et al., 1988) and to be noticeable in p-lage and surrounding regions (Braun et al., 1990). Figure 1.5 shows the absorption coefficients obtained using Fourier-Hankel analysis from Braun (1995) for the sunspot NOAA 5254 for a variety of moderate  $\ell$  waves. A value of  $\alpha = 0$  indicates no difference between the amplitude of incoming and outgoing oscillations, while  $\alpha = 1$  corresponds to total absorption. One can see that the absorption peaks at around 3 mHz and is more prevalent at higher  $\ell$ .

There is also a strong  $p$ -mode phase shift found in complement to the sunspot power absorption, as shown by Braun et al. (1992a) and Braun (1995), and displayed in figure 1.6. The data points with error bars indicate the  $m$ -averaged phase shifts measured around NOAA 5254 for a variety of  $p$ -mode ridges. The solid curves are from the semi-analytic work of Cally et al. (2003), which we discuss shortly. The fact that the absorptions and phase shifts occur more significantly for higher  $\ell$  and frequency respectively, suggests that the effect is a shallow one.

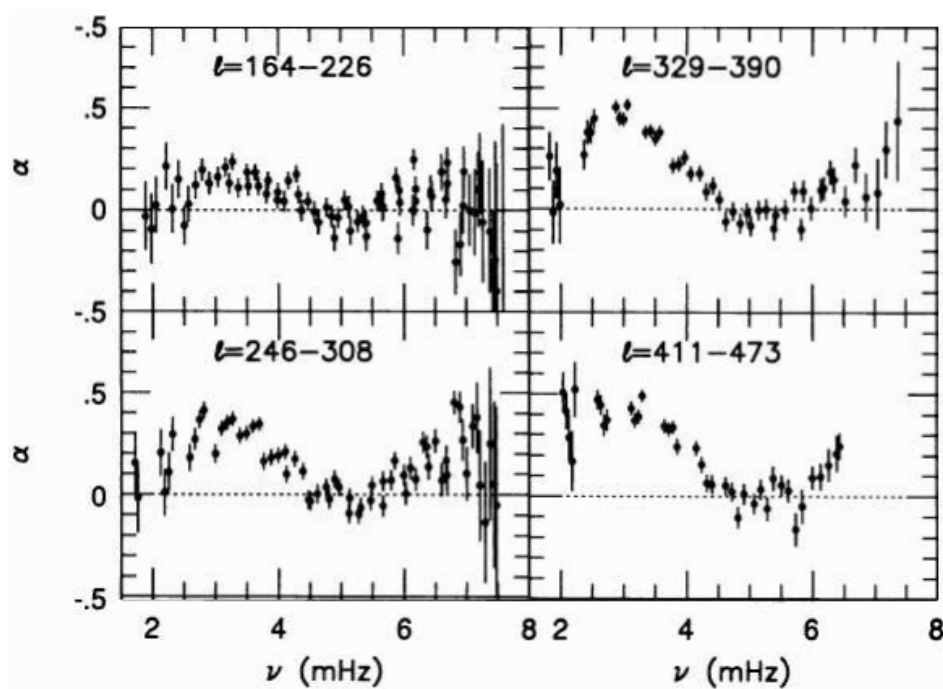


Figure 1.5: Fourier-Hankel absorption coefficient,  $\alpha$ , for the sunspot NOAA 5254 for various ranges of the harmonic degree,  $\ell$  (Braun, 1995).

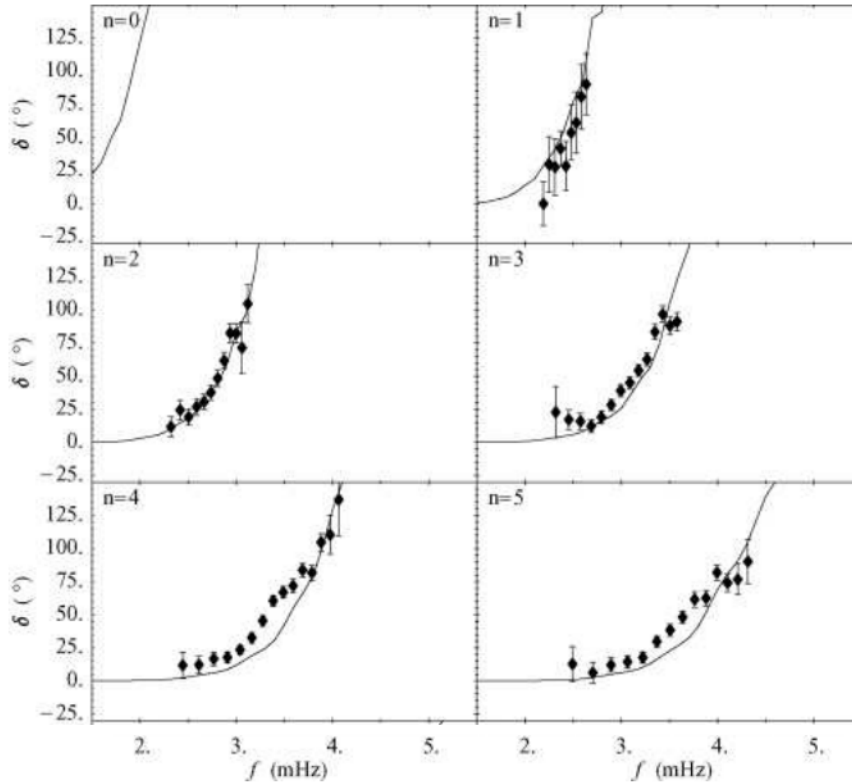


Figure 1.6: Phase shift difference between outgoing and incoming waves for a range of radial orders,  $n$ . The solid curves are the inclined-field simulation phase shifts from Cally et al. (2003) and the data points are from the Fourier-Hankel analysis of NOAA 5254 (Braun, 1995).

Theory was developed over the next decade in an attempt to explain the acoustic absorption and phase shifts. Spruit (1991) and Spruit & Bogdan (1992) importantly suggested that the absorption was a mode conversion effect; specifically that energy could be channeled to field aligned slow modes under the right conditions. Follow-up work (Cally & Bogdan, 1993; Cally et al., 1994; Bogdan et al., 1996; Bogdan & Cally, 1997; Cally & Bogdan, 1997) focused on the forward modelling of waves in gravitationally stratified adiabatic atmospheres with vertical and uniform magnetic field structures. Surface  $f$ -mode power absorption in these simulations showed good agreement with observations. The absorption of higher radial order  $p$ -modes however was significantly less than expected.

It was not until Cally (2000) and Cally et al. (2003) that efforts were made to

perform studies in field at realistic photospheric inclinations. The simulations yielded not only  $p$ -mode absorptions which roughly agreed with the values of Braun (1995) but also extremely accurate phase shifts (as shown by the solid curves in figure 1.6). The fact that the absorption and phase shifts were reproduced in a simple constant inclined field made clear the fact that mode conversion from fast to field-aligned slow magneto-hydrodynamic (MHD) waves is the dominant mechanism, rather than any variations in the thermal and magnetic structure brought about by the active region itself (although these variations do have a significant effect in the umbra). Other helioseismic techniques have also been successfully employed to measure the phase shifts, including acoustic imaging (Chen et al., 1998; Chou et al., 1999; Chou, 2000) and helioseismic holography (Roddier, 1975; Lindsey & Braun, 1990, 2000) yielding agreements with the Fourier-Hankel analysis described here.

With the availability of the *Heliospheric and Magnetic Imager* (HMI) (Scherrer et al., 2012) onboard the *Solar Dynamics Observatory* (SDO) current problems in helioseismology are related to subsurface active region structure and convection. Recently there have been inferences of convective transport velocities that are dramatically smaller than predicted by models of solar convective energy transport (Hanasoge et al., 2012b) – though Woodard (2016) presents a contrary opinion – and in particular there is much ongoing work to determine whether it is possible to predict the emergence of surface flux given its effects on helioseismic waves at deeper levels (Ilionidis et al., 2013; Stein et al., 2012). Local helioseismology in the presence of sunspots is prone to difficulty however. Phase shifts – interpreted as travel time perturbations – due to underlying structure can be introduced via returning fast waves which have sampled the *overlying* atmosphere, undergone mode conversion and re-entered the photospheric wave-field (Cally & Moradi, 2013). An in depth review on the theory and motivations behind these helioseismic techniques, including others such as Ring diagram analysis (Hill, 1988) can be found in Gizon & Birch (2005).

## 1.4 Waves in Magnetised Plasmas

In this section we give a brief mathematical description of the wave types prevalent in a magnetic plasma. We restrict our analysis to the linear regime, which is largely

appropriate in the photosphere and given the strictly linear codes which we use throughout this work.

### 1.4.1 The dispersion relation

Waves are the result of a restoring force acting in response to a perturbation to an otherwise equilibrium quantity. In a magnetised plasma there are a range of restoring forces in effect giving rise to a variety of wave types, with properties governed largely by the extent to which the plasma is either magnetically or thermally dominated. A magnetised plasma exhibits both a thermal and a magnetic pressure ( $P_g$  and  $P_m$  respectively), with ratio known as the plasma  $\beta$ ,

$$\beta = \frac{P_g}{P_m}.$$

The gas pressure restoring force yields the standard acoustic wave. The magnetic pressure gives rise to compressional magnetic waves. The domain where both the gas and magnetic pressure are dynamically important is where the magneto-acoustic wave exists. Magnetic field lines also exhibit a tension (the other component of the Lorentz force) which gives rise to the transverse and incompressible Alfvén wave.

Through some simple manipulation of the linearised MHD fluid equations, one can derive a dispersion relation that provides crucial information as to the behaviour of wave solutions present in a fluid without actually having to solve the entire system of equations. The standard system of MHD equations is simply the magnetic induction equation plus equations for hydrodynamic continuity and momentum for the dependent variables  $\rho$  and velocity ( $\mathbf{v}$ ), as well as an energy equation (which we choose this time to write in terms of the pressure,  $p$ ). Also included is the divergence-free condition on the magnetic field.

By introducing a small perturbation to background variables (with magnitude significantly less than the background quantity) one can express the linearised system as follows:

$$\frac{\partial \rho_1}{\partial t} + \nabla \cdot (\rho_0 \mathbf{v}_1) = 0, \tag{1.2}$$

$$\rho_0 \frac{\partial \mathbf{v}_1}{\partial t} = -\nabla p_1 + \frac{1}{4\pi} (\nabla \times \mathbf{B}_1) \times \mathbf{B}_0, \tag{1.3}$$

$$\frac{\partial p_1}{\partial t} + \mathbf{v}_1 \cdot \nabla p_0 = c^2 \frac{\partial \rho_1}{\partial t} + \mathbf{v}_1 \cdot \nabla \rho_0, \quad (1.4)$$

$$\frac{\partial \mathbf{B}_1}{\partial t} = \nabla \times (\mathbf{v}_1 \times \mathbf{B}_0), \quad (1.5)$$

$$\nabla \cdot \mathbf{B}_1 = 0. \quad (1.6)$$

Variables with a ‘0’ subscript refer to the background quantities, while a ‘1’ refers to the linear perturbations to those backgrounds.  $c$  is the gas sound speed and  $4\pi$  is the representation of the magnetic permeability constant in cgs units. This is of course a simple example of the MHD system, with only a linearised Lorentz force term and a pressure gradient on the right-hand side of the momentum equation; gravity has been ignored in this case.

Time-differentiation of (1.3) and subsequent substitution of the remaining equations allows for the elimination of all variables except for  $\mathbf{B}_0$  and  $\mathbf{v}_1$  and subsequently one is left with a wave equation for *linear* waves in a magnetised plasma,

$$\frac{\partial^2 \mathbf{v}_1}{\partial t^2} - c^2 \nabla (\nabla \cdot \mathbf{v}_1) + \frac{\mathbf{B}_0}{4\pi \rho_0} \times (\nabla \times (\nabla \times (\mathbf{v}_1 \times \mathbf{B}_0))) = \mathbf{0}.$$

If one assumes that solutions exist in the form of plane monochromatic waves, i.e.

$$\mathbf{v}_1(\mathbf{r}, t) = \mathbf{v} e^{i(\mathbf{k} \cdot \mathbf{r} - \omega t)},$$

where  $\mathbf{r} = (x, y, z)$  in standard cartesian coordinates, then one can make the replacements

$$\nabla \rightarrow i\mathbf{k}, \quad \frac{\partial}{\partial t} \rightarrow -i\omega$$

and the wave equation is transformed into a general algebraic equation:

$$\omega^2 \mathbf{v}_1 - c^2 (\mathbf{k} \cdot \mathbf{v}_1) \mathbf{k} + \frac{\mathbf{B}_0}{4\pi \rho_0} \times (\mathbf{k} \times (\mathbf{k} \times (\mathbf{v}_1 \times \mathbf{B}_0))) = 0. \quad (1.7)$$

One can derive dispersion relations for given wave types (under some simplifying assumptions) by applying various vector operations on equation 1.7. The dispersion relations themselves describe how the angular frequency  $\omega$  varies as a function of the wavenumber or wavevector ( $k$  or  $\mathbf{k}$  respectively, where  $k = |\mathbf{k}| = \frac{2\pi}{\lambda}$ ), and can provide other valuable information about the nature of a given wave mode. Mathematically, the relation expresses the condition under which non-trivial solutions exist. Expressing equation (1.7) in matrix form for the components of  $\mathbf{v}_1$ , it is simply the vanishing

of the determinant of the coefficient matrix. Under simplifying assumptions such algebraic equations can be re-arranged to the form  $\omega = \omega(\mathbf{k})$  in effect expressing the frequency in terms of the wavevector and even its inclination to the background magnetic field.

A given wave will travel with speed  $\omega/k$  in the direction of  $\mathbf{k}$  and thus the phase velocity is defined as  $\mathbf{v}_p = (\omega/k)\hat{\mathbf{k}}$ . This is the velocity at which a monochromatic wave with wavenumber  $k$  and angular frequency  $\omega$  will travel. In general a group of waves possessing a variety of wavenumbers will travel at the group velocity ( $\mathbf{v}_g$ ) where

$$\mathbf{v}_g = \frac{\partial \omega}{\partial \mathbf{k}} = \left( \frac{\partial \omega}{\partial k_x}, \frac{\partial \omega}{\partial k_y}, \frac{\partial \omega}{\partial k_z} \right)$$

in terms of the cartesian components of  $\mathbf{k}$ .  $\mathbf{v}_g$  describes the direction and velocity at which energy is transmitted and can differ distinctly from  $\mathbf{v}_p$ .

### 1.4.2 Acoustic waves

Pure acoustic waves exist in the absence of a magnetic field. Taking the dot product of  $\mathbf{k}$  with equation (1.7) and assuming  $\mathbf{B}_0 = \mathbf{0}$  yields the simple dispersion relation

$$\omega = \pm ck.$$

Sound waves are longitudinal (i.e. the wavevector points in the same direction as the oscillation of the particles) and isotropic. They are brought about by the plasma compressibility and the gas pressure restoring force.

### 1.4.3 Shear Alfvén waves.

Seeking transverse waves, where the direction of oscillation of wave material is perpendicular to the wave propagation ( $\mathbf{k} \cdot \mathbf{v}_1 = 0$ ) yields

$$\omega = \pm \frac{(\mathbf{k} \cdot \mathbf{B}_0)}{\sqrt{4\pi\rho_0}} = \pm \frac{B_0}{\sqrt{4\pi\rho_0}} k \cos \theta_B,$$

after taking the dot product with  $\mathbf{v}$  and some simplification.  $\theta_B$  is the angle between  $\mathbf{k}$  and  $\mathbf{B}_0$ . Generally the *Alfvén speed* is defined as  $a = B_0/\sqrt{4\pi\rho_0}$ , and so evidently the phase speed,  $\omega/k$  is such that

$$\frac{\omega}{k} = \pm a \cos \theta_B.$$

Thus the Alfvén wave propagates with maximum phase speed when aligned with the field and cannot travel perpendicularly to it. The shear Alfvén wave can also be shown to have a field aligned group velocity,  $\mathbf{v}_g = a\hat{\mathbf{B}}_0$  so that while these waves may travel at any angle to the field (except for  $\theta_B = \pi/2$ ) the direction of energy propagation is always along the field. The right-most term of equation 1.3 represents the Lorentz force and can be re-written (through the application of various vector identities) as

$$\frac{1}{4\pi}(\nabla \times \mathbf{B}_1) \times \mathbf{B}_0 = \frac{1}{4\pi}(\mathbf{k} \cdot \mathbf{B}_0)\mathbf{B}_1 - \frac{1}{4\pi}(\mathbf{B}_0 \cdot \mathbf{B}_1)\mathbf{k}.$$

The term  $(\mathbf{k} \cdot \mathbf{B}_0)\mathbf{B}_1$  represents the magnetic tension and the second term  $(\mathbf{B}_0 \cdot \mathbf{B}_1)\mathbf{k}$  is the magnetic pressure. It can be shown that the field perturbation for the Alfvén wave is always perpendicular to the background field ( $\mathbf{B}_0 \cdot \mathbf{B}_1 = 0$ ) meaning that the pressure term disappears and that dynamically, the magnetic tension is solely responsible for the incompressible Alfvén wave.

#### 1.4.4 Magneto-acoustic waves.

The magneto-acoustic wave is a result of both the magnetic pressure and the magnetic tension of the field. The wave propagation can be thought of as the compression and rarefaction of both the magnetic field lines and the plasma itself. From equation (1.7), the phase speed of the magnetoacoustic wave can be written as

$$\frac{\omega}{k} = \left( \frac{1}{2}(a^2 + c^2) \pm \frac{1}{2}\sqrt{a^4 + c^4 - 2a^2c^2 \cos 2\theta_B} \right)^{\frac{1}{2}}, \quad (1.8)$$

when both the magnetic field and the sound speed are non-negligible quantities. The  $\pm$  indicates two distinctly different wave modes, the *fast* magneto-acoustic wave (+ sign) and the *slow* magneto-acoustic wave (− sign).

The fast wave can be considered a magnetically modified sound wave and travels at its maximum phase speed when perpendicular to the field, so that  $\theta_B = \pi/2$  and  $\omega/k = \sqrt{a^2 + c^2}$ . The minimum speed is ( $\omega/k = \max(a,c)$ ) when parallel to the field. In contrast, the slow wave achieves its maximum speed of  $\omega/k = \min(a,c)$  when parallel to the field and cannot propagate in a direction perpendicular to it.

In the limit as the plasma  $\beta$  approaches  $\infty$  (either in the quiet sun or at great depth below the photosphere, where magnetic forces are unimportant) the fast wave

becomes the sound wave and the slow wave disappears. This can be seen by setting  $a = 0$  in equation 1.8. Alternately, at asymptotically low values of  $\beta$  (high in the tenuous atmosphere around magnetic regions or in the umbra of sunspots) the fast wave resembles a compressional magnetic wave with dispersion relation  $\omega = \pm ak$  and the slow wave travels along field lines at the sound speed, disappearing entirely when  $\beta = 0$ .

## 1.5 MHD Mode Conversion

Mode conversion is a well studied phenomenon, and there is a wide range of literature available on the subject - both in a solar and a purely plasma physics context. In the context of sunspot modelling we are interested in any effect that may alter the properties of oscillations in the vicinity of strong magnetic fields. The work presented in subsequent chapters investigates the effects of two primary types of mode conversion which occur at differing atmospheric heights and are governed by somewhat distinct, but related, physical principles.

*Fast-slow* mode conversion describes a process whereby energy may be channeled between the fast and the slow magneto-acoustic wave branches. The critical point in the atmosphere where this occurs is where  $a \approx c$ . We refer to this layer as the *a = c equipartition layer*. The layer is essentially at the same atmospheric height as the  $\beta = 1$  layer and separates the magnetically dominated upper atmosphere from the gas dominated depths below.

*Fast-Alfvén* mode conversion describes the channeling of energy from the fast magneto-acoustic branch to the Alfvén wave. This occurs slightly above the fast wave reflection height, which is normally above the equipartition layer. We will leave a discussion of this process until chapter 4, and focus here on a brief summary of the fast-slow mode conversion.

### 1.5.1 Fast-slow mode conversion and transmission

The first mode conversion type we will discuss is the conversion and transmission of energy between magneto-acoustic wave modes at around the  $a = c$  equipartition layer

of a magnetised atmosphere. In a gravitationally stratified magnetic atmosphere there are two velocity scales of importance: the Alfvén speed and the sound speed. The ratio  $a/c$  tells us the extent to which the local atmosphere is dominated by either magnetic or thermal effects (or both). The layer of the atmosphere (roughly where  $\beta = 1$ ) where  $a$  and  $c$  equate is the so called  $a = c$  equipartition layer. At this height, the phase speeds of the magnetoacoustic fast and slow waves are equal, allowing the two modes to interact; In this way energy can be channeled from the fast to the slow branch or vice versa.

In a sunspot umbra of sufficient strength the equipartition layer may lie below the photosphere, whereas in the weaker field of the penumbra and beyond the layer may extend well into the chromosphere. An upwards-travelling magneto-acoustic wave from the fast branch will be primarily acoustic in nature below the  $a = c$  equipartition layer (because by definition the sound speed is faster than the Alfvén speed where  $a/c < 1$ ). However provided the magnetic field is not too weak as to be negligible, there will also be a field-aligned slow mode present. When  $a/c \approx 1$  the normally separate branches of magnetoacoustic waves (the fast and the slow wave) may interact. If the upcoming waves are of sufficiently high frequency to penetrate above the acoustic cut-off and travel into the  $a > c$  atmosphere, the wave energy will be partially re-assigned into the fast or slow mode depending on the relationship between the wavevector and the orientation of the magnetic field.

The path of the fast magneto-acoustic wave above the  $a = c$  layer is controlled by the Alfvén speed just as the path of a downwards travelling acoustic wave is determined by the sound speed profile. Thus the fast wave will refract and then reflect at the fast wave turning height (where  $a^2 = \omega^2/k_h^2$ ) returning downwards from above the  $a = c$  layer.

Initially Cally (2006) and Schunker & Cally (2006) (summarised nicely in Cally (2007)) performed studies attempting to quantify this reassigning of wave energy at around the  $a = c$  equipartition height through the use of ray theory and semi-analytic simulations for rays incident on vertical and inclined uniform magnetic fields in adiabatic atmospheres. For a summary of the key conclusions, consider figure 1.7 which shows schematics of the ray path calculations. The thick dark curves below the horizontal  $a = c$  line are the ray paths representing an upcoming fast acoustic

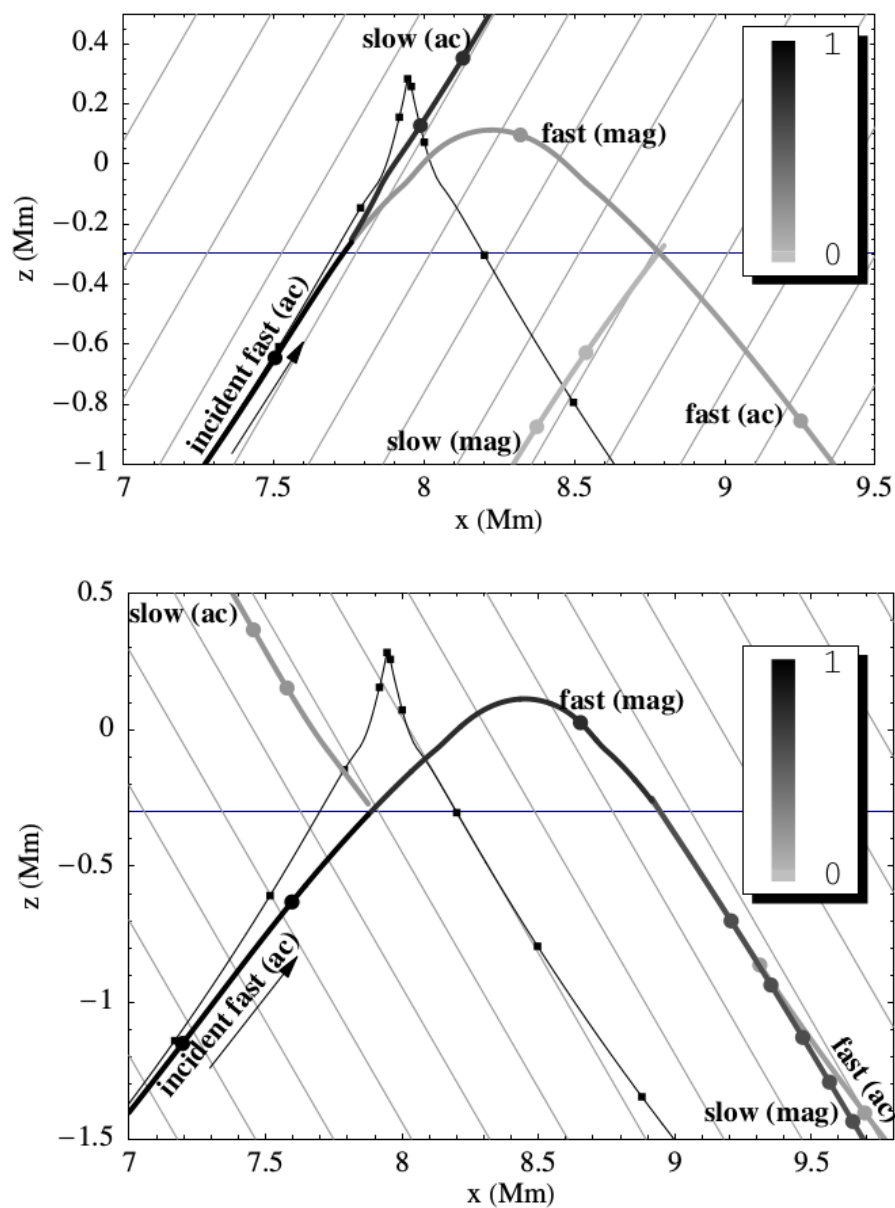


Figure 1.7: The ray path of an incident subsurface fast wave is shown in two cases, firstly in the case where the ray wavevector is relatively field aligned (top panel) and approaching close to perpendicular to the field (bottom panel). The horizontal line is the  $a = c$  layer and the background lines are magnetic field lines (Cally, 2007).

wave. Once  $a/c \approx 1$  a portion of the energy is channeled into either the fast or slow branch depending strongly on the attack angle between the ray and the field. The thin dark ray paths are the paths that would be taken by a purely acoustic ray in a field-free atmosphere; the acoustic waves are sharply reflected by the acoustic cutoff in this case. It is clear that energy is preferentially converted from the fast-acoustic mode to the fast-magnetic mode if there is a large attack angle between the wavevector of the incident wave and the orientation of the magnetic field. If the attack angle is small then energy will be primarily channeled into the slow mode, which follows the field lines (upwards and away in this case). In quantifying the effect, Cally (2006) showed that the fraction of energy *transmitted* through from the fast-acoustic wave to the field-following slow-acoustic wave can be approximated as

$$T = \exp(-\pi k h_s \sin^2 \alpha)_{a=c},$$

where  $h_s$  is the thickness of the equipartition layer measured along the wavevector (determined by the severity of the Alfvén speed profile, among other factors) and  $\alpha$  is the attack angle between the ray and the field. Naturally then the fraction of energy *converted* from the fast-acoustic branch to the fast-magnetic branch is  $C = 1 - T$ . The refracting magnetic wave will interact with the equipartition layer again upon returning downwards, re-converting back to the fast-acoustic branch (while again losing some energy to the slow-magnetic mode).

It is this refracting fast wave that we are primarily interested in for chapters 2 and 3; mode conversion has already proved a likely mechanism for the reduction of  $p$ -mode umbral power as discussed earlier, and we are aiming to show that the enhancements in high frequency acoustic and intensity power observed on the photosphere and chromosphere (known as the acoustic halo) is similarly a mode conversion driven process; specifically we provide significant evidence that the halo is created by an excess of energy at observation heights brought about by the returning fast wave.

## 1.6 Thesis Outline and Basis for this Research

The importance of understanding the dynamical interactions between oscillations and magnetic field structure in the solar atmosphere has long been understood to be

vitably important. The magnetically dominated heights above the transition region can support a variety of wave types, which often interact spectacularly with the magnetic field loops prominent in the corona.

In and below the photosphere compressible oscillations are manifested as magnetically (and gravitationally) modified acoustic waves whose properties depend significantly on the local plasma  $\beta$  and the ratio between the gas and magnetic pressures. While the physics is somewhat different at these lower heights the influence that the magnetic field exerts on waves here is no less profound. This thesis is focused on such interactions and primarily concerns itself with the study of fast-slow and fast-Alfvén mode conversion at photospheric and low-chromospheric heights amongst realistic sunspot-like magnetic field configurations. In particular the goals of this work are as follows:

1. To attempt to model a well-known active region phenomenon – the acoustic (or seismic) halo – using linear forward wave modelling in a realistic magneto-hydrostatic sunspot atmosphere.
2. To test the validity of the idea that the halo is related to the conversion and transmission of fast/slow magneto-acoustic waves at the  $a = c$  equipartition layer (roughly where  $\beta = 1$ ) above the photospheric surface.
3. To compare simulated halos with SDO observations of the same phenomenon in a rigorous manner.
4. To explore some of the properties of fast-Alfvén mode conversion in the context of a gravitationally stratified *twisted* magnetic field. Can we quantify the efficiency of the conversion as a function of the field twist and the various parameters governing the interaction between wave and field?

As discussed in the introduction, fast-slow MHD mode conversion has already been shown to be the mechanism responsible for the long-mysterious  $p$ -mode absorption exhibited by sunspot umbrae. It is therefore logical to assume that the related

*enhancement* in high-frequency time-averaged Doppler velocity power known as the acoustic halo (and discussed at length in the following chapter) may well also be governed by a similar wave-field interaction.

Chapters 2 and 3 detail our efforts to address the first 3 points above while chapter 4 addresses the last point.

## Chapter 2

We start in chapter 2 by attempting a simple experiment with a straight-forward premise: "Can we show that the power enhancement that characterises the halo is present when a finite wave pulse travels through a sunspot atmosphere and interacts with the magnetic field?" In answering this question we model the propagation of a single time-dependent perturbation to the vertical component of the velocity ( $v_z$ ) through a MHS sunspot atmosphere with a gravitational stratification. We choose the vertical component of the velocity as it corresponds to the line-of-sight Doppler velocity when observed at disk centre, which is roughly what most halo observations measure. The wave pulse is spatially localised and gaussian in its frequency spectrum. The aim is to observe the pulse as it propagates from its original position (below the surface of the photosphere) and travels towards the sunspot, observing the power enhancement structure (if any) that forms as a result.

We note that a reasonably realistic halo-like enhancement does indeed form. We then show a clear relationship between the  $v_z$  power structure and the  $a = c$  equipartition layer for the sunspot atmosphere. This is quite significant as the equipartition layer is where fast-slow mode conversion takes place. This also explains the fact that the halo is observed to spread with height.

## Chapter 3

In chapter 3 we make use of a much more realistic wave source function which approximates the acoustic bath present in the photosphere. This distributed source driver saturates the simulation domain and exhibits a realistic peak frequency at approximately 3.3 mHz with solar-like power ridges in  $\omega - k_h$  space. We also calculate synthetic intensities corresponding to the AIA 1700 Å and 1600 Å spectral line heights. In such a scenario we are able to truly compare the halos that form with

actual HMI and AIA velocity and intensity halo observations.

We find a range of similarities between simulated and observed halo structure, as well as some interesting differences which are perhaps brought about by the idealised geometry and simplicity of our simulations. In performing these simulations we employ Alfvén speed limiters which artificially modify the structure of the atmosphere above certain heights in order to limit the exponential increase of the Alfvén speed that results from a gravitationally stratified atmosphere. These limiters enforce a constant Alfvén speed above the critical heights at which we choose them to come into effect and are implemented to ensure a reasonable minimum simulation time-step, as dictated by the Courant-Friedrichs-Lewy condition. However in both chapters 2 and 3 we find that the halo magnitude *decreases* as a function of the height at which the limiter comes into effect. We conclude that the halo is entirely governed by the refraction and return of fast waves that have undergone mode conversion at the  $a = c$  equipartition layer.

We also discover a strong signal of fast-Alfvén mode conversion in our simulations which we suggest is very much present in real solar halos (albeit not as markedly) and which helps explain the spatial structure of the halo itself.

## Chapter 4

In the final chapter we proceed to explore the process of fast-Alfvén mode conversion in more depth, albeit in a semi-analytic capacity, rather than through large-scale numerical simulations. We expand on the work of Cally & Hansen (2011), who quantified the efficiency of fast-Alfvén mode conversion for uniformly inclined field in a cold plasma. Essentially we wish to determine the parameters under which the conversion to the upwards-travelling Alfvén wave is most efficient in the context of a *twisted* force-free magnetic field accompanied by a gravitationally stratified density profile.

In carrying out this parameter study we drive a mixture of fast and Alfvén waves from beneath the classical fast wave reflection height (FWRH). We allow the fast waves sufficient room to interact with the Alfvén resonance layer and therefore channel energy into the Alfvén wave. The Alfvén flux is measured at some height well above the resonance layer in order to determine the extent of the conversion.

We analyse the fast-Alfvén conversion in this way as a function of field twist, field inclination and wavevector-to-field attack angle in order to determine the optimal parameters for the conversion.

Due to the complexity of the twisted field, our parameter study is somewhat more simplified in its findings than the work of Cally & Hansen (2011), however we find broad agreement with those results. The fast-Alfvén conversion is most efficient when the fast wave wavevector-to field attack angle is approximately  $90^\circ$  and when the twisted field inclination approaches verticality (although the conversion is non-existent for precisely vertical field, as expected). Quantifying the extent to which fast wave energy may be re-assigned to the upwards-travelling Alfvén wave is important as energy transported by Alfvén waves is a leading candidate for a coronal heating mechanism, provided sufficient energy dissipation can be achieved at coronal heights.

Chapter 5 includes a thorough summary of our results and a discussion on the context of our findings and their implications for solar physics in general.

## 1.6. THESIS OUTLINE AND BASIS FOR THIS RESEARCH

---

Monash University

### Declaration for Thesis Chapter 2

#### Declaration by candidate

In the case of Chapter 2, the nature and extent of my contribution to the work was the following:

Nature of contribution	Extent of contribution (%)
Key ideas, development of code, modelling, production of all results, writing of paper	70

The following co-authors contributed to the work. If co-authors are students at Monash University, the extent of their contribution in percentage terms must be stated:

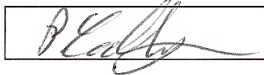
Name	Nature of contribution	Extent of contribution (%) for student co-authors only	
Paul Cally	Supervision and guidance		
Hamed Moradi	Co-supervision and guidance		
Damien Przybylski	Assistance in development of models		10%

The undersigned hereby certify that the above declaration correctly reflects the nature and extent of the candidate's and co-authors' contributions to this work\*.

Candidate's  
Signature

 Date 30/08/16

Main Supervisor's  
Signature

 Date 25/8/16

\*Note: Where the responsible author is not the candidate's main supervisor, the main supervisor should consult with the responsible author to agree on the respective contributions of the authors.

## Part II

# The Acoustic Halo

# Chapter 2

## Simple Modelling of the Acoustic Halo

### 2.1 Observations of the Acoustic Halo

The acoustic halo is a phenomenon first noted at around the same time as the umbral  $p$  - mode absorption, which was discussed in the introductory section of this work (Braun et al., 1987). Along with the magnetic flux-dependent reduction in 3 mHz acoustic power, Braun et al. (1992b) found a peculiar enhancement (with respect to average quiet-Sun values) in the 6 mHz acoustic power range which surrounded the sunspot and extended several Mm radially outwards. This anomalous enhancement was coined the "acoustic halo". The term in this case refers to the time-averaged Fourier power of the Doppler velocity wavefield taken from observations spanning a number of hours. The halos were also observed and subsequently verified by Brown et al. (1992). Toner & Labonte (1993), using data from Mees Solar Observatory, quantified the power enhancement, finding around a 10% increase over quiet-sun values in the 5.5 - 8.3 mHz frequency range, while also showing some evidence of a weak wavenumber dependence.

The year 1995 saw a great advance in the era of space-based solar observations, with the launch of the *Solar and Heliospheric Observatory* (SOHO). In Ni I 6768 Å spectral line dopplergrams taken by the onboard *Michelson Doppler Imager* (MDI) (Scherrer et al., 1995), Hindman & Brown (1998) note that the halo is absent in

measurements of the intensity continuum power. As can be seen in figure 2.1, the authors found that Doppler velocity power and continuum intensity power were almost identical for frequencies below the photospheric acoustic cut-off frequency of around 5.2 mHz. For non-trapped waves above this frequency the Doppler power exhibits the enhancement in contrast to the continuum intensity, which remains slightly suppressed at outer penumbral field radii. This suggests that either there is a process at work affecting observed power somewhere in the height range between the intensity continuum height and the Doppler velocity observation height, or that the mechanism causing the enhancement is not a process that is detectable in

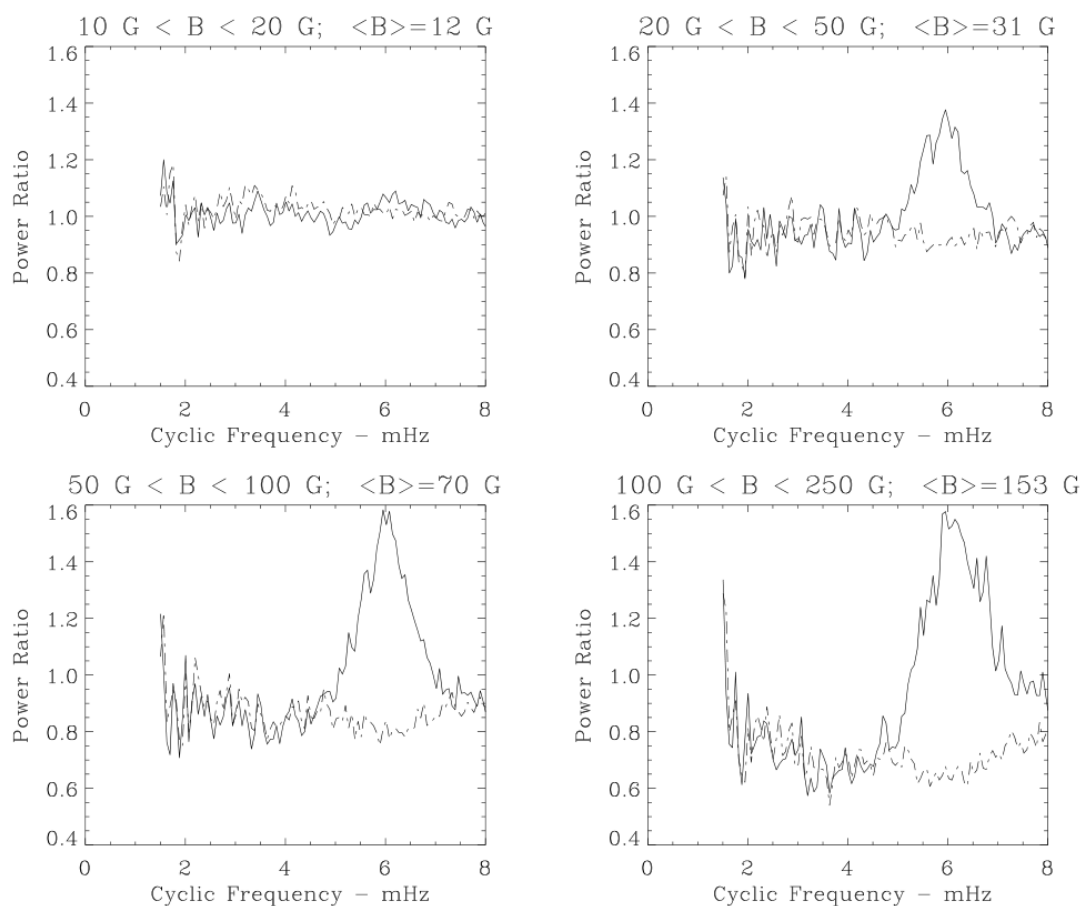


Figure 2.1: An MDI comparison between the intensity continuum power (dashed curves) and the Doppler velocity power (solid curves). The values have been averaged over different field strength pixels (indicated in each separate plot), and divided by the average value of quiet-Sun pixels (Hindman & Brown, 1998).

measurements of intensities. Time has shown that the former case is much more likely, as intensity halos taken from spectral lines at greater heights have since been observed and studied in detail (Moretti et al., 2007; Rajaguru et al., 2013). Evidently there is a physical process at work modifying the dominant oscillation frequency at heights *above* the base of the photosphere, where the intensity continuum is measured.

Whilst the suppression of acoustic  $p$ -modes was confirmed to extend to high-frequency oscillations in high field strength locations such as the umbra (Donea et al., 2000; Jain & Haber, 2002; Ladenkov et al., 2002), Thomas & Stanchfield (2000) confirmed the existence of halos in intermediate-strength field and also showed a larger, spatially extended enhancement in the overlying chromospheric Ca II K line.

Features of acoustic power enhancement and suppression continued to be brought to light throughout the next decade (Muglach, 2003; Muglach et al., 2005; Moretti et al., 2007; Nagashima et al., 2007; Gizon et al., 2009) due to the existence of instruments such as the Solar Optical Telescope (Katsukawa et al., 2007) onboard HINODE (Kosugi et al., 2007), the Transition Region and Coronal Explorer (TRACE) observatory (Handy et al., 1999) as well as MDI onboard SOHO.

More recently, Schunker & Braun (2011) examined 7 days of observations of the active region AR 9787 and unveiled some very specific halo properties. They showed that halos are manifested for relatively horizontally aligned, weak-to-moderate magnetic fields ( $150 \text{ G} < |\mathbf{B}| < 350 \text{ G}$ ) with enhancement magnitudes of up to 50% over average quiet-Sun values. The study also noted the interesting property that the power spectrum ridges of the enhancement region (in  $k_h - \omega$  space) were shifted towards a larger wavenumber for a given frequency (compared to the ridges from an area of the quiet-Sun) and that this effect is more pronounced for larger values of  $k$ , which suggests that the enhancement is a shallow wave effect, rather than a significantly deep one.

The most comprehensive observational halo study to date was conducted by Rajaguru et al. (2013), who utilised the HMI (Scherrer et al., 2012) and *Atmospheric Imaging Assembly* (AIA) (Lemen et al., 2012) instruments onboard SDO. The authors conducted a multi-height analysis of several active regions, measuring the time-averaged power from intensities and velocities corresponding to 6 different atmospheric heights. From the intensity continuum at  $z = 0$  (the base of the

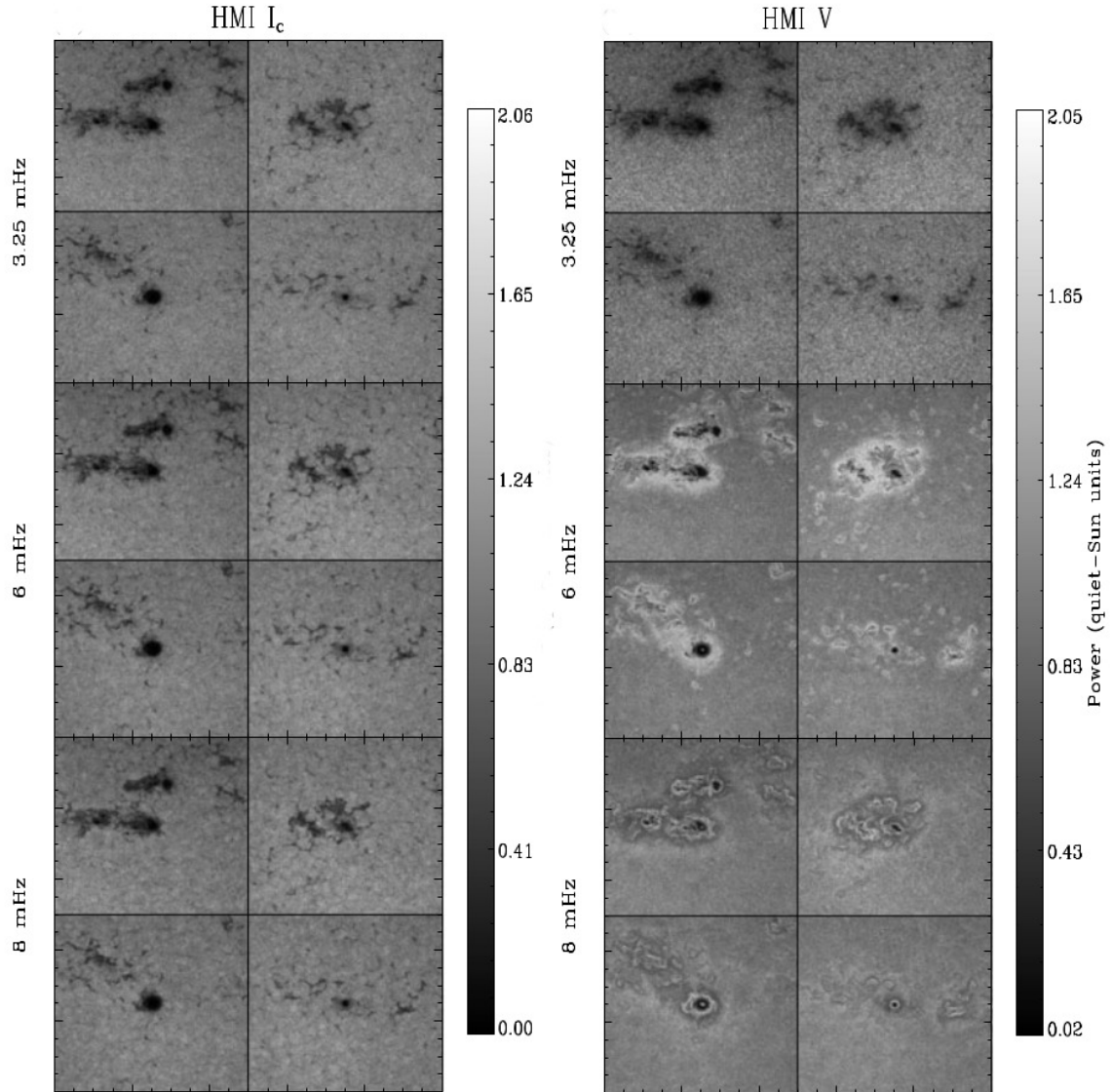


Figure 2.2: 14-hour quiet-Sun normalized Doppler velocity (right panel) and continuum intensity (left panel) power maps for the 4 different active regions studied by Rajaguru et al. (2013) at 3 different frequencies. The maps correspond to spatial areas of size  $373 \times 373 \text{ Mm}^2$  (Rajaguru et al., 2013).

photosphere, where the optical depth is unity) to Doppler velocities of the Fe I 6173.34 Å spectral line at around  $z = 140$  km to intensities measured from the AIA 1600 Å and 1700 Å chromospheric spectral lines, halo properties were compared and analysed in detail. Figure 2.2 shows power maps of the Doppler velocity acoustic halo for the 4 active regions in that work (right panels) and its aforementioned conspicuous absence in the intensity continuum (left panels). A summary of the halo properties uncovered in that work is presented as follows:

1. The halo is present for non-trapped frequencies, beginning at 5.5 - 6 mHz (as observed by all references above) and is present up to at least 9-10 mHz. The 6 mHz halo is the strongest in measurements of the Fe I 6173.34 Å Doppler velocity at  $z = 140$  km (shown in figure 2.2).
2. The halo magnitude is a clear function of observation height. There is no enhancement in the time-averaged intensity continuum ( $z = 0$ ) power (figure 2.2) or in the derived line-wing Doppler velocity ( $z = 20$  km). For weak-field regions at these heights, there is also a uniform wave power above the acoustic cutoff, which is to be expected. However, at  $z = 140$  km (the aforementioned HMI Doppler velocity line) the situation is markedly different, and the halo comes into effect.
3. The halo is clearly present in intensity observations of the chromosphere, as measured by AIA. The time-averaged power of the 1600 Å and 1700 Å wavelength channels (corresponding approximately to  $z \approx 430$  and 360 km above the base of the photosphere respectively) shows an intensity halo in the 7-10 mHz range, that spreads radially with height, agreeing with the suggestions of Finsterle et al. (2004).
4. The spatial extent and structure of the halo changes above about 8 mHz. This higher frequency halo is seen in power maps to be thinner and more confined spatially than the more diffuse structure seen at 6 mHz. Radially outwards from this higher  $\nu$  field is a region of slightly reduced power, which in turn is

surrounded by a diffuse, weak secondary halo region, extending radially many Mm into very weak and horizontal field regions (Rajaguru et al., 2013).

Rajaguru et al. (2013) also examined the halo structure in more detail both spectrally and as a function of the local field strength and its inclination. Figures 2.3 and 2.4 show an example of these spectral decompositions. In these figures the unfiltered power is shown as a function of  $|\mathbf{B}|$  and each pixel is grouped according to the local field inclination. In this study,  $\gamma = 0^\circ$  implies a horizontal field (whereas throughout the rest of this thesis we use an inclination angle where  $\gamma = 0^\circ$  is vertical field).

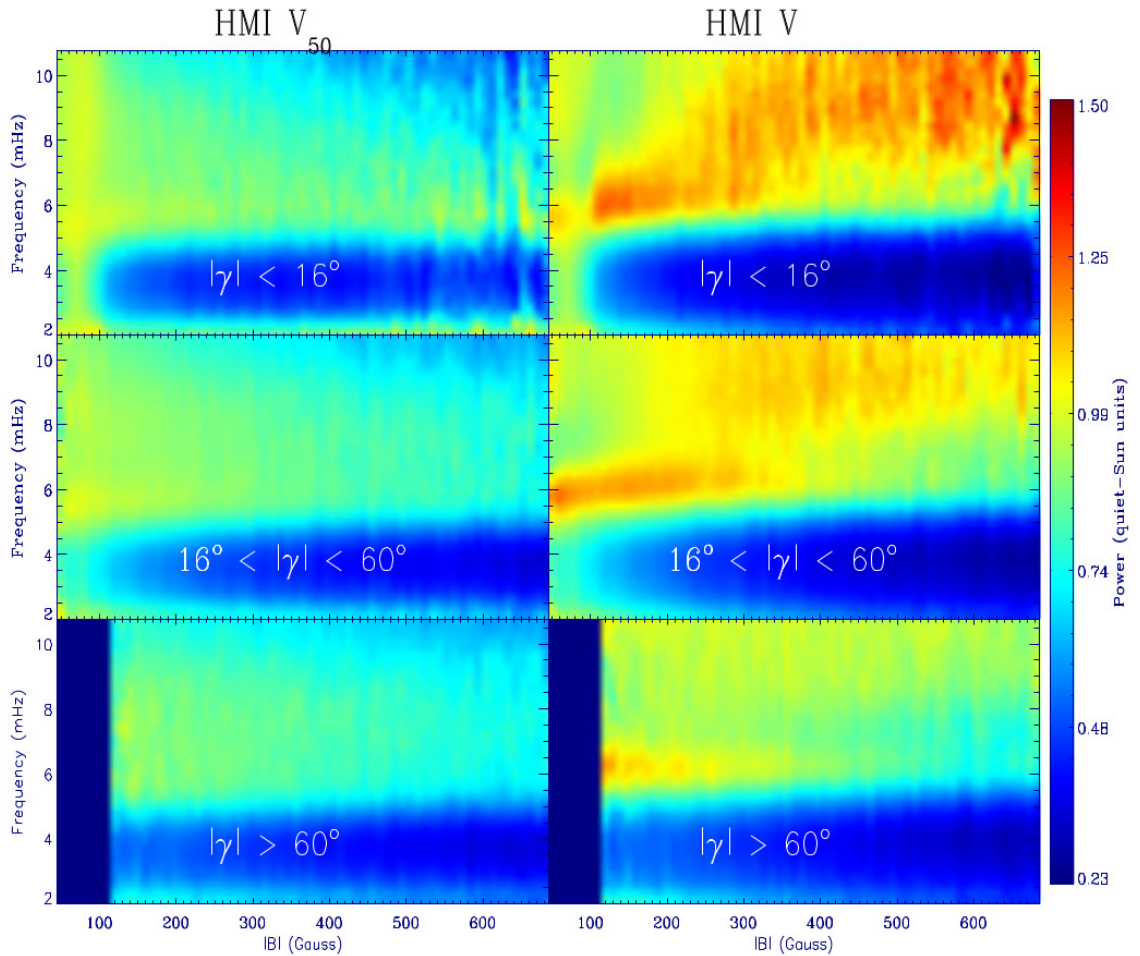


Figure 2.3: Unfiltered Fourier power corresponding to the Fe I 6173.34 Å Doppler velocity line at  $z \approx 140$  km (right column). A derived Doppler velocity corresponding to the lower height  $z \approx 20$  above the base of the photosphere (left column).  $\gamma = 0^\circ$  implies horizontal field in this case (Rajaguru et al., 2013).

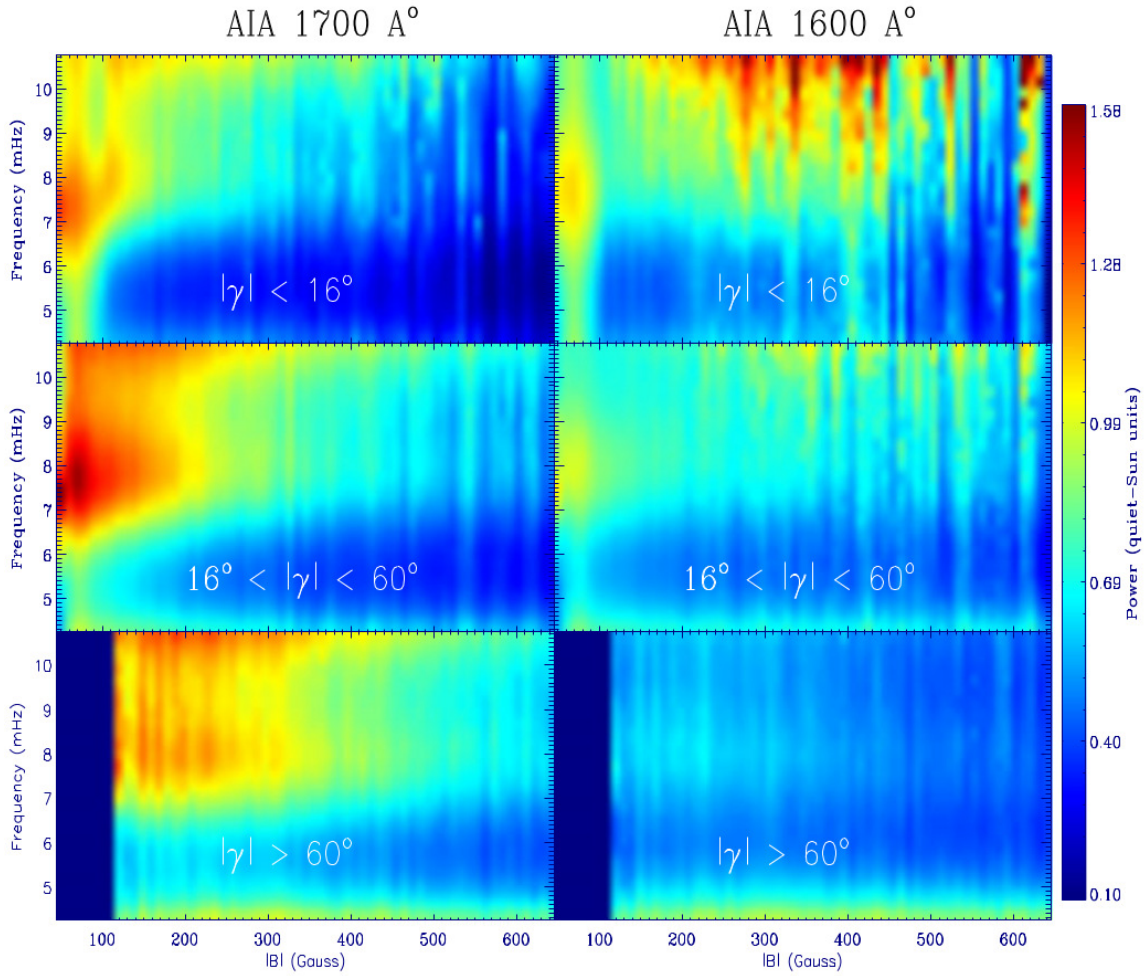


Figure 2.4: Unfiltered Fourier power corresponding to the AIA 1600 Å ( $z \approx 430$  km) and 1700 Å ( $z \approx 360$  km) spectral lines in the chromosphere. (Rajaguru et al., 2013).

One can see in figure 2.3 that the halo is strongly height-dependent. The left column is the power measured from a derived Doppler velocity at a height of around  $z \approx 20$  km above the photosphere. The right column is the standard Doppler velocity at  $z \approx 140$  km. Something is profoundly altering the oscillation frequency within a height range of only 120 km. It is also clear that the halo enhancement is at its peak value amongst inclined, near-horizontal field, with the signal disappearing for  $|\gamma| > 60^\circ$  (which is field approaching verticality in this study).

Intriguingly, even though a halo is not seen at  $z = 0$  in intensity continuum measurements, a halo is observed in spectral line intensities at greater heights, as shown in figure 2.4. One can see that the enhancement is largest at heights corresponding to

the AIA 1700 Å line, and becomes constrained to weaker field regions (while peaking at the same frequency) when observed up at the AIA 1600 Å line height.

## 2.2 Mechanisms for Halo Formation

There have been several recent theories which have attempted to explain the acoustic halo. Early theories suggested that the halos correspond to areas of increased acoustic emission (Brown et al., 1992). However such a mechanism would have a noticeable effect in measurements of the intensity continuum, which as discussed previously is not seen (Hindman & Brown, 1998; Rajaguru et al., 2013), casting doubt on this hypothesis.

Jacoutot et al. (2008) have performed radiative MHD simulations with an emphasis on the effect of the magnetic field on the frequencies of excitation originating from the solar convection zone. They found that the field shrinks the granulation scale size and shifts the local oscillation frequency upwards to higher values, consistent with halos.

Kuridze et al. (2008) shows (semi-analytically) that it is possible for waves of azimuthal wave number  $m > 1$  to become trapped under small canopy field regions, resulting in an enhancement in the high-frequency wave power which would be observable at photospheric heights.

Hanasoge (2009) suggests that the local oscillation is shifted preferentially from high to low mode mass (Bogdan et al., 1996), in high strength field regions due to the fact that flux tubes may act as a wave scatterer. The reasoning is that mode energy may be reorganised more significantly for high frequency waves because of their greater propensity for scattering.

Additionally the overlying magnetic canopy itself has been shown to be linked with photospheric power enhancement by Muglach et al. (2005), and in particular the mode conversion process that is governed by the ratio between  $a$  and  $c$ .

In this study we are interested in uncovering the halo mechanism. In order to do so, we must be able to reproduce the phenomenon using forward modelling and be able to explain its manifestation using concrete, known theory.

### 2.2.1 Fast-slow MHD mode conversion as a halo mechanism

We intend to follow up on the initial simulations and theory of Khomenko & Collados (2009), who have suggested that the fast-slow MHD mode conversion/transmission process may be the dominant driver of halo formation. Khomenko & Collados (2009) have performed 2D wave propagation simulations through a MHS sunspot atmosphere (Khomenko & Collados, 2008) to examine the halo. When using a monochromatic pulse wave driver (initiated below the surface of the photosphere, in the vertical component of the velocity) they noted a distinct interference pattern in the near-surface velocity field which coincided with a notable ‘bump’ in RMS velocity values for high frequency (non-trapped) waves. This bump is evident at around halo radii in the model atmosphere and is not present for low-frequency (trapped) waves.

Following up on this, they initiated simulations with  $v_z$  pulses exhibiting a gaussian frequency distribution and observed a power enhancement of around 40-60% in 5-8 mHz acoustic power (with respect to quiet-Sun values) in a narrow region 10-20 Mm from the sunspot umbra. A quick summary of these results is shown in figure 2.5. The power enhancements correlate well with the  $a = c$  equipartition region for the photosphere (where the photosphere is defined as the height at which the optical depth scale is unity). Particularly in the first two panels of the figure, the enhancement magnitude is of the order observed ( $\approx 50\%$ ) and seems to manifest for high (non-trapped) frequencies. The standard suppression of low frequency wave power around the sunspot umbra is reassuringly present as well. The similar locations of the RMS interference pattern and the halo-like power enhancements suggest that the halos may well occur simply as the addition of energy from high frequency non-trapped waves which have travelled above the  $a = c$  layer and undergone mode conversion, returning downwards to contribute to the observed wavefield.

As discussed in section 1.5, the fast magnetic wave above the  $a = c$  height will refract due to the rapidly increasing profile of  $a$ , and eventually undergo reflection where  $\omega^2 = a^2 k_h^2$ , depositing energy into regions below. It is these fast waves which can be enhanced by favourable field-wavevector orientations at the  $a = c$  height and which may deposit extra energy into observable heights as they return. Low frequency power would not be enhanced by this mechanism, as these waves are unable to reach

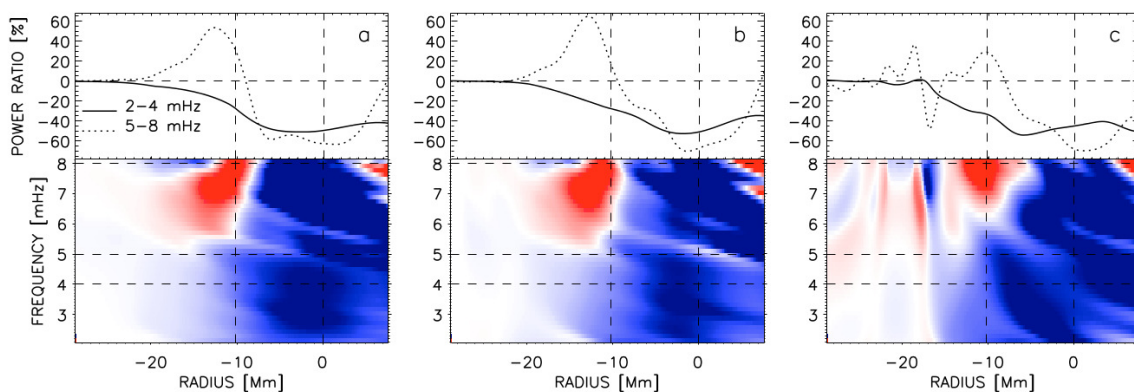


Figure 2.5: Ratio between photospheric wave power in the sunspot model relative to the quiet Sun model  $(P_{spot} - P_{quiet})/P_{quiet}$  as a function of horizontal position and frequency for three simulations with the wavelet source located at **a)**  $X_0 = -35$  Mm, **b)**  $X_0 = -30$  Mm and **c)**  $X_0 = -20$  Mm. The colour scale of the bottom panels ranges from  $-50\%$  to  $50\%$  (red means power excess). The upper panels show the power ratio averaged over the low-frequency and high-frequency bands (marked on the figure). The vertical dashed line located at  $x = 0$  marks the sunspot axis. The other dashed line (at around  $x = -10$  Mm) is where  $a = c$  in the photosphere (Khomenko & Collados, 2009).

the  $a = c$  height in general, except in special wave-field configurations where the ramp effect may reduce the effective acoustic cutoff frequency (Cally, 2006; Schunker & Cally, 2006; Cally, 2007). The fast-acoustic-to-fast-magnetic conversion is favoured at a higher frequency and, more importantly, by a large attack angle between the incoming wave and the magnetic field lines, which potentially explains why halos are consistently observed at near-horizontal fields; the line of sight component of the Doppler velocity is largely vertical (when observing at disk center) and provides a large attack angle with the horizontal field. The mechanism also naturally explains the spreading of the halo that is observed with height (Braun et al., 1992b; Brown et al., 1992), given that the  $a = c$  equipartition layer is located further outwards radially from sunspot center as a function of height.

The fraction of wave energy not channeled to the fast branch will transmit to the slow MHD wave branch. The slow waves are strongly field aligned at small  $\beta$  and may contribute to the diffuse, spatially extended halos observed by Rajaguru

et al. (2013), given that they can follow canopy field and return to the photosphere at some greater radius.

Recently Kontogiannis et al. (2014) performed an interesting observational study by examining photospheric and chromospheric power enhancements as functions of mode conversion parameters, such as the attack angle. They discovered chromospheric slow wave signatures corresponding to waves following the field lines upwards, as well as reflected fast wave signatures correlating with power enhancement regions for high frequency waves, lending further weight to the importance of mode conversion in this instance.

To summarise then, our hypothesis is the following: That the acoustic (and intensity) halo is created as a result of additional wave energy added to photospheric and chromospheric observation heights by the refraction and reflection of fast magnetoacoustic waves brought about by fast-slow mode conversion. The high frequency non-trapped acoustic waves normally present in the quiet-Sun would of course be unable to refract and return in this manner, and so the energy from these oscillations is not observed in the quiet-Sun.

In order to test this hypothesis, we will initially perform 3D linear forward wave modelling with a simple wavelet pulse acoustic source (similar to that used by Khomenko & Collados (2009)) to determine whether a halo-like enhancement becomes evident. In the next section we describe our computational approach and the details of our wave propagation simulations, paying particular attention to the equations to be solved as well as the details of the MHS sunspot atmosphere which we have chosen to use.

## 2.3 Forward Modelling with the SPARC Code

For the wave propagation simulations described in chapters 2 and 3, we make extensive use of the *Seismic Propagation through Active Regions and Convection* (SPARC) code (Hanasoge, 2007; Hanasoge et al., 2007). SPARC is a 3D wave propagation code which is ideally suited to the forward modelling of linear adiabatic wave propagation through magnetic atmospheres.

Output consists of the linear perturbations to the background states of the four

MHD variables  $\rho(x, y, z)$ ,  $p(x, y, z)$ ,  $\mathbf{B} = (B_x, B_y, B_z)$  and  $\mathbf{v} = (v_x, v_y, v_z)$  at desired timesteps and has been used several times for wave-sunspot interaction studies (Moradi & Cally, 2013, 2014; Moradi et al., 2015; Przybylski et al., 2015). The code solves the following ideal linearised Eulerian MHD system of equations in cartesian coordinates:

$$\frac{\partial \rho_1}{\partial t} = -\nabla \cdot (\rho_0 \mathbf{v}_1) - \nabla \cdot (\rho_1 \mathbf{v}_0), \quad (2.1)$$

$$\begin{aligned} \rho_0 \frac{\partial \mathbf{v}_1}{\partial t} = & -\rho_0 (\mathbf{v}_0 \cdot \nabla \mathbf{v}_1 + \mathbf{v}_1 \cdot \nabla \mathbf{v}_0) - \nabla p_1 - \rho_1 g \mathbf{e}_z - \rho_0 \Gamma \mathbf{v}_1 \\ & + \frac{1}{4\pi} (\mathbf{J}_0 \times \mathbf{B}_1 + \mathbf{J}_1 \times \mathbf{B}_0) + \mathbf{S}(\mathbf{x}, t), \end{aligned} \quad (2.2)$$

$$\frac{\partial p_1}{\partial t} = -c^2 \rho_0 \nabla \cdot \mathbf{v}_1 - \mathbf{v}_1 \cdot \nabla p_0 - \mathbf{v}_0 \cdot \nabla p_1, \quad (2.3)$$

$$\frac{\partial \mathbf{B}_1}{\partial t} = \nabla \times \mathbf{v}_0 \times \mathbf{B}_1 + \nabla \times \mathbf{v}_1 \times \mathbf{B}_0, \quad (2.4)$$

along with the divergence-free field condition  $\nabla \cdot \mathbf{B}_1 = 0$ . As always, ‘0’ subscripts refer to background quantities, while ‘1’ denotes the linear perturbations to those background values. All terms that are quadratic or higher in the perturbed variables are excluded. The variables  $c$ ,  $\rho$ ,  $p$ ,  $\mathbf{B}$  and  $\mathbf{v}$  in this case take on their standard meanings (gas sound speed, density, pressure, magnetic field and velocity respectively), with  $\mathbf{J} = \nabla \times \mathbf{B}$ . In addition  $g = g(z)$  is the acceleration due to gravity and  $\Gamma$  is a function describing the sponges on the horizontal and vertical boundaries of the simulation domain (if required). The  $\mathbf{S}(\mathbf{x}, t)$  term corresponds to an external forcing function which we use to drive waves of a type (and from a location) of our choosing throughout the atmosphere.

The density stratification and background magnetic field are read in as input to SPARC and can be any configuration in 2D or 3D, provided they are convectively stable (due to the linear nature of the code) and in MHS equilibrium. The code may also be run in a purely hydrodynamic mode, with no magnetic field, which is useful for comparisons with the quiet-Sun.

Numerically, time integrations are achieved through an optimised explicit 4th order Runge-Kutta scheme while spatial derivatives are calculated via an 11-point implicit finite difference grid. Due to the size and required resolution of such 3D

simulations the code is necessarily parallelised using the MPI framework. When this work was being carried out parallelisation was only partially incorporated, meaning simulation run-times were still significant. However the code has since been fully parallelised in all 3 spatial directions, (Przybylski et al., 2016 - in preparation) drastically reducing run-times.

### 2.3.1 Sunspot atmospheres

As mentioned, SPARC can be run in a non-magnetic hydrodynamic setting. In this case we simply set  $\mathbf{B} = \mathbf{0}$  in equations 2.1-2.4. As such the pressure gradients are purely vertical as there is no Lorentz force and the only requirement on the input atmosphere is that it is convectively (vertically) stable. We will refer to these simulations as quiet-Sun simulations (even though extremely weak fields are often present in the real quiet-Sun they are generally not dynamically important).

For the atmosphere itself we use a convectively stabilised version of the Model S (Christensen-Dalsgaard et al., 1996) joined onto the VALIIC chromosphere (Vernazza et al., 1976, 1981) which has been modified (by the method of Parchevsky & Kosovichev (2007)) to minimize convective instabilities which do not lend themselves well to linear wave simulations.

For our magnetic wave propagation simulations, we use the MHS sunspot model of Khomenko & Collados (2008) which has been thoroughly optimised by Przybylski et al. (2015) in order to increase spectropolarimetric accuracy and produce more realistic line formation regions. The model makes use of the Model S and the VALIIC chromosphere once again (as in the quiet-Sun case) for the distribution of quiet subphotospheric thermodynamic variables and the Avrett umbra for the non-quiet variables (Avrett, 1981). The MHS sunspot configuration consists of the joining of two different distributed-current models, the sub-photospheric self-similar model of Schlüter & Temesváry (1958) and Low (1980) and the potential configuration of Pizzo (1986). The latter flux tube requires a known distribution of pressure, both along the sunspot axis and in the quiet, non-magnetic atmosphere as a boundary condition. Such sub-photospheric profiles have been notoriously difficult to determine consistently in sunspot umbras, as they must be inferred via active region helioseismology,

and so as such the Pizzo (1986) model is used in the photosphere and at shallow depths. At greater depth, where  $\beta > 1$ , the Low (1980) flux tube is more appropriate and stable. The two magnetic profiles are joined at around  $z = -1$  Mm, using the techniques described in Khomenko & Collados (2008) and Przybylski et al. (2015).

As the sunspot is of the current-distributed class, there is no definite umbral-penumbral or penumbral-quiet-Sun boundary. The magnetic field strength and its inclination vary smoothly from a peak value and vertical field at the centre of the umbra to very weak and horizontal at the boundary (where the inclination is horizontally enforced). As such we define the umbral and penumbral extents based on field inclinations of  $45^\circ$  and  $60^\circ$  respectively (from the vertical).

There are a variety of free parameters available with which the user can modify the broad characteristics of the sunspot. The peak magnetic field strength, field inclination and general shape of the field can be altered via the three parameters  $a$ ,  $\eta$  and  $B_0$  described in Khomenko & Collados (2008), and we are also free to choose the vertical extent of the sunspot (both above and below the surface of the photosphere). The sunspot model also allows the user to prescribe the depth of the Wilson depression (the height at which the atmosphere becomes optically thin is depressed in high field regions such as the umbra).

We make use of two model atmospheres in this study; one with a peak surface field strength of  $|\mathbf{B}| \approx 1.4$  kG and another with  $|\mathbf{B}| \approx 2.7$  kG. We have assigned Wilson depression depths of 250 and 400 km respectively to these sunspot atmospheres, which are reasonably realistic values for the given peak surface field strengths. In this case the surface of the atmosphere is defined as the photospheric height at which  $\log(\tau_{5000}) = 0$  (where  $\tau_{5000}$  is the optical depth scale, as calculated from the thermodynamic values at every point in the box) and follows the Wilson depression. The surface corresponds to the height of formation of the  $5000 \text{ \AA}$  intensity continuum ( $z = 0$ ) in this atmosphere.

Figure 2.6 gives an overview of the 1.4 kG sunspot atmosphere that we have chosen to use in this case. As can be seen, the field strength drops and the inclination becomes horizontal quite swiftly, yielding umbral/penumbral and penumbral/quiet-Sun boundaries at around 10 and 30 Mm respectively.

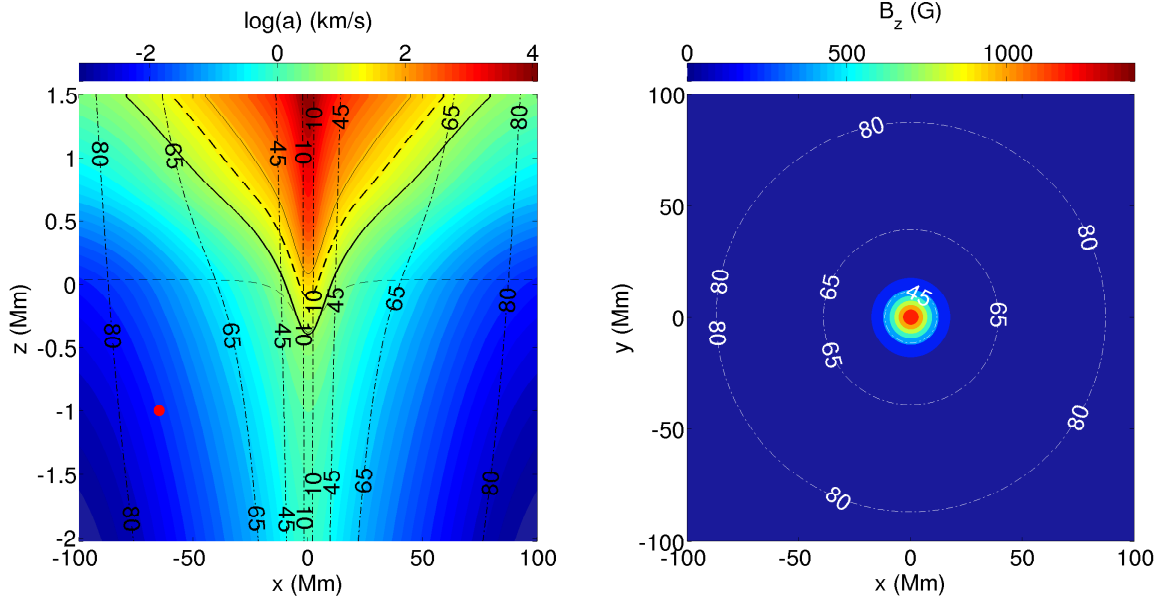


Figure 2.6: The left panel shows a 2D contour cut through the centre of the MHS sunspot atmosphere. Vertical dash-dotted curves are contours of field inclination (from the vertical). The thin black dashed curve corresponds to our reference photosphere, where  $\log(\tau_{5000}) = 0$ , with a Wilson depression of around 400 km. The thick solid curve is the  $a = c$  equipartition height and the thin solid curve is the height at which  $a = 80$  km/s (where  $a = a_{\max}$ ). The thick dashed curve corresponds to the fast wave turning height for a 6.5 mHz magnetoacoustic wave with  $k_h \approx 1.5 \text{ Mm}^{-1}$ . The background colour contour is  $\log(a)$  in km/s. The red dot corresponds to the location where the wave source was initiated. Note the highly stretched aspect ratio of the figure, with the abscissa spanning 200 Mm and the ordinate spanning only 3.5 Mm. The right panel shows a contour plot of the vertical component of the magnetic field -  $B_z$  (in G) for the spot taken at the surface, along with various field inclination contours (dashed contours).

### 2.3.2 Geometry and boundary conditions

The computational box that we have chosen consists of square, horizontal dimensions  $L_x = L_y = 200$  Mm, corresponding to 256 grid points and yielding a horizontal resolution of  $\Delta x = 0.78125$  Mm. We define a reference photosphere as the height at which  $\log(\tau_{5000}) = 0$ , while the vertical dimension spans from 10 Mm below this surface to 1.85 Mm above it. The vertical axis is scaled in inverse proportion to the sound speed with 215 grid points, yielding grid spacing on the order of 20 km above the surface, to spacings of around 100 km at the bottom of the box. In an attempt to keep the simulation as simple as possible and avoid any periodicity, we have implemented sponges along the sides of the box and perfectly matched layers (PML) along the top and bottom. The intention is to ensure that all outgoing waves are damped completely. We choose sponge parameters which come into effect in the outer 10 Mm of the horizontal domain, and the top PML takes effect over the top 15 grid points, resulting in a useable box top height of  $z = 1.5$  Mm above the photosphere.

### 2.3.3 A pulse wave driver

We begin by setting off a time-dependent wave pulse similar to that used by Moradi & Cally (2014) and Shelyag et al. (2009), of the form

$$\mathbf{S}(\mathbf{x}, t) = \sin \frac{2\pi t}{p} \exp \left( -\frac{(t - t_0)^2}{\sigma_t^2} \right) \exp \left( -\frac{(\mathbf{x} - \mathbf{x}_0)^2}{\sigma_x^2} \right),$$

where  $\mathbf{S}(\mathbf{x}, t)$  is the forcing term on the right hand side of the MHD momentum equation (2.2),  $p = 300s$ ,  $t_0 = 300s$ ,  $\sigma_t = 100s$  and  $\mathbf{x} = (x, y, z)$ .  $\sigma_x$  was chosen to give a pulse size of approximately 5 grid points in the  $x$ ,  $y$  and  $z$  directions, with  $\mathbf{x}_0 = (-65, 0, -1)$  Mm. In other words the wave source is located 65 Mm from the sunspot umbra (which lies at  $(x, y) = (0, 0)$ ), in the  $y$ -plane cutting through the centre of the spot, and at a depth of 1 Mm below the surface (this position is shown by the red dot in figure 2.6). The excitation is driven initially only in the vertical component of the velocity,  $v_z$ , which quickly begins to drive oscillations in all components of the velocity as well as perturbations to the background field. With the above parameters, the pulse excites waves with a range of temporal frequencies around 3.3 mHz in

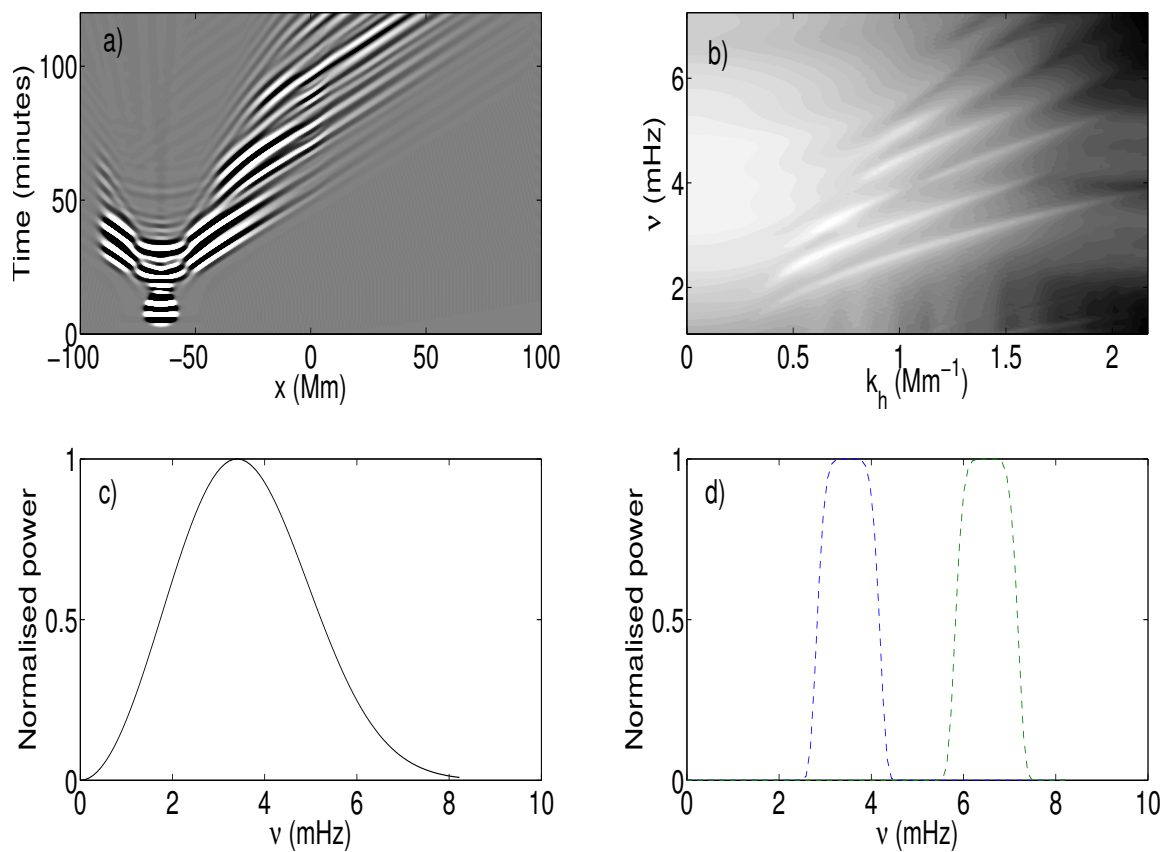


Figure 2.7: Panel a) shows the time-distance diagram of  $v_z$ , taken along the  $\log(\tau_{5000}) = 0$  contour corresponding to the surface, through the centre of the sunspot. b) shows the full 2-hour azimuthally averaged surface power spectrum of the simulation. c): The frequency distribution of the wave source, centred at 3.3 mHz. d): The filtering functions used to isolate power at 3.5 and 6.5 mHz.

somewhat of an approximation to the spectrum observed on the solar photosphere.

Figure 2.7 includes a summary of some of the features of the wave pulse. The frequency spectrum of the source is shown in panel c). Panel b) shows the power ridges calculated from the spatio-temporal Fourier transform of  $v_z$  at the surface, in  $\nu - k_h$  space. The ‘fuzzy’ region observed at low wavenumber results from wave interactions with the top and bottom box PML. Panel a) shows a time-distance plot of  $v_z$  taken along the  $\log(\tau_{5000}) = 0$  curve of figure 2.6 for the simulation duration of 2 hours. It is clear that the sponges have been reasonably successful at damping the waves, however there is a small amount of reflection occurring off the left hand side sponges, resulting in some very small amplitude waves returning through the simulation domain.

By utilising such a simple wave source, we may follow a wavepacket as it propagates from the quiet-Sun, through to the magnetically dominated regions of the sunspot, and analyze any dynamical features (such as halos) as they appear.

Figure 2.8 shows a 2-dimensional time progression of the pulse as it is initiated from the point  $\mathbf{x}_0$  and travels through the magnetic sunspot atmosphere, where  $v_z$  has been scaled by  $\sqrt{\rho}$  for clarity. As in figure 2.6, this is a cut through  $y$  in the centre of the spot and displays the progression of the pulse in the  $x-z$  plane. One can see the same small-scale reflection features in the left hand side absorbing boundary sponges as in the time-distance plot.

It is clear that the wave pulse behaviour is modified noticeably above the surface (thin dashed curve), as we would expect. Mode conversion takes place around the thick black  $a = c$  curve. Wave energy at this layer is channelled from the slow mode to the fast mode preferentially (if the attack angle is approaching perpendicular and the frequency is high (non-trapped)). The fast wave then begins to refract due to the increasing Alfvén speed profile and reflects at the FWRH (shown for the case of a wave with  $\nu = 6.5$  mHz and  $k_h \approx 1.5$  Mm<sup>-1</sup> by the upper thick dashed curve). All that is left of the fast wave above this height is an evanescent (exponentially decaying) tail. The magnitude of the  $v_z$  oscillations is clearly sensitive to these facts as it travels through the sunspot umbra.

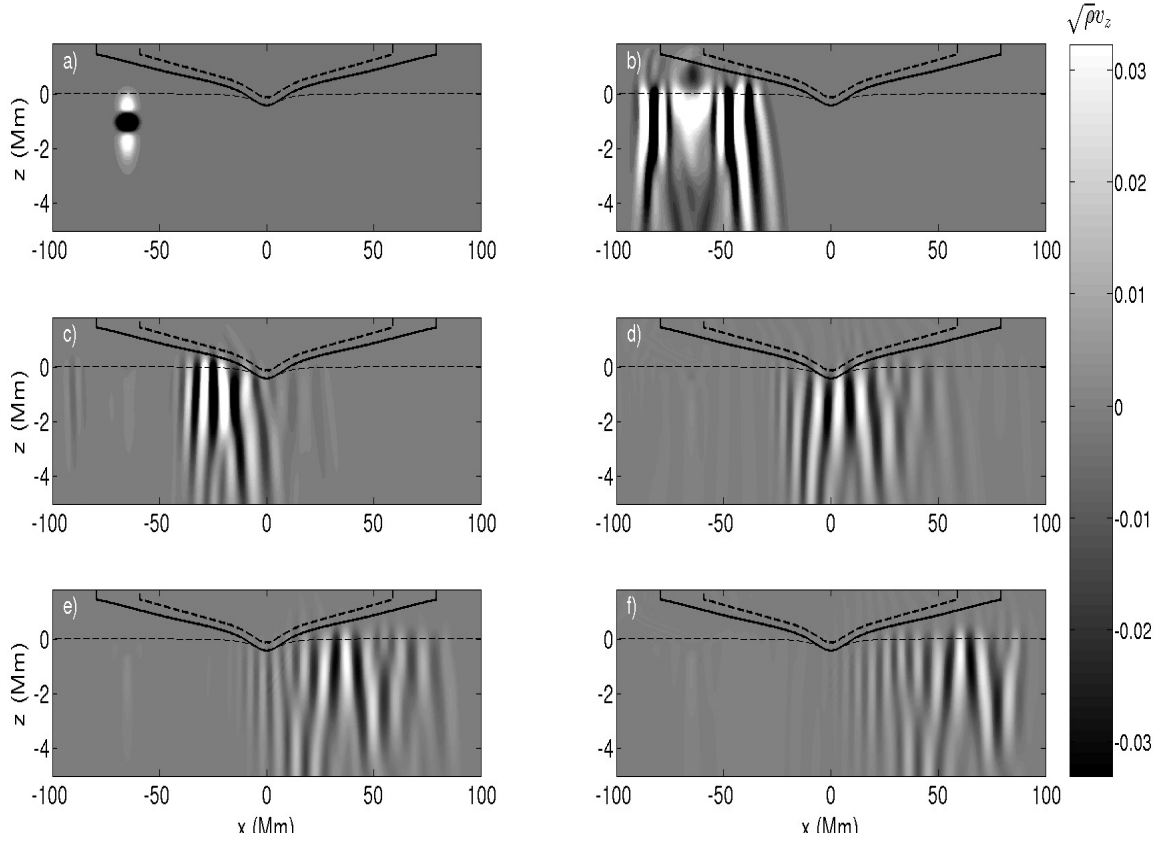


Figure 2.8: Snapshots of density-scaled  $v_z$  from a depth of -5 Mm to the top of the usable box at 1.5 Mm. a):  $t \approx 2$  min, b): 20 min, c): 40 min, d): 60 min, e): 80 min, f): 100 min. The sunspot umbra centre is at  $x = 0$  Mm. The three curves are the same as those in figure 2.6,  $\log(\tau_{5000}) = 0$  surface (thin dashed curve),  $a = c$  layer (black solid curve) and the FWRH for a 6.5 mHz fast wave (upper thick dashed curve).

### 2.3.4 Alfvén speed limiter

The most immediate problem when initiating forward modelling in a stratified magnetic atmosphere is the rapid increase in the Alfvén velocity with height caused by the swiftly decreasing density profile. The Courant-Friedrichs-Lewy (CFL) constraint on explicit finite differences schemes provides a limit on the maximum stable time step in a given simulation. If  $\Delta t$  is the time step,  $\Delta x$  is the grid spacing and  $V$  is the maximum local velocity scale, then we must have  $\Delta t < \Delta x/V$  on every grid point in the computational domain. In the low- $\beta$  atmosphere above the surface,  $V = a$  which rises exponentially, resulting in a correspondingly restrictive maximum  $\Delta t$  if we extend the box too far into the atmosphere. In order to overcome this challenge, we artificially modify the Alfvén speed such that it doesn't begin to grow to problematic magnitudes.

Methods of artificially capping the Alfvén speed at some manageable value have been well described recently, by both Rempel et al. (2009) and Hanasoge et al. (2012a). Having tried both approaches, we use the method of Rempel et al. (2009). The limiter is applied by specifying a maximum Alfvén velocity  $a_{\max}$  and then calculating a reduction term  $R_{\text{mag}}$ , where

$$R_{\text{mag}} = \frac{a_{\max}^2}{a_{\max}^2 + a^2(x, y, z)/c_q^2(z)} \quad (2.5)$$

and  $c_q$  is the quiet-Sun sound speed, with all terms expressed in units of cm/s. The reduction term is then applied to the Lorentz force term in equation (2.2). When  $a$  begins to dominate over  $c$ , or in other words the plasma  $\beta$  becomes sufficiently small according to a chosen criteria, the limiter will take effect and prevent any further rise in  $a$ . The result is that the Alfvén speed will remain roughly constant above the height where  $a = a_{\max}$ . It is important to ensure that such a limiter takes effect well above the FWRH for any high frequency waves of interest.

Indeed work has been done to ascertain whether the use of such limiter has a detrimental effect on helioseismic travel times (Moradi & Cally, 2014), with the conclusion being that one must be certain that the artificial capping is occurring well above heights where any relevant physics is occurring (such as the FWRH or the  $a = c$  layer).

For our initial pulse wave source simulations we have capped  $a$  at a value of

$a_{\max} = 80$  km/s, yielding a fairly manageable simulation time step of 0.2 s for our sunspot, which has a peak surface field of 1.4 kG. In figure 2.6 one can see that the reflection height for a typical halo frequency fast magneto-acoustic wave (dashed curve) is crucially between the  $a = c$  layer (thick black curve) and the  $a = 80$  km/s capped contour (thin black curve), meaning that with this choice of  $a_{\max}$ , the primary body of fast waves which undergo mode conversion are free to reflect back downwards unhindered by our non-physical alterations to the wave speed.

## 2.4 Simulation Results

Our primary goal is to undertake forward modeling of a simple wavepacket propagating through a sunspot-like magnetic field and atmosphere in full 3D and observe the structure of any resultant enhancements in time averaged acoustic power at high frequencies, both spatially and spectrally. Specifically we aim to analyse the power distribution on the near-side of the sunspot (to the source). The simulation run-time was 2 solar hours, which is a sufficient length of time for the wavepacket to pass through the sunspot umbra and most of the way to the opposite boundary, as can be seen in figure 2.8.

In order to analyse power enhancements we perform simulations in both quiet (non-magnetic) and full MHS sunspot atmospheres. For each grid point in space, for both atmospheres, we perform temporal Fourier transforms from the  $v_z$  perturbations and then calculate the Fourier power at each point as a function of  $\nu$ . This power is then filtered around a frequency range of our choosing.

The main quantity which we use throughout the paper to denote a halo enhancement is  $P = (P_{\text{mag}} - P_{\text{quiet}})/P_{\text{quiet}}$ .  $P_{\text{mag}}$  is the 2-hour averaged Fourier power of  $v_z$  calculated as described above in the magnetic atmosphere.  $P_{\text{quiet}}$  is the analogue to  $P_{\text{mag}}$  for the separate quiet sun simulation.  $P$  is therefore the fractional enhancement in power for the sunspot simulation (with respect to the power from the quiet-Sun simulation) at each grid point.  $P_\nu$  indicates that the power has been filtered about the frequency  $\nu$  mHz by applying gaussian filters of the type shown in panel d) of figure 2.7.

### 2.4.1 Evidence of a halo

Our first task is to identify that halos do indeed occur in our wave pulse simulations. Figure 2.9 shows  $P_\nu$  along cuts through the sunspot centre (along  $y = 0$ , also the plane in which the source is located) at 4 different sample heights, plotted as a function of radial distance from the centre of the sunspot.

In this study we have chosen to filter the power around two indicative frequency ranges,  $\nu = 3.5$  mHz and 6.5 mHz, using the filters shown in figure 2.7. These are similar ranges to those used by Khomenko & Collados (2009) and respectively represent low  $p$ -mode frequencies (which generally cannot penetrate above the acoustic cut-off height to contribute to halos) and high non-trapped halo frequencies. The top left panel of figure 2.9 corresponds to the photospheric surface, where the optical is unity ( $\log(\tau_{5000}) = 0$ ), whereas the others are at the constant geometrical heights labelled and the fractional values of the enhancements have been converted to percentages.

We of course expect to see the well observed  $p$ -mode absorption for the low frequency 3.5 mHz waves, which are suppressed in power when propagating through regions of high magnetic field strength. This can clearly be seen in figure 2.9;  $P_{3.5}$  shows a deficit with increasing proximity to the sunspot and no power enhancement whatsoever. In contrast, there is a strong 6.5 mHz power enhancement visible at all heights. To be clear, a value of  $P = 100\%$  indicates a doubling of quiet-Sun power; enhancements of 100 – 300% are clearly seen, which is significantly larger than the observed halo values (Hindman & Brown, 1998; Jain & Haber, 2002; Schunker & Braun, 2011; Rajaguru et al., 2013) of between 40-60% and indeed the values achieved in 2D simulations (Khomenko & Collados, 2009; Zharkov et al., 2009). The wave field in the solar photosphere is of course much more complex than our simple gaussian wave pulse however and so the magnitude is less of a concern than the qualitative behaviour of the enhancement at this point.

We also show power maps for  $P_{6.5}$  over the full  $x$ - $y$  plane in figure 2.10 for the same 4 heights. The red ‘+’ indicates the position of the source in the  $x$ - $y$  plane and the dashed curve shows the outward spreading of the  $a = c$  layer with height. The high frequency power enhancement appears to correlate extremely well with the position of the  $a = c$  layer just as Khomenko & Collados (2009) found in the

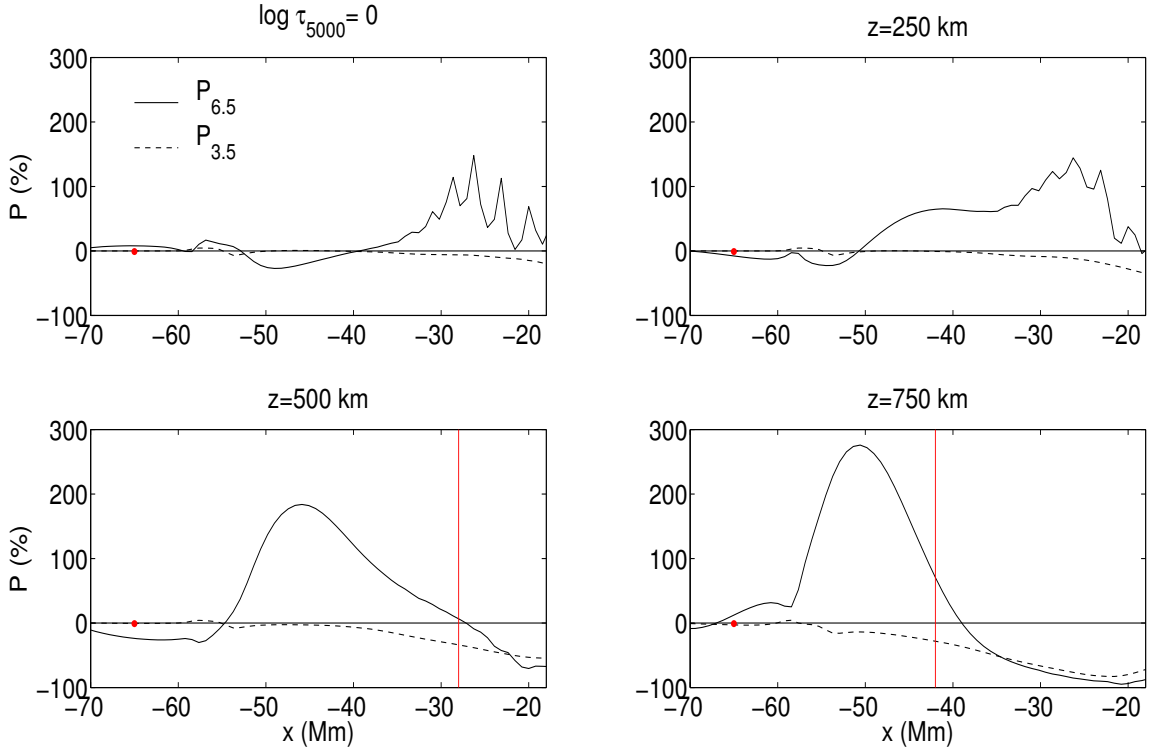


Figure 2.9:  $P_\nu$  at the surface, and at constant geometrical heights of  $z = 250$ , 500 and 750 km, extending from around 20 to 70 Mm from the centre of the sunspot umbra (the umbra is to the right of the figures, at  $x = 0$ ). The solid line is the 6.5 mHz enhancement and the dashed line is the 3.5 mHz enhancement. The horizontal solid line indicates  $P = 0\%$ , which is a quiet-Sun value. Anything above this line we consider to be an enhancement. The source radial position of -65 Mm is shown by the red dot (although it is of course located 1 Mm below the surface). The vertical red line is the point at which  $a = c$  for that particular height.

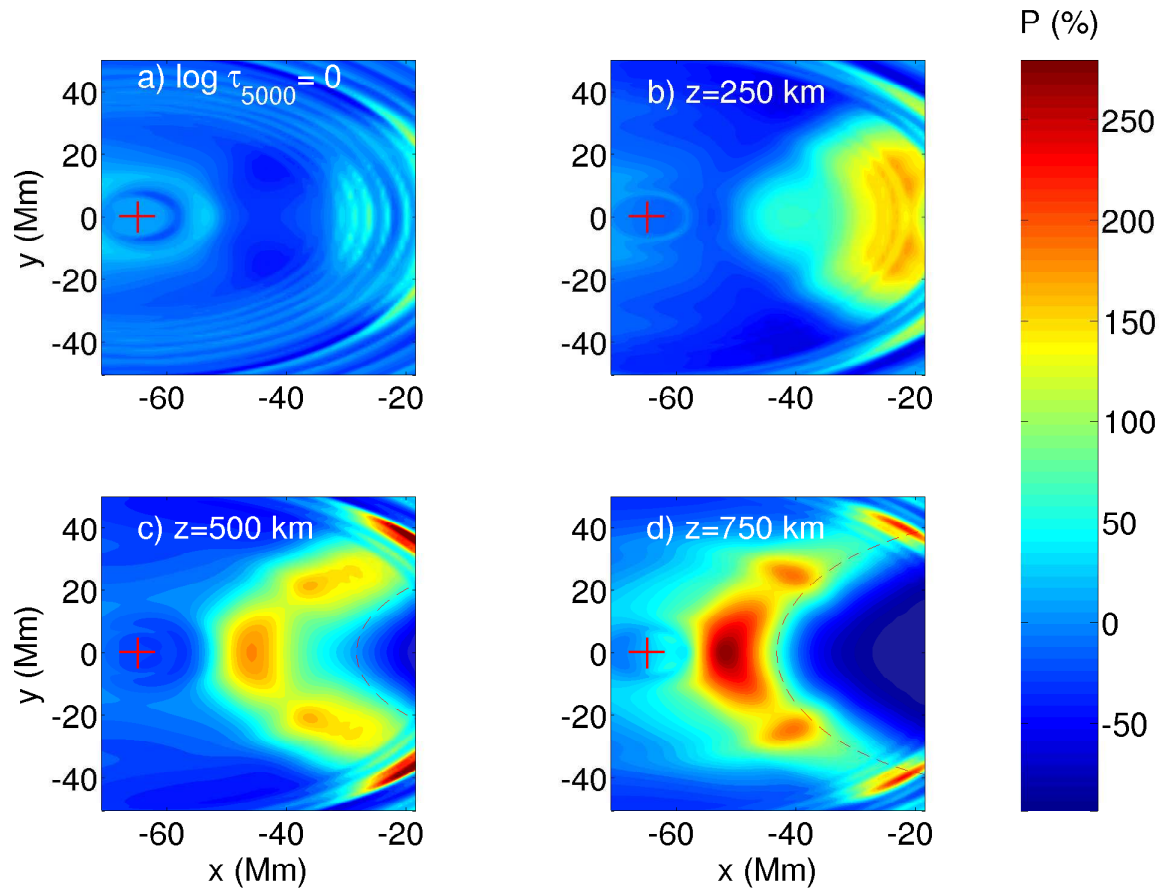


Figure 2.10: Power maps of  $P_{6.5}$  over the same height range for the  $x$ - $y$  plane, restricted to the near side of the sunspot. The dashed curve visible at  $z = 500$  km and  $750$  km is the  $a = c$  contour for that particular height. The source radial position of  $-65$  Mm is shown by the cross.

2-dimensional case. It appears that this relationship is also true for multiple heights, as evidenced by the spreading of the enhancement with the  $a = c$  layer.

### 2.4.2 Testing the hypothesis

We are primarily interested in whether mode conversion and the refraction of high frequency waves is the source of the halo enhancement. It is therefore necessary to ascertain whether the enhancements are true halos or simply an aberration caused by the magnetically modified atmosphere. In order to determine this we compare our results with another simulation that we shall term the thermal atmosphere case. The thermal simulation is performed with our 1.4 kG sunspot atmosphere as normal, however the background field itself is removed everywhere when the simulation begins. In this instance the atmosphere is not really in MHS equilibrium, however it tells us if the enhancement is caused by wave-field interactions (as it should be if mode conversion is the cause); if the field is the cause of the halo we expect to see no enhancement in the thermal case.

Figure 2.11 shows the comparison between  $P_{6.5}$  and  $P_{\text{ther}-6.5}$ , where where  $P_{\text{ther}}$  is the analogue to  $P$ , denoting the time averaged power enhancement at 6.5 mHz at every spatial point for the thermal case. Clearly the thermal simulation yields no meaningful high-frequency power enhancement, and so we conclude that the interaction between field and wave is key to the enhancement seen in this simulation. If we had seen enhancements comparable to the magnetic case, our hypothesis would look shaky indeed.

To expand upon these simple findings we examine the spatial power enhancement structure in more detail. We next examine  $P_{3.5}$ ,  $P_{6.5}$  and  $P_{\text{ther}-6.5}$  as functions of  $x$  and  $z$  (instead of along set heights) in figure 2.12. The figure is simply the 2D version of Figures 2.9 and 2.11, displayed for heights from  $z = 0$  to  $z = 1$  Mm above the surface, once again on the near side of the sunspot. One can see from panel a) that the behaviour of  $P$  is quite complex. Significantly, the halo-equipartition layer correlation hinted at in the previous figures is extremely clear, with the enhancement manifesting below the  $a = c$  layer and spreading radially outwards with height, agreeing with observations (Rajaguru et al., 2013; Schunker & Braun, 2011) and

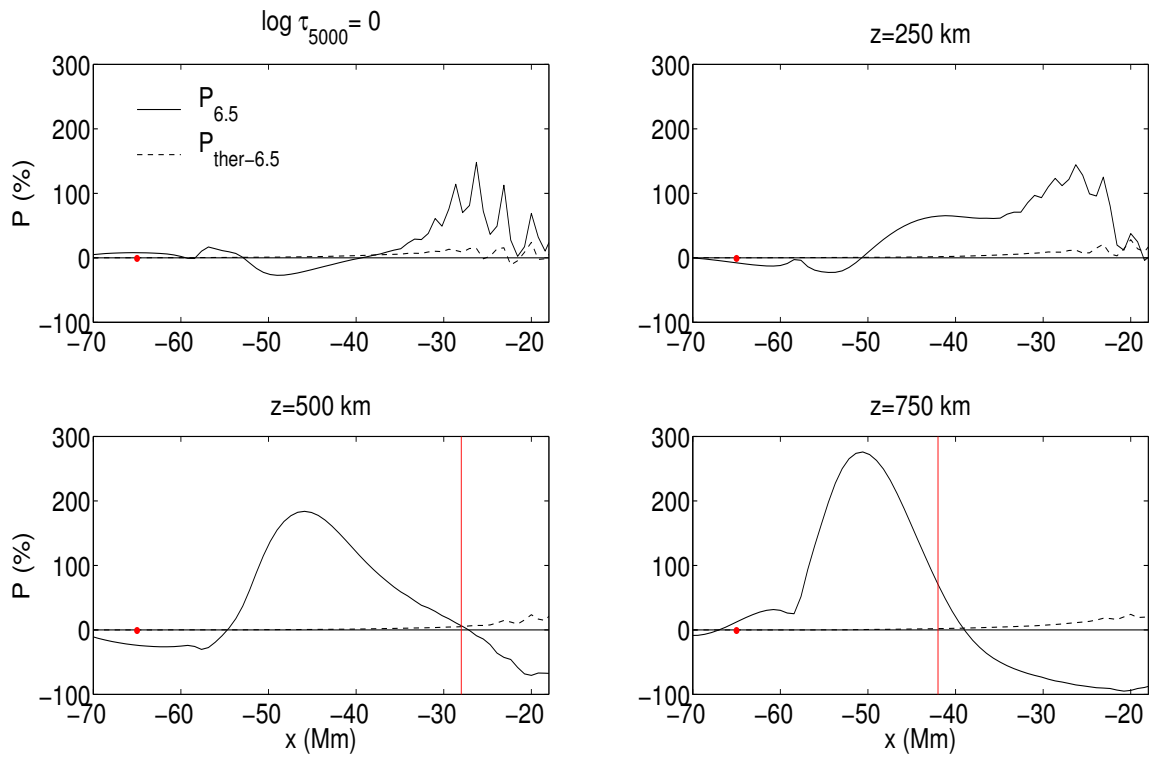


Figure 2.11: In a similar manner to figure 2.9, we take cuts at 4 heights, including the surface. The solid curve is  $P_{6.5}$ , just as in figure 2.9. The dashed curve is  $P_{\text{ther}}$  at 6.5 mHz. The vertical red line is the point at which  $a = c$  for that particular height.

## 2.4. SIMULATION RESULTS

---

the prediction of Khomenko & Collados (2009). There are two lobes of larger power separated by a region of weaker - but still significant - enhancement. It is difficult at this stage to state whether the characteristics of the pulse are the cause of this dual-lobe structure or whether the reason is deeper and related to the mode conversion itself. Importantly also of course there is no halo in either the 3.5 mHz or the thermal cases.

With a reasonably realistic enhancement structure firmly established, we turn now to the real crux of the matter. We must test the validity of our original assertion that the acoustic halo is generated by extra deposited energy from downwards travelling fast waves. If this is the halo mechanism, then logically if fast waves are prevented from returning from above the  $a = c$  layer, the halo should disappear. We proceed by performing 3 additional simulations to the ones already discussed. These simulations are identical to our primary 2-hour simulation (from which we have calculated  $P_\nu$ ) in every way except that we have enforced successively stricter Lorentz force limiters (as in section 2.3.4) on the 3 atmospheres, resulting in lower Alfvén speed limits of  $a_{\max} = 50, 20$  and  $7$  km/s respectively.

Recall that the primary simulation in which we detect the strong halo enhancement has  $a_{\max} = 80$  km/s, which means that the atmosphere is only modified where  $a > 80$  km/s, which is well above the FWRH for halo frequency waves. With  $a_{\max} = 7$  km/s the Alfvén speed is capped just above the  $a = c$  layer; therefore upcoming fast acoustic waves that undergo mode conversion to fast magnetic waves are never able to achieve the condition for refraction, that  $a = \omega/k_h$  (as  $a$  is constant above this height), and so cannot return downwards and contribute to a halo.

The other cases  $a_{\max} = 50$  and  $20$  km/s are the intermediate cases which restrict the return of successively higher frequency waves. Comparisons between these simulations, showing the 6.5 mHz power enhancement ( $P_{6.5}$ ) presented in the same manner as in figure 2.12, are displayed in figure 2.13.

The behaviour is clear; as  $a_{\max}$  is lowered to 50 km/s and then to 20 km/s the halo magnitude decreases noticeably at this frequency of 6.5 mHz. panel d) clearly shows the complete reliance of the halo on the effects of the overlying magnetically dominated  $a > c$  atmosphere. To be clear, the atmospheres used for the 4 simulations are all identical below the  $a = c$  layer. For d) the atmosphere is modified above this

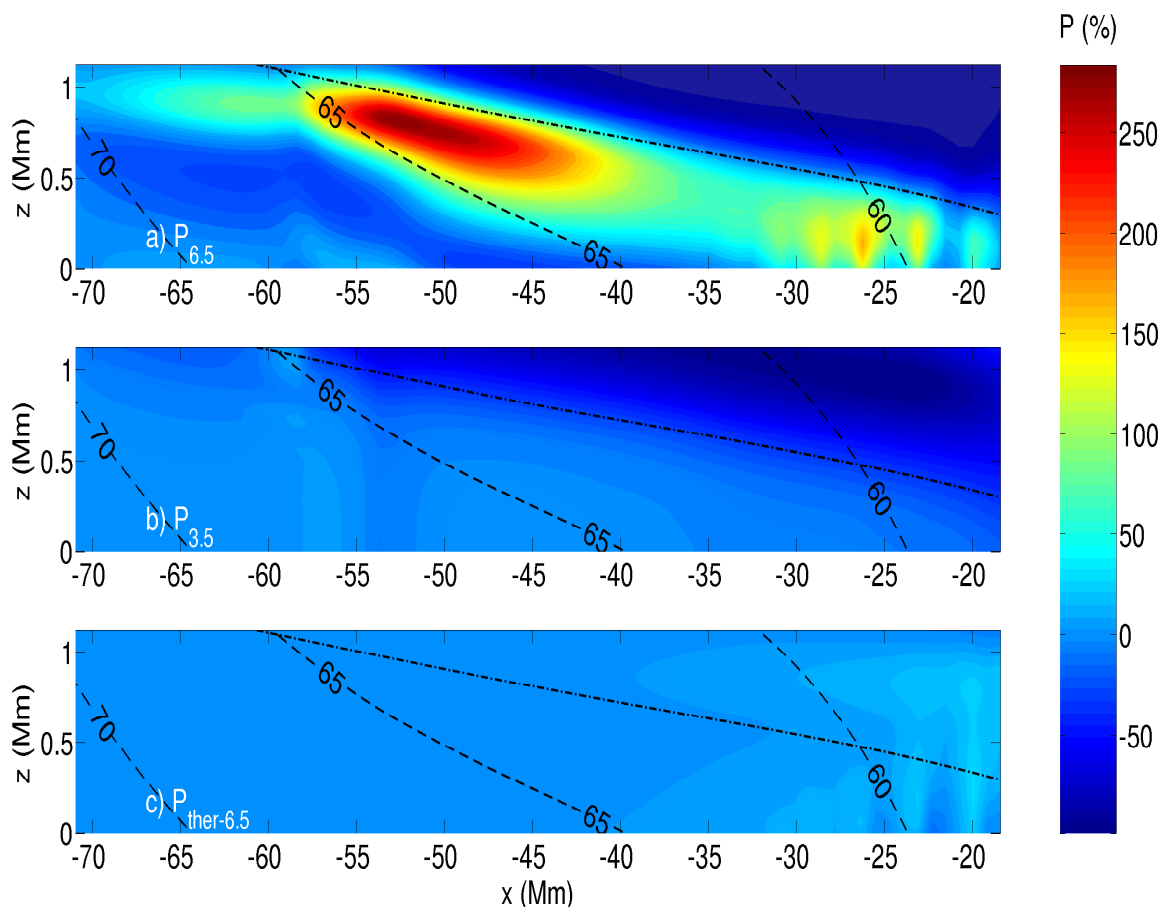


Figure 2.12:  $P$  and its relationship with the  $a = c$  height. This is the vertical plane taken along the line  $y = 0$  in figure 2.10. Panels a) and b) are  $P_{6.5}$  and  $P_{3.5}$ . Panel c) shows the enhancement (or lack thereof) for the thermal case,  $P_{\text{ther-6.5}}$ . The dot-dashed curve is the  $a = c$  equipartition layer and the thick dashed labelled curves are contours corresponding to magnetic field inclinations of 70, 65 and 60 degrees (from left to right) with respect to the vertical.

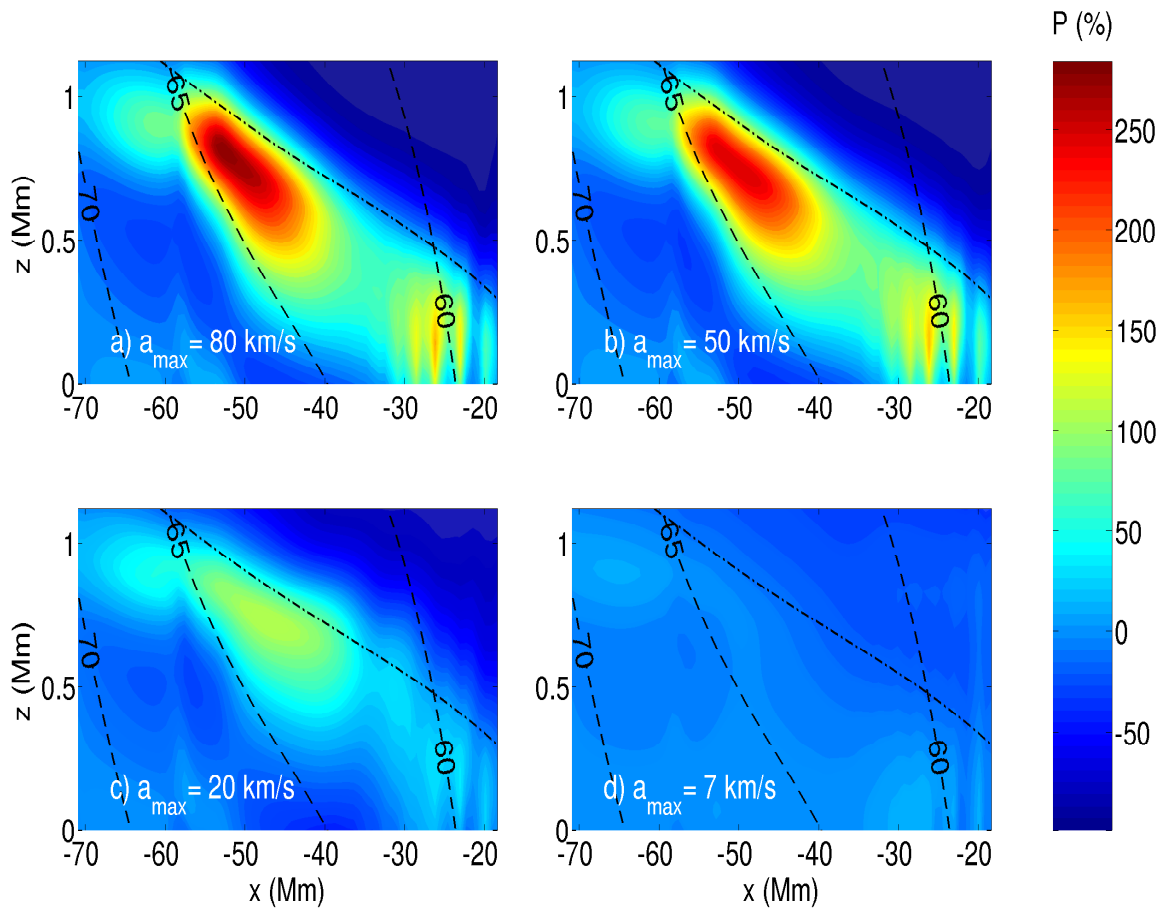


Figure 2.13:  $P_{6.5}$  for the 4 cases of simulation with  $a_{\max} =$  a) 80 km/s, b) 50 km/s, c) 20 km/s and d) 7 km/s. Once again the dot-dashed curve is the  $a = c$  layer and the thick dashed labelled curves are contours corresponding to the labelled magnetic field inclinations with respect to the vertical.

point such that waves cannot reflect and refract. The lack of any enhancement indicates that the halo is manifested purely as a result of waves which have refracted and reflected downwards through this overlying  $a > c$  atmosphere.

Finally, we present a comparison of the enhancement structure for differing sunspot field strengths (figure 2.14). The comparison shows  $P_{6.5}$  for the standard  $B = 1.4$  kG case (top panel) and for a simulation where everything was kept identical except that the peak field strength of the sunspot was doubled to around 2.8 kG (bottom panel). In the case with the stronger 2.8 kG field, the halo is more spatially localised and its magnitude has increased by around 25%. The greater field strength has focused the fast wave enhancement into a more confined region due to the lower FWRH. The halo itself has also dropped slightly in height, corresponding to the lower  $a = c$  layer present in the stronger sunspot atmosphere.

### 2.4.3 Spectral structure

We conclude our wave pulse study with a brief examination of the spectral characteristics of the power enhancement. Observations of acoustic halo power exhibit quite a clear spectral behaviour. The velocity power appears to peak at higher frequency for greater heights of  $z$  between 140 and 400 km and exhibits a dual lobe structure with peaks at around 6 and 8 mHz (Rajaguru et al., 2013). It would be ambitious to believe that a simple pulse wave source as we have used could reproduce the bulk of the observational characteristics of the real halos, and in fact we leave such a comparison to the more realistic simulations in the following chapter. It is however still worth looking at the *unfiltered* acoustic power,  $P$ , as a function of height (above  $z = 0$  km) and frequency (shown in figure 2.15). In this case the power is averaged along the range of  $x$  points from  $x = -60$  Mm to  $x = -20$  Mm at each  $z$  height above the surface, which corresponds roughly to the horizontal halo extent.

A dual-lobe frequency structure is evident in the figure, peaking at 6.3 mHz and 7.6 mHz for heights between 0 to 800 km above the photosphere. The second enhancement lobe at 7.6 mHz is more compact than the lower frequency lobe, only appearing at heights greater than 300 km. The fact that such a simple wave pulse simulation reproduces many of both the spatial and spectral properties of

## 2.4. SIMULATION RESULTS

---

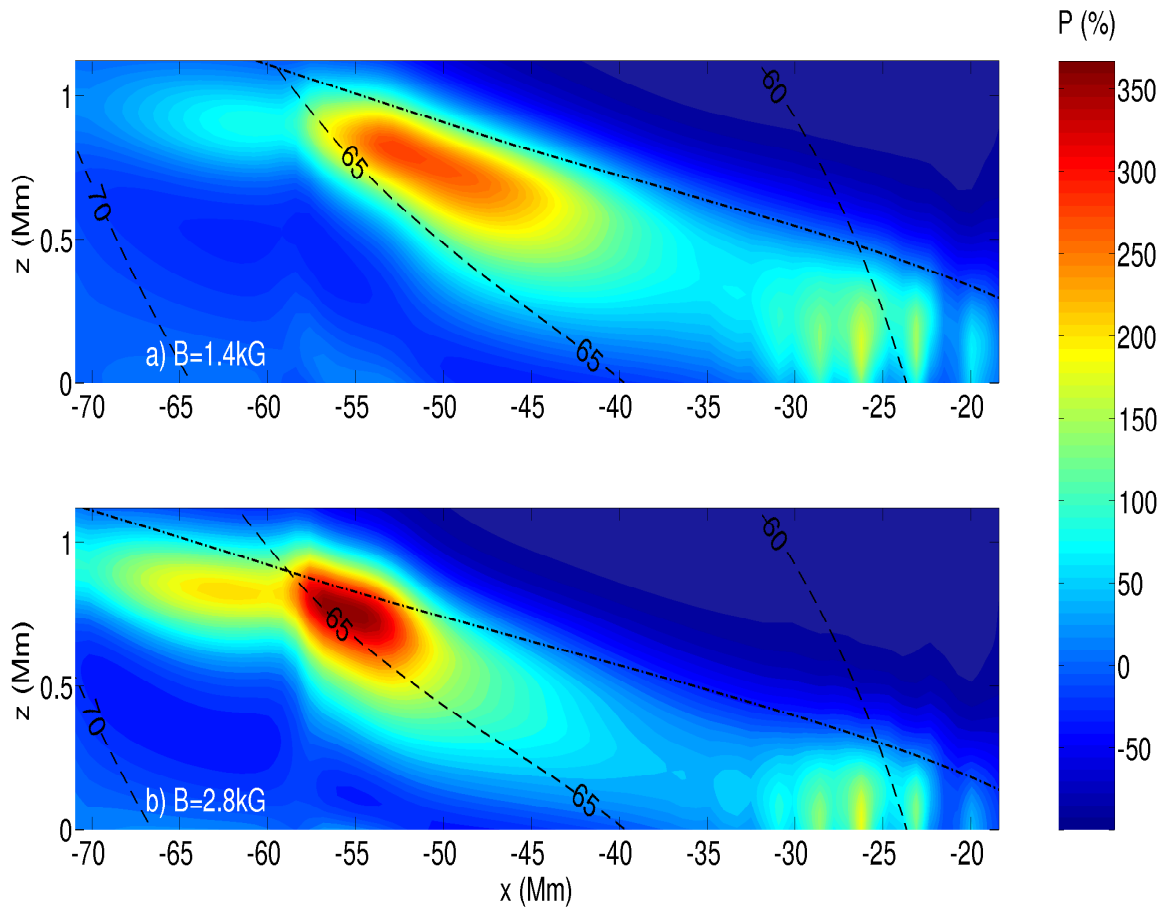


Figure 2.14:  $P_{6.5}$  for the simulations with peak surface fields of a) 1.4 kG and b) 2.8 kG.  $a_{\max} = 80$  km/s in both cases.

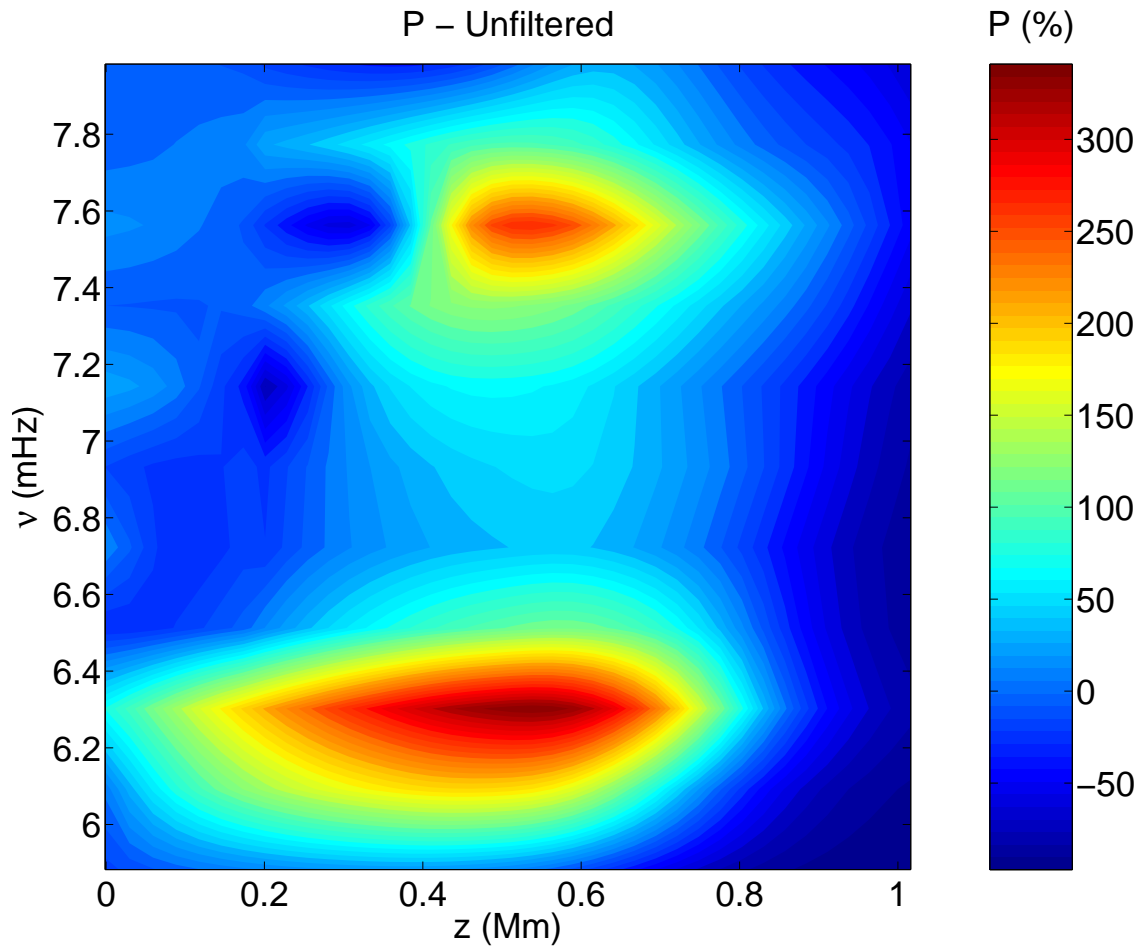


Figure 2.15: Unfiltered acoustic power  $P$  as a function of height, averaged over the points from  $x = -60$  Mm to  $x = -20$  Mm (the horizontal halo extent in figures 2.12-2.14).

acoustic halos observed in the actual solar photosphere and chromosphere is certainly encouraging.

## 2.5 What Can We Conclude?

The results of our simple MHS sunspot wave propagation simulations show a marked power enhancement (by a factor between 1.5 and 4) with respect to quiet-Sun values in the time averaged vertical component of velocity,  $v_z$ . The enhancement is present for relatively horizontal field (inclined 60 - 65 degrees from the vertical) which corresponds to weak field strengths of between 20-200 G (in the 1.4 kG sunspot atmosphere). Spectrally, the enhancement exhibits twin peaks at approximately 6.3 mHz and 7.6 mHz, with the 7.6 mHz frequency peak manifesting slightly higher in the atmosphere than the lower frequency peak.

These characteristics (apart from the magnitude of the enhancement itself) match those determined observationally when acoustic power maps of halo regions have been analysed (Schunker & Braun, 2011; Rajaguru et al., 2013), indicating that we can, with reasonable certainty, refer to the enhancement as an acoustic halo. It is interesting that these features are brought out in such simple simulations with a wave source that differs so significantly from the bath of stochastically excited acoustic modes present in the real solar photosphere. This fact suggests that the halo is a dynamic phenomenon brought about by the interaction of waves with the magnetic atmosphere, rather than any modification of the local acoustic oscillation frequency through granulation scale size shrinking (Jacoutot et al., 2008) or scattering effects (Hanasoge, 2009).

The hypothesis that we set out to investigate is that the acoustic halo is formed as extra energy is deposited into observable regions (in the photosphere and chromosphere) by downwards travelling fast waves that have refracted and reflected at the fast wave turning height. The idea was suggested and explored initially by Khomenko & Collados (2009). In the quiet-Sun, an upwards travelling high frequency (non trapped) acoustic wave will continue to propagate upwards and out of the local area, taking its energy with it. However, if there is a magnetic field present in the gravitationally stratified atmosphere, wave energy will branch into the fast-magnetic and

the slow-acoustic modes at around the  $a = c$  equipartition region. The slow acoustic waves in this case are the modes that take energy away along the field lines. The fast magnetic waves will continue to travel upwards while refracting until the condition for reflection (that  $\omega/k_h = a$ ) is met. It is these waves that would then be responsible for the excess energy. The fact that the power enhancement so closely correlates with the  $a = c$  layer (figures 2.12 - 2.14) supports this hypothesis. Furthermore, the halo magnitude scales with the value at which we cap the Alfvén speed, meaning that as we allow progressively more waves to return from the  $a > c$  atmosphere, the halo becomes more apparent; when we do not permit upcoming waves to return downwards from above the  $a = c$  layer, the halo disappears completely. This is the strongest evidence in favour of the mode conversion mechanism.

The halo structure itself shows no evidence of any small-scale variations in magnitude, like the groupings of enhanced emission evident in egression power maps of active regions known as ‘glories’ (Braun & Lindsey, 1999; Donea et al., 2000). This is most likely due to the simplicity of the monolithic field structure and wave source that we have utilised. It is likely that the small bead-like glories require less idealised magnetic configurations with more fine structure than we have used here.

We have not undertaken any analysis of intensity halos in this study, owing to the simple nature of the wave pulse that we have used. The calculation of intensities requires a strong and continuous wave source, and so in the following chapter we perform simulations with a more realistic stochastic and spatially homogeneous wave bath with which we can more rigorously conduct a comparison with observations.

## 2.5. WHAT CAN WE CONCLUDE?

---

**Monash University**

### **Declaration for Thesis Chapter 3**

#### **Declaration by candidate**

In the case of Chapter 3, the nature and extent of my contribution to the work was the following:

<b>Nature of contribution</b>	<b>Extent of contribution (%)</b>
Key ideas, development of code, modelling, production of all results, writing of paper	70

The following co-authors contributed to the work. If co-authors are students at Monash University, the extent of their contribution in percentage terms must be stated:

<b>Name</b>	<b>Nature of contribution</b>	<b>Extent of contribution (%) for student co-authors only</b>	
<b>Paul Cally</b>	Supervision and guidance		
<b>Hamed Moradi</b>	Co-supervision and guidance		
<b>Paul Rajaguru</b>	Observational collaborations		
<b>Sergiy Shelyag</b>	Assistance in development of models		
<b>Damien Przybylski</b>	Assistance in development of models		10%

The undersigned hereby certify that the above declaration correctly reflects the nature and extent of the candidate's and co-authors' contributions to this work\*.

**Candidate's  
Signature**

 **Date** 30/08/16

**Main Supervisor's  
Signature**

 **Date** 25/8/16

\*Note: Where the responsible author is not the candidate's main supervisor, the main supervisor should consult with the responsible author to agree on the respective contributions of the authors.

# Chapter 3

## Distributed Source Simulations

In the previous chapter, we performed 3D simulations to determine whether there was promise in the suggestion of Khomenko & Collados (2009) that it is in fact the *overlying* atmosphere that is directly responsible for the halo. Specifically that the addition of energy from high frequency non-trapped waves which have travelled above the Alfvén-acoustic equipartition ( $a = c$ ) layer and undergone mode conversion and refraction are responsible for the halo.

In this chapter we perform simulations in similar MHS sunspot atmospheres, however we now use a realistic distributed wave source, modelled as a slab of point sources at some depth below the photosphere. The sources are tuned to mimic the observed photospheric power spectrum, peaking at the 5 minute oscillation period ( $\nu \approx 3.3$  mHz) and exhibiting solar-like amplitudes. In this way we are able to compare the halos present in our simulations with observations in a more rigorous manner by simulating the constant  $p$ -mode bath of the solar photosphere.

For the observational comparisons we use a subset of the data corresponding to a single active region (NOAA 11092) from Rajaguru et al. (2013) which provides a multi-height velocity and intensity halo data set with which to compare our simulations.

### 3.1 Approximating the Photosphere with SPARC

We once again use the SPARC code for our distributed source forward modelling with two primary sunspot atmospheres similar in nature to those described in chapter 2. Some parameters of the sunspots (such as the field inclination with height) are slightly altered as compared to the two previous versions, however we still have both a weak (1.4 kG) and a strong (2.7 kG) field atmosphere, where the peak field values refer to the value on the sunspot axis on the photosphere ( $z = 0$ ). Once again we define an umbral and a penumbral radius arbitrarily, choosing those points to be where the field is inclined at  $45^\circ$  and  $60^\circ$  from the vertical respectively.

We also apply an Alfvén limiter at  $a_{\max} = 90$  km/s this time to fully ensure that we are not interfering with the majority of fast waves which have travelled above the  $a = c$  layer. We have taken care to ensure that this modification to the atmosphere will not affect the photospheric fast waves, which are given the necessary space to refract back downwards as they naturally would before the limiter takes effect. In this regard, simulations have been run with Alfvén limiter values of up to  $a_{\max} = 200$  km/s, with no change to the observed wave properties at our relatively low observation heights

Figure 3.1 shows a cut through the centre of the 2.7 kG sunspot atmosphere this time (along the plane at  $y = 0$ ). Overlaid are the  $a = c$  and  $a = 90$  km/s contours, as well as the observation height of the Fe I 6173.34 Å spectral line, which is located approximately 140 km above the photospheric surface. The vertical inclination contours show the rather rapid drop-off in field inclination, with the field reaching 30 degrees from the horizontal some 20 Mm from the umbra (at the surface). One can see that the structure of the strong field atmosphere is somewhat different to that of the weak case (in figure 2.6). In particular the  $a = c$  layer dips well below the photosphere in the umbra in this case, which is to be expected.

The computational domain in both cases is again square in the horizontal with 256 points in each of the  $x$  and  $y$  directions (where  $L_x = L_y = 200$  Mm) yielding a horizontal spatial resolution of  $\Delta x = 0.78125$  Mm. There are 220 grid points in the vertical direction, with spacings scaled by the local background sound speed. The box extends from a depth of 10 Mm below the surface to 2.5 Mm above it. As we

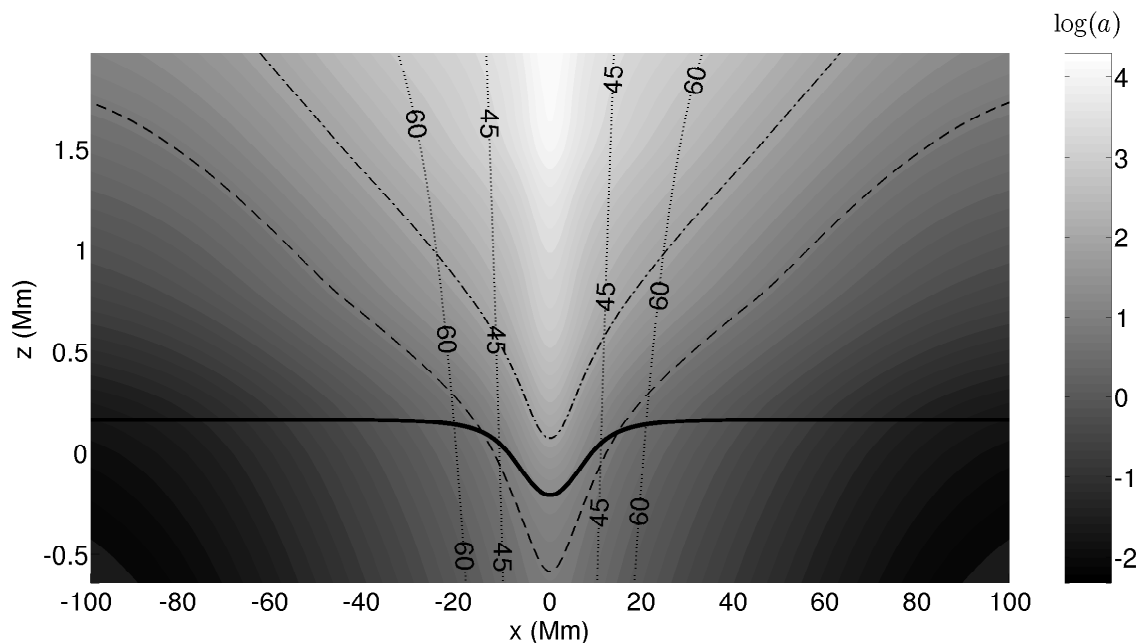


Figure 3.1: A cut through the sunspot center. Field inclination contours are shown for typical umbral/penumbral and penumbral/quiet sun values of 45 and 60 degrees from the vertical respectively. The  $z = 140$  km Doppler velocity observation height is shown by the solid black curve. The dashed curve is the  $a = c$  equipartition layer for this atmosphere and the dash-dotted curve is the  $a = 90$  km/s layer, where the Alfvén limiter is in effect. The background contour is  $\log(a)$  in km/s as it would appear without any Alfvén limiter in application. In our simulations  $a$  is constant above the  $a = 90$  km/s curve. Note that the aspect ratio of the figure is highly stretched, with the horizontal dimension spanning 200 Mm and the vertical spanning only around 2 Mm.

are using a plane of distributed sources instead of a localised pulse for driving waves, the implementation of the side boundary conditions must be altered somewhat; we apply periodic side boundary conditions, which is effectively implying that our simulation box is embedded in a larger region of the sun and that returning waves from either boundary are just incoming waves from outside of the box.

This time, in order to aid simulation stability there are both damping sponges and PMLs in effect along the top and bottom boundaries of the box. The top 20 and the bottom 8 grid points are taken up by these sponges and the PML, resulting in a maximum useable box height of 2 Mm above the surface.

#### **The distributed wave source**

Regarding our wave source function, we are attempting to model the uncorrelated stochastic wave field seen on the solar photosphere, rather than a single time dependent pulse. This wave field is in reality generated by subsurface convective cells. We choose a depth of 150 km below the surface and initiate a source function,  $S$ , in the right hand side of the momentum equation, in the manner of Hanasoge et al. (2007), i.e.

$$S(x, y, z, t) = \hat{S}(x, y, t)f(z). \quad (3.1)$$

In this case the horizontal function  $\hat{S}(x, y, t)$  is a plane of spatial delta functions which are excited at a cadence of 30 seconds, and the function  $f(z)$  is a gaussian function in depth with FWHM of approximately 100 km centered at a constant geometrical depth of 150 km below the surface. The source power spectrum has been tuned such that it more-or-less fits the spectrum of power observed on the surface of the quiet sun.

Panel a) of figure 3.2 displays this spectrum, which exhibits a peak in power at around 3.3 mHz. The spectrum has a slightly more extended high-frequency tail than that of our wave pulse source from chapter 2, with non-zero power present until above 10 mHz. Panel b) shows the power ridges in  $\ell$ - $\nu$  space calculated from 6 hours of  $v_z$  output at the surface. The simulated ridges in this case match the observed photospheric equivalents quite well and one can see that the fuzzy low- $\ell$  region, present in chapter 2 from using side absorbing boundaries, is gone. It is

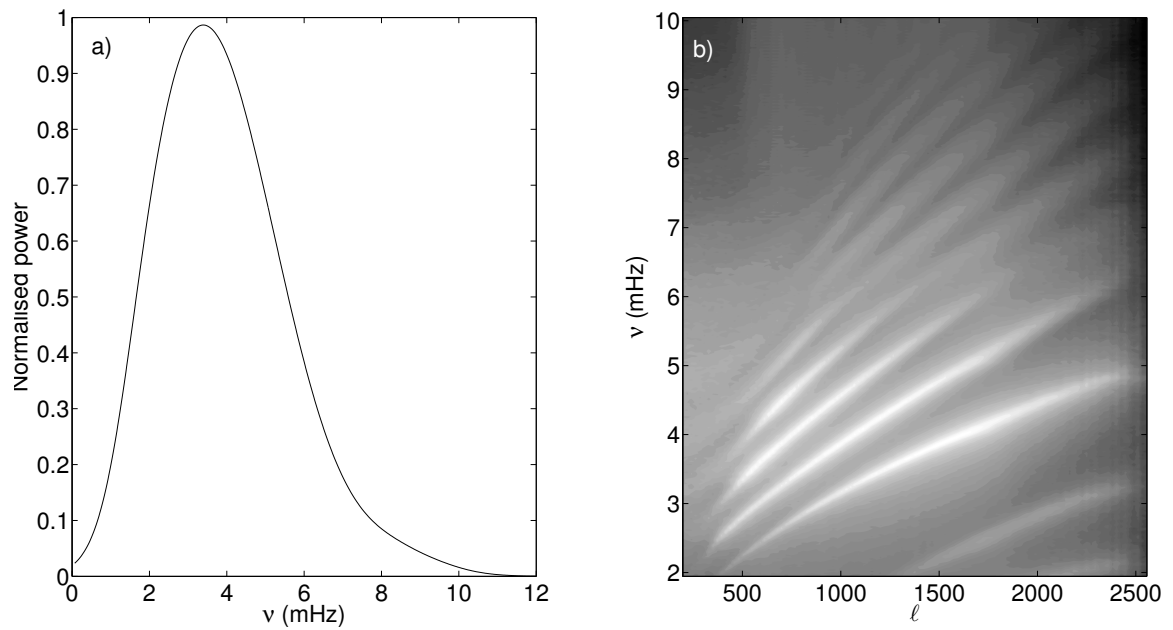


Figure 3.2: Panel a): The power spectrum of the wave source function used, tuned to provide a solar-like peak. b:) Arbitrarily normalised power ridges in  $\ell$ - $\nu$  space for 6 hours of simulation time, calculated at the surface ( $z = 0$ ) from  $v_z$ .

important to note that there is some variation in the power ridge structure as a function of chosen source depth. With the distributed source plane located at lower depths of between 400 km to 1 Mm (instead of 150 km) there was some damping of the ridges at moderate frequencies of 3-4 mHz. We found that by choosing a shallower source depth this damping took effect at higher frequencies (above 9 mHz) and left the bulk of the power ridges unaffected. In this chapter we stick to a source depth of 150 km, we do *not* perform a halo property analysis with respect to varying source depth, although this would be an interesting effect to look at in the future.

In taking into account the fact that strong umbral fields inhibit subsurface convection and wave propagation, we do not excite waves in the umbra of the sunspot itself. Instead we smoothly suppress the source amplitude as the magnetic field strength increases. In achieving this suppression we simply measure the value of  $B_z$  at all points in the plane corresponding to the source depth and then smoothly reduce the amplitudes of the sources at vertical field strengths which are deemed to be approaching the umbra.

In these simulations wave propagation is initiated and run for 8 hours of solar time in total using both the 1.4 kG and 2.7 kG sunspot atmospheres (as separate simulations). Most of our analysis will involve the stronger 2.7 kG atmosphere however, with the weaker spot used primarily for comparison. We disregard approximately the first 2 solar hours of simulation data as this is the period when the wave field is reaching an equilibrium and saturating the entire box. Once the RMS of the velocity levels out at around 2 hours, we begin to include the data, leaving us with 6 solar hours of usable time.

## 3.2 Extracting Observables

We analyse the power manifested in synthetic intensities corresponding to the 5000 Å continuum intensity, the AIA 1700 Å and 1600 Å intensity bands as well as both the vertical and horizontal components of the velocity perturbation ( $v_z$  and  $v_h$  respectively), which correspond observationally to the line-of-sight components of velocity when observing at disk centre ( $v_z$ ) and at the limb ( $v_h$ ).

In reality, the HMI Doppler camera (Scherrer et al., 2012) measures velocities

from the Fe I 6173.34 Å line, which has its peak of formation at a height of around 140 km (Fleck et al., 2011; Rajaguru et al., 2013), while the AIA (Lemen et al., 2012) 1700 Å and 1600 Å wavelength intensity channels are formed at approximate heights of 360 km and 430 km respectively (Fossum & Carlsson, 2005; Rajaguru et al., 2013). Thus, in comparing the structure of power enhancements present in our simulations with the observed power behaviour from Rajaguru et al. (2013) we extract simulation velocity signals from a height of  $z = 140$  km. We then calculate the synthetic intensities corresponding to the two above AIA channels as well as the 5000 Å continuum intensity for the full 6 hours of simulation time.

The approximate 1600 Å and 1700 Å intensities are calculated by interpolating the ATLAS9 continuum and line opacity tables (Kurucz, 1993) using the plasma parameters from the simulation and integrating them together with the corresponding LTE source function along the lines-of-sight for each column in the sunspot models. The routine used for the intensity calculations is similar to that of Jess et al. (2012). The filter bandwidths are set to 10 Å for both simulated AIA channels. No line-of-sight velocity or magnetic field information is used in this radiation intensity calculation. As observations show, the acoustic halo is a phenomenon especially sensitive to  $|\mathbf{B}|$  and to the local field inclination,  $\gamma$ . We firstly demonstrate here some of the similarities and differences between our idealised 2.7 kG sunspot and the real active region we have chosen for comparison.

Figure 3.3 compares the topology of  $|\mathbf{B}|$  and the unsigned field inclination from the vertical ( $\gamma$ ) at the surface of our 2.7 kG sunspot atmosphere and that of NOAA 11092. For the observations of NOAA 11092,  $|\mathbf{B}|$  is calculated from the disambiguated vector maps with components  $B_x$ ,  $B_y$  and  $B_z$ .  $\gamma$  in degrees is then simply defined as  $\gamma = 90 - (180/\pi)|\arctan(B_z/B_h)|$  where  $B_h = \sqrt{B_x^2 + B_y^2}$ . As can be seen in the figure, the peak field strengths of the two spots are similar, with the field strength of NOAA 11092 dropping off in a similar manner to the artificial sunspot; however the small scale features present in the real active region introduce many variations in both the field and its inclination which are not modelled in our simulations. The behaviour of  $\gamma$  around NOAA 11092 with radius for example is not the smooth monotonically increasing function yielded by the 2.7 kG sunspot model. We can therefore expect some differences between observed and simulated halo structure. Overall however

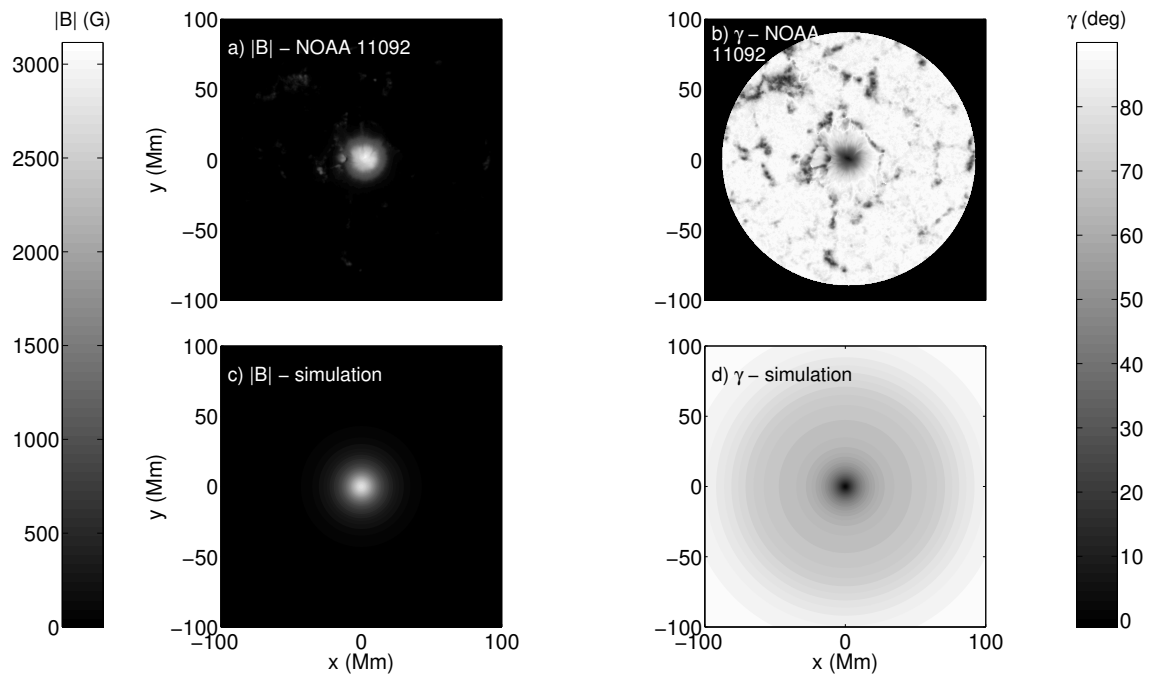


Figure 3.3: Panels a) and b) show  $|\mathbf{B}|$  and the unsigned field inclination from vertical ( $\gamma$ ) respectively for NOAA 11092. Panels c) and d) are the counterpart plots for the 2.7 kG simulated sunspot atmosphere over the same spatial scale.

NOAA 11092 is a reasonably symmetric and well-behaved sunspot, which is why it was chosen for comparison.

### 3.3 Comparisons with Observations

To begin our analysis we compare the 6 hour averaged acoustic power for  $v_z$  - from both the weak (1.4 kG) and strong (2.7 kG) sunspot atmosphere simulations - with the 14 hour time averaged Doppler velocity power from the HMI observations of NOAA 11092.

Frequency filtered power maps are shown in figures 3.4 and 3.5 for a range of frequencies of interest. The frequency filters are equivalent to those shown in figure 2.7 of chapter 2, except centred around the 4 indicative frequencies 4.5, 5.5, 6.5 and 7.5 mHz. The power at every point has been divided by the average power of a quiet corner of the simulation domain (at the same height and frequency range), in order to represent an enhancement over quiet values. In both simulations, the enhancement comes into effect at around 5 mHz, when waves are in the non-trapped regime, just as in the observations.

The differences between the two sunspot simulations (rows 1 and 2) are immediately evident, with the 2.7 kG sunspot exhibiting a larger umbra. A consequence of having a stronger magnetic field strength is also that the  $a = c$  height will be lower in the atmosphere, resulting in a spreading of this contour for a particular observation height. It is clear that the halo appears correlated with the  $a = c$  contour (green circles) in both cases, manifesting outside of the  $a = c$  equipartition layer, as in the pulse simulations of chapter 2. An intriguing feature of the simulated halos is the clear dual-ring structure present for higher frequencies (figure 3.5). The inner ring appears to conform qualitatively well at a glance with the observational halo. However the simulation enhancement appears to be interrupted by a region of mild power deficit with respect to the quiet sun (the dark moat in between the two halo rings at 6.5 and 7.5 mHz).

Although not entirely obvious in the NOAA 11092 power maps here, observed halos do exhibit a similar dual-ring structure when observed at increasingly high frequencies, though the structure is significantly less prominent than in our

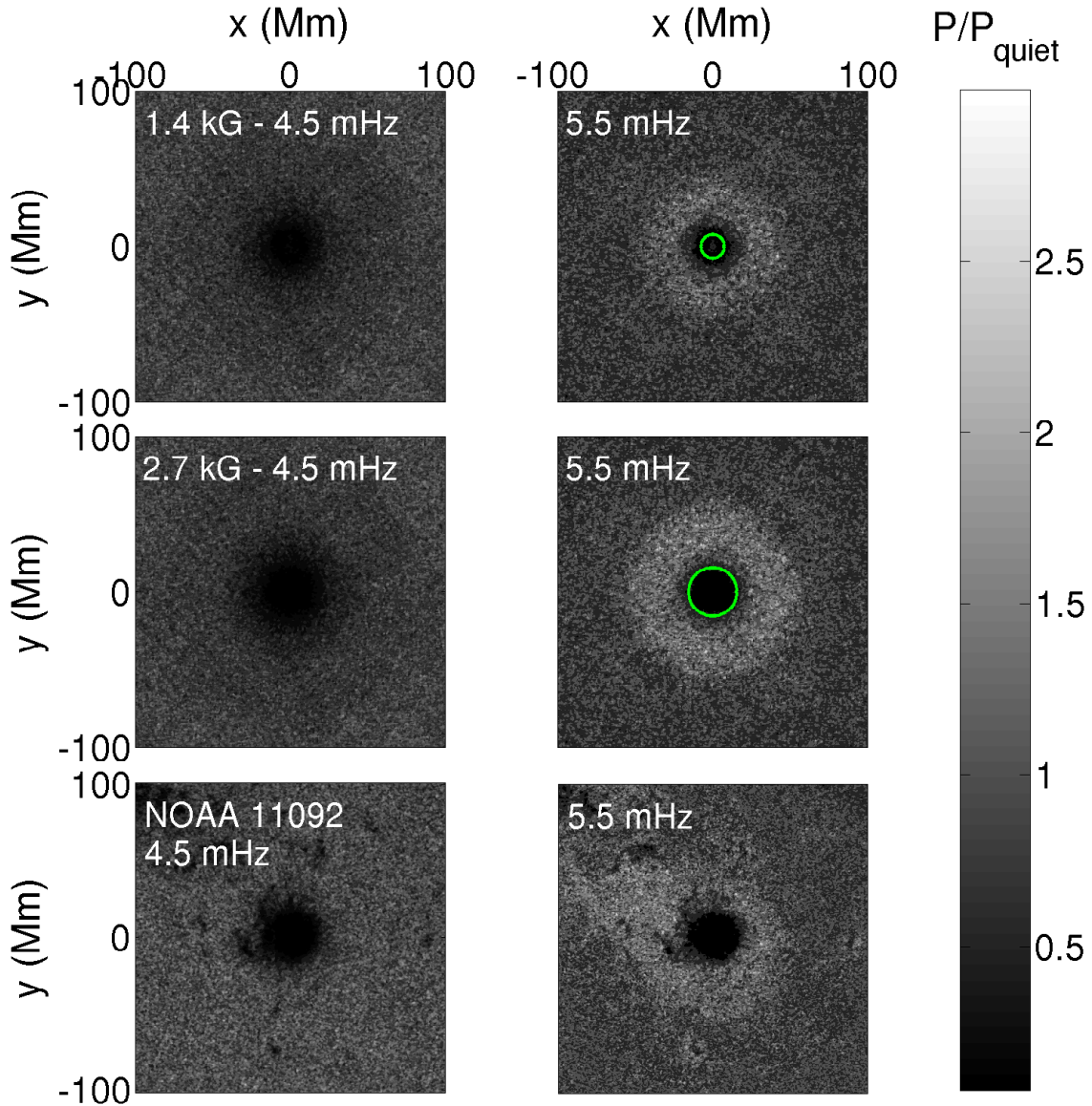


Figure 3.4: Top row: 6-hr time-averaged  $v_z$  power maps at the height of formation of the Fe I 6173.32 Å line ( $z = 140$  km) for two illustrative frequency ranges for the weak (1.4 kG) sunspot atmosphere. Middle row: The same power maps for the strong-field (2.7 kG) case. Bottom row: 14-hr time-averaged observational Doppler velocity power maps of the active region NOAA 11092 for the same frequency ranges. The green contour in the simulation rows is the  $a = c$  contour at the height  $z = 140$  km.

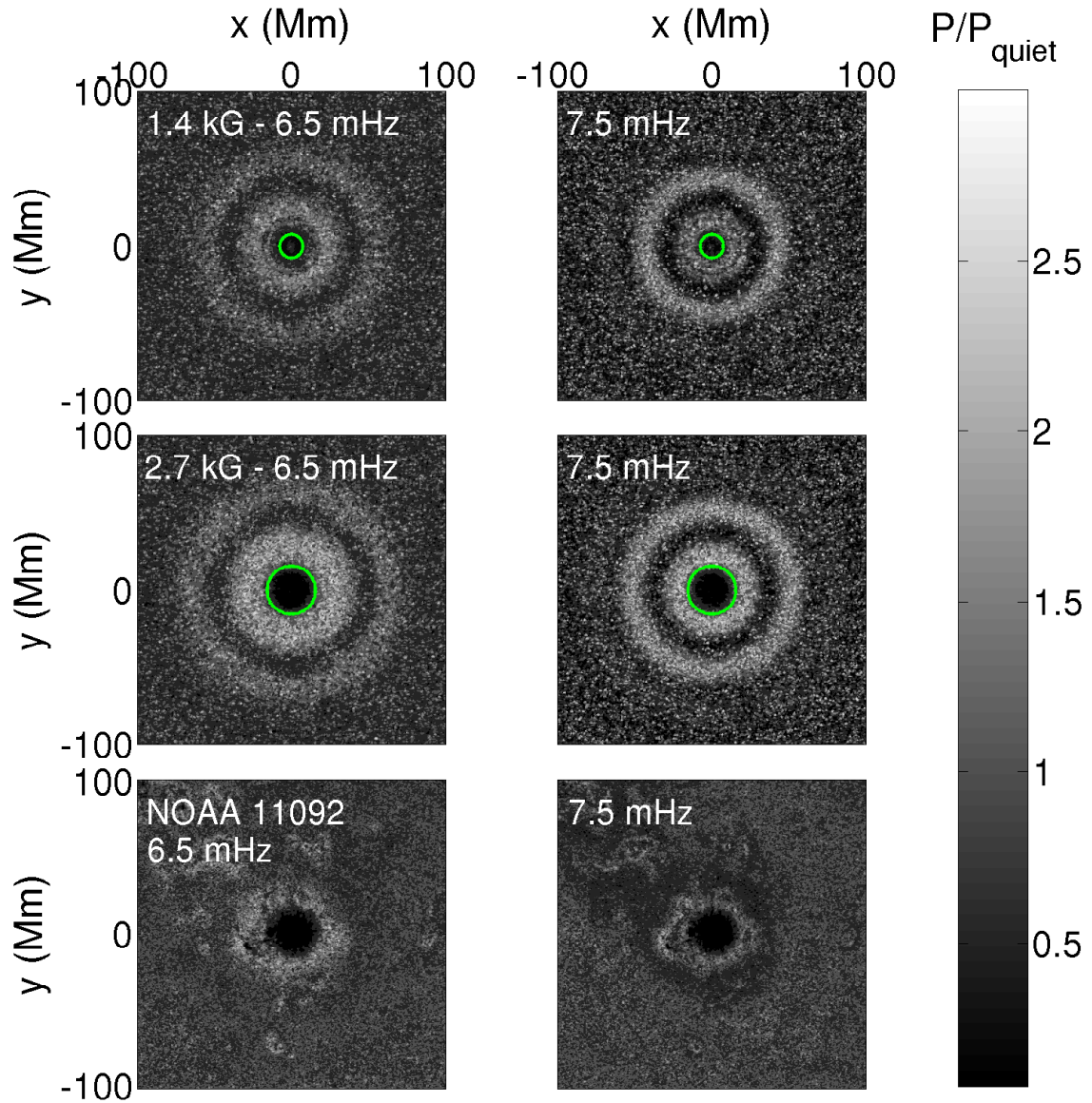


Figure 3.5: The same power maps as figure 3.4 except filtered around the higher frequencies 6.5 and 7.5 mHz.

simulations. This feature can clearly be seen in power maps of observed Doppler velocity in Rajaguru et al. (2013) (shown as figure 2.2 in chapter 2 of this thesis) and in Hanson et al. (2015) (figure 2 in that work) at 8 and 9 mHz respectively.

We shortly discuss how fast-Alfvén mode conversion may likely lead to this dual-ring structure, both in our simulations and on the solar surface.

#### 3.3.1 Spectral structure

Comparing power maps in this way is of only so much use however. To more rigorously compare the structure of observed and simulated power halos we examine the *unfiltered* power enhancements as functions of  $|\mathbf{B}|$  and  $\nu$  (i.e. no frequency filter is applied during the Fourier transform). In this way we may fully examine the spectral structure of the halo, in a similar manner to the analysis performed in Rajaguru et al. (2013).

Figure 3.6 shows the unfiltered power enhancement corresponding to both the horizontal and vertical components of the velocity. The  $v_z$  (top) panel corresponds directly to the power maps in the middle rows of figures 3.3-3.5; it is the same data, but simply unfiltered in frequency space and so is inclusive of the entire spectral structure. The bottom panel shows the power calculated from the horizontal velocity component at the same height as the  $v_z$  power. The power at every point has been binned according to the local value of  $|\mathbf{B}|$  so as to reveal not only the spectral structure of the halo but also how it behaves with respect to field strength.

The first thing to notice in figure 3.6 is that the simulated  $v_z$  power structure matches up reasonably well with what we have seen in the power maps; the halo has formed over relatively weak field ( $50 \text{ G} < |\mathbf{B}| < 700 \text{ G}$ ) as expected. In the simulation sunspot atmosphere,  $|\mathbf{B}|$  decreases (and  $\gamma$  increases) smoothly and uniformly as a function of umbral distance. As such this field strength range corresponds to nearly horizontal inclinations of  $55^\circ < \gamma < 75^\circ$ . This of course agrees with all other observational reports of enhancements which place the halo amongst moderate to weak and horizontally inclined field (Jain & Haber, 2002; Schunker & Braun, 2011; Rajaguru et al., 2013).

The  $v_z$  dual-ring structure can clearly be seen at higher frequencies in the

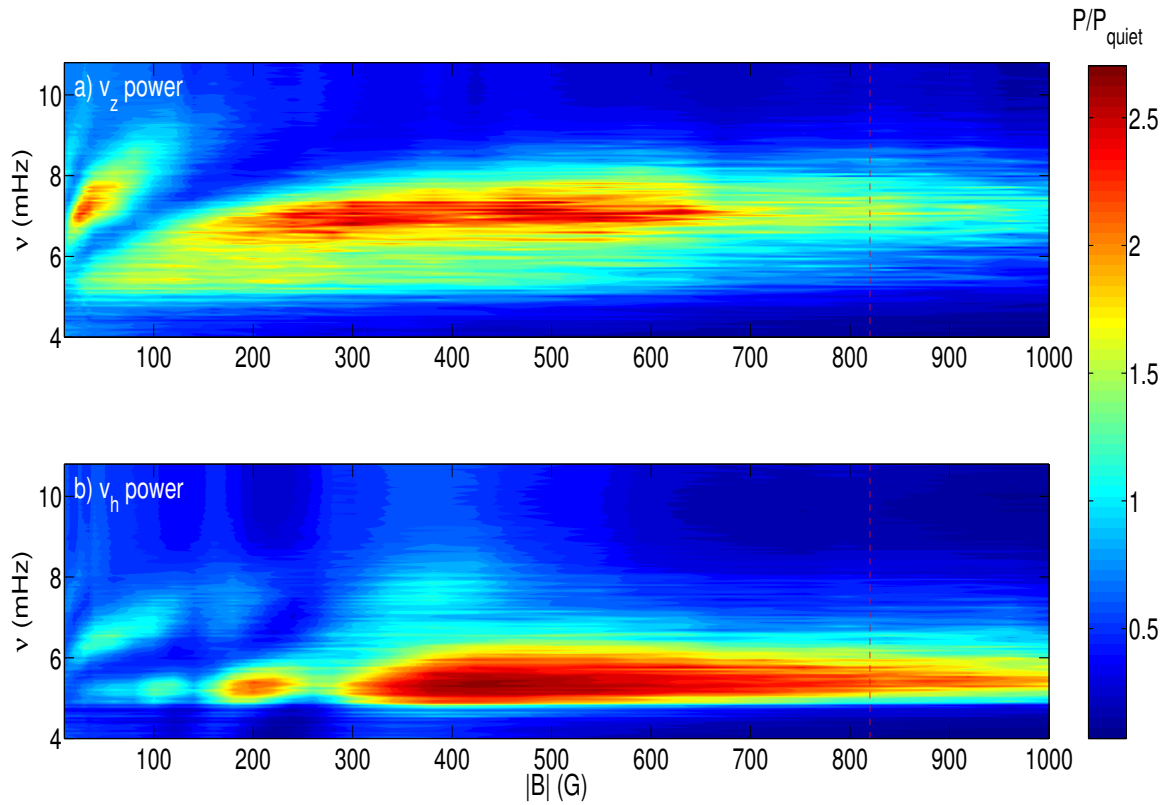


Figure 3.6: Panel a) is the unfiltered Fourier power of  $v_z$  binned according to the local field strength at the  $z = 140$  km observation height for the 2.7 kG atmosphere. Panel b) is the equivalent quantity for the horizontal velocity component,  $v_h$ . The dashed vertical line is the position of the  $a = c$  at the same height.

### 3.3. COMPARISONS WITH OBSERVATIONS

---

figure, manifesting as the second lobe of enhancement for very weak field. Wedged between the two lobes (from around  $(|\mathbf{B}|, \nu) = (100, 6)$  to  $(200, 8)$ ) is the region of power reduction which is seen in the power maps of figure 3.5 as the dark ring in-between the halo.

Interestingly, the  $v_h$  enhancement (bottom panel) is largely weak or non-existent amongst the outer horizontally inclined field where the  $v_z$  halo and the associated dual-ring structure is prevalent (in the region  $|\mathbf{B}| < 300$  G in the figure). This is very much expected and strongly supports our hypothesis; amongst horizontal field an upcoming fast wave with a large  $v_z$  component (compared to its  $v_h$  component) will mode convert efficiently to a fast (magnetic) wave at the  $a = c$  layer. This wave will refract and reflect at its reflection height and undergo secondary mode conversion on the way down once again. The wave will again efficiently convert to the fast acoustic wave which will contribute to the excess power measured at those horizontal-field locations.

The fast-to-fast conversion will be efficient in both cases because the largely  $v_z$  wave will form a significant attack angle with the horizontal field, although there will of course be some energy loss to the field-aligned slow mode. Conversely a more horizontally aligned wave will form a weaker attack angle with the largely horizontal field during both episodes of mode conversion leaving significantly less returning fast wave energy to be deposited and measured at photospheric heights. In general the opposite will be true for more vertical field, which is why there is a  $v_h$  enhancement at preferentially *higher* field strength than the  $v_z$  enhancement. The field inclination is more vertical at stronger field radii, which results in a larger attack angle between  $v_h$  and the field.

It is of course somewhat difficult to determine the wave type given only the direction of the oscillation in general; the direction of  $\mathbf{v}$  for the fast and slow waves with respect to  $\mathbf{k}$  and  $\mathbf{B}$  depends on whether the atmosphere is magnetically ( $a > c$ ) or hydrodynamically ( $a < c$ ) dominated. It would however be extremely useful if there were any center-to-limb observational studies of halo features focusing on the low- $\beta$  photosphere, so that we could compare the horizontal Doppler component with our  $v_h$ . Zharkov et al. (2009) and Przybylski et al. (2015) have performed analyses of umbral power features as functions of observation angle, but as yet, no such studies

focusing on halo properties have been conducted.

### Multi-height comparisons

We now move on to a more complete comparison between our simulations and observations. Extending on the power map comparisons 3.4-3.5 we present a multi-height halo comparison for both velocities and intensities.

Figures 3.7-3.9 show comparisons between power structures for NOAA11092 and the 2.7 kG atmosphere simulation. The right panel of figure 3.7 is the same  $v_z$  power plot as in the previous figure (with a different aspect ratio), and the left panel is the equivalent for the observed Doppler velocity power for NOAA 11092. The first thing to notice is that the simulated  $v_z$  power structure matches up reasonably well with the observed Doppler power structurally. The NOAA 11092 halo has formed over similar relatively weak ( $50 \text{ G} < |\mathbf{B}| < 700 \text{ G}$ ) and inclined field as expected. Notably, the dual-ring structure is not evident in the NOAA 11092 observational

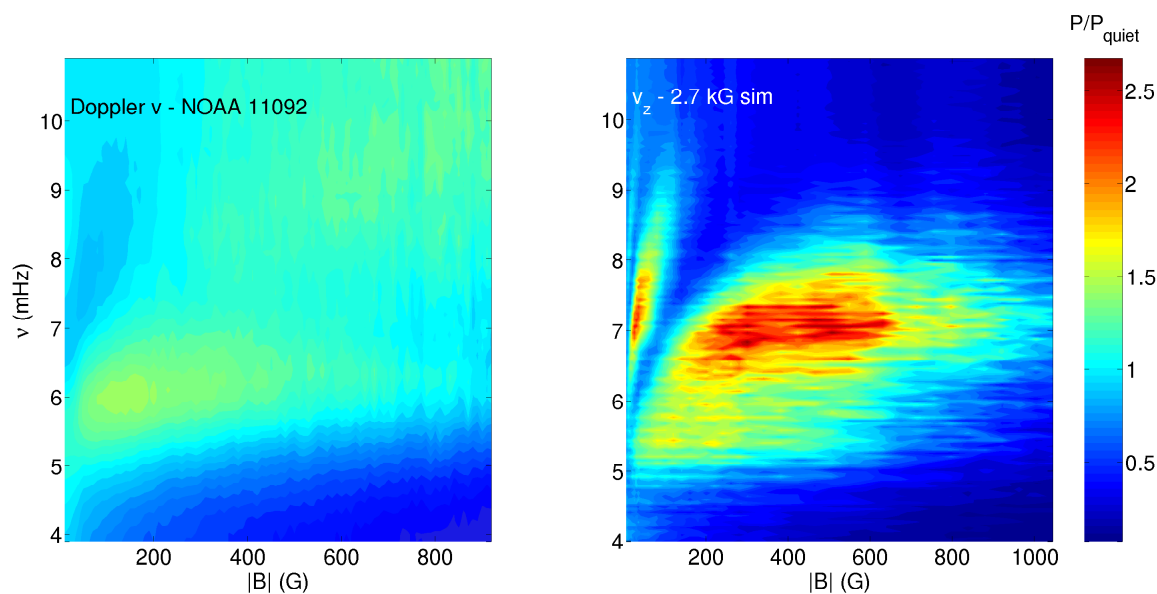


Figure 3.7: Unfiltered Doppler velocity power enhancement for NOAA 11092 (left panel) and unfiltered  $v_z$  power enhancements for the 2.7 kG simulation (right panel) as functions of  $|\mathbf{B}|$  and  $\nu$ . Note that the sunspot centre is located far to the right of these plots ( $|\mathbf{B}| \approx 2700 \text{ G}$ ), with the regions external to the spot at the left (in the weak field).

### 3.3. COMPARISONS WITH OBSERVATIONS

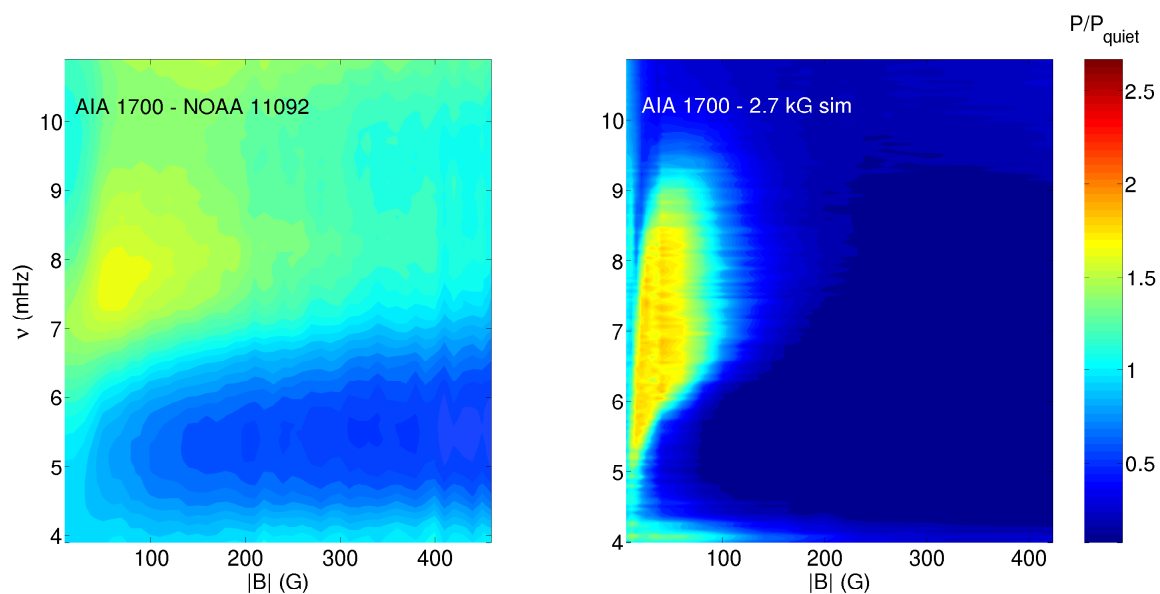


Figure 3.8: Unfiltered observed (left panel) and synthetic (right panel) AIA 1700 power enhancement as functions of  $|B|$  and  $\nu$ .

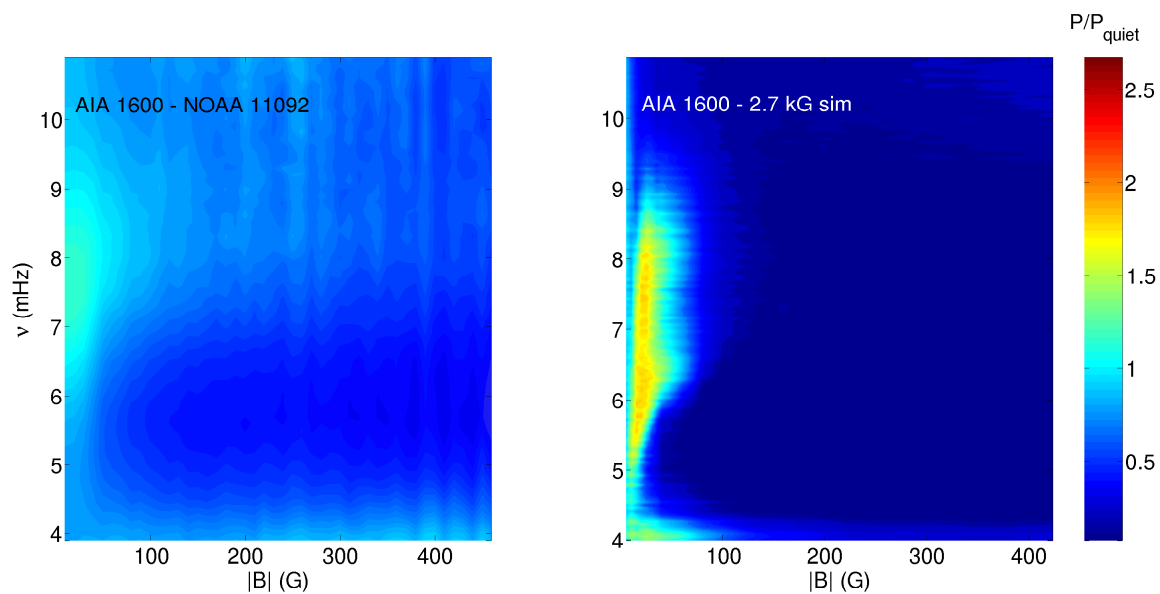


Figure 3.9: Unfiltered observed (left panel) and synthetic (right panel) AIA 1600 power enhancement as functions of  $|B|$  and  $\nu$ .

panel in this case. It is however evident in the similar plots of Rajaguru et al. (2013), which are shown in chapter 2 as figure 2.3. In the HMI V panel (corresponding to the Doppler velocity) of that figure the pixels have been binned according to the local field inclination before the power was calculated and plotted against the field strength. These plots represent averages over 4 different active regions which exhibit a much less symmetrical structure than our ideal simulation sunspot. In the nearly-horizontal field case (top-right panel) there is a noticeable dual-ring power feature. The regular inner halo stops at around 100 G and then begins to form again faintly at around 50-60 G. This is the diffuse outer halo seen in the corresponding power maps extending out to the quiet-Sun. We have not binned the NOAA 11092 power according to inclination however, which is why the dual-ring structure is not immediately visible in figure 3.7.

Looking at greater heights in the form of the AIA 1700 Å and 1600 Å intensities (corresponding to heights of 360 km and 430 km above the base of the photosphere respectively) we also see a general agreement in  $\nu, |\mathbf{B}|$  space. The spreading of the magnetic canopy at these heights has resulted in the intensity halos forming at much weaker field locations both in the observations and the simulations.

The magnitudes of the enhancements in the simulations are consistently larger than the observed values, as is evident in these figures. This is a feature that was also noted in chapter 2 (and in Rijs et al. (2015)) and can most likely be attributed to the fact that our sunspot is symmetric and its magnetic field inclination is a steep, monotonically decreasing function of radial distance. The MHS structure is such that horizontal field is enforced at the side boundaries of the simulation domain and so there is a large expanse of nearly horizontal field. The fast-slow mode conversion mechanism for the generation of the halo relies on a large attack angle between wavevector and field and so, in analysing  $v_z$  power enhancements, it is reasonable to expect that this horizontal field will be very conducive to the conversion of energy into magnetic fast waves and hence, a prominent halo. We will discuss this discrepancy further at the end of the chapter.

Power derived from the 5000 Å intensity continuum (at  $z = 0$ ) was also calculated synthetically to compare with the observational intensity continuum power. It is well known that halos do not appear in measurements of intensity continuum

power and we also found this to be the case in simulations, with no enhancement present.

#### Chromospheric phase shifts

Another interesting result is the comparison between observed and simulated phase shifts at chromospheric AIA heights. A net upward or downward propagation of waves in an atmosphere can be diagnosed by calculating the temporal cross-spectrum of any wave quantity sampled at two different heights. For example, for velocities  $v(z_1, t)$  and  $v(z_2, t)$  sampled at two different heights  $z_1$  and  $z_2$ , the phase shift corresponding to a height evolution of the wave is given by the argument or phase of the complex cross-spectrum,

$$\phi_{1,2}(\nu) = \arg[\mathbf{V}(z_1, \nu)\mathbf{V}^*(z_2, \nu)],$$

where  $\mathbf{V}$  is the Fourier transform of  $v$ . In the above convention, a positive phase-shift would mean that the wave is propagating from height  $z_1$  to  $z_2$ , while the opposite holds for a negative phase-shift.

The phase shift contour maps of figure 3.10 describe the phase shifts of waves at the AIA 1700 Å and 1600 Å intensity formation heights with respect to those waves at  $z = 0$  (at the height of formation of the intensity continuum). The simulation yields a clean band of positive phase shifts at halo frequencies with respect to those at the surface at weak field regions. The same basic pattern is seen in the observations, however there is some extended phase shift structure at higher field strengths in the AIA 1700 Å power which is not replicated in the simulation. The simulation phase shifts are also of a greater magnitude than observations - particularly in the case of the AIA 1600 intensities.

These variations in features are not too surprising given that NOAA 11092 exhibits a much more rapid horizontality of field away from the umbra than seen in the MHS model. The physics of fast-*Alfvén* mode conversion is also strongly tied to the local magnetic field inclination. Therefore the reason that NOAA 11092 exhibits such an extended phase shift structure into higher field regions (and our MHS sunspot does not) may be in part due to the more horizontal field at those radii for the active region. We discuss shortly how these bands of positive phase shifts

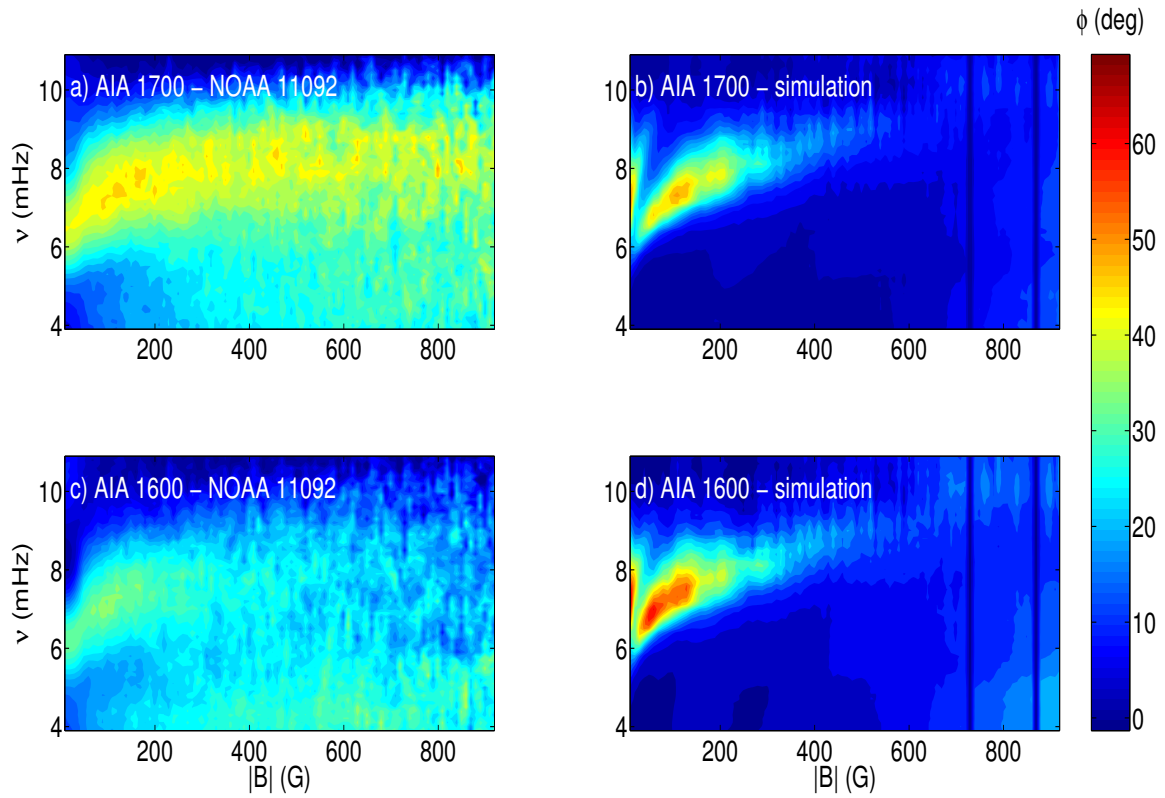


Figure 3.10: Phase shifts at the heights of formation of the AIA 1700 Å and 1600 Å lines of all waves with respect to those at the surface. Panels a) and c) correspond to observations and b) and d) to the 2.7 kG simulation.

at given observation heights may be intrinsically related to the process of fast-Alfvén mode conversion.

### 3.4 The Halo Formation Mechanism

In order to further convince ourselves that the halo is produced by the return of reflected fast waves, we revisit the proof-of-concept test which we applied in chapter 2 (and in Rijs et al. (2015)). In a similar manner we perform several identical simulations to the 2.7 kG case examined above, except with incrementally sticter Lorentz force limiter values. By reducing the height of the artificial cap on the atmosphere we are allowing less and less room for fast waves to refract and deposit extra energy onto observable heights. The atmosphere above the cap has a roughly uniform Alfvén speed and as such, waves that impinge on this altered region will simply travel upwards and out of the local area. As the standard 2.7 kG simulation which we have analysed so far had a value of  $a_{\max} = 90$  km/s, we run simulations with  $a_{\max} = 40$ , 20 and 12 km/s and analyse the power in a similar manner to figure 3.7, i.e. as a function of  $|\mathbf{B}|$  and  $\nu$ .

The progression is shown in figure 3.11. Panel a) is the standard case  $a_{\max} = 90$  km/s. In the intermediate cases of panels b) and c), the severity of the Alfvén speed cap is increased to 40 and 20 km/s respectively, which correspond to caps at *lower* heights above the  $a = c$  layer. In these cases it is clear that the magnitude is reduced as the more vertically oriented waves are escaping to the top of the box, yielding contributions from only the more horizontally inclined waves. Panel d) corresponds to the case where the limiter is only barely above the  $a = c$  height. In this case the mode conversion process itself is largely unaffected, however upwards travelling fast waves are entirely prevented from refracting, reflecting and returning down to the  $z = 140$  km observation height at which we measure the  $v_z$  halo. This is a similar result to that shown with a simple pulse wave source in the previous chapter; here however we have shown that the entire halo spectrum is entirely dependent on the return of reflected fast waves, rather than just those at 6.5 mHz originating from a specific location.

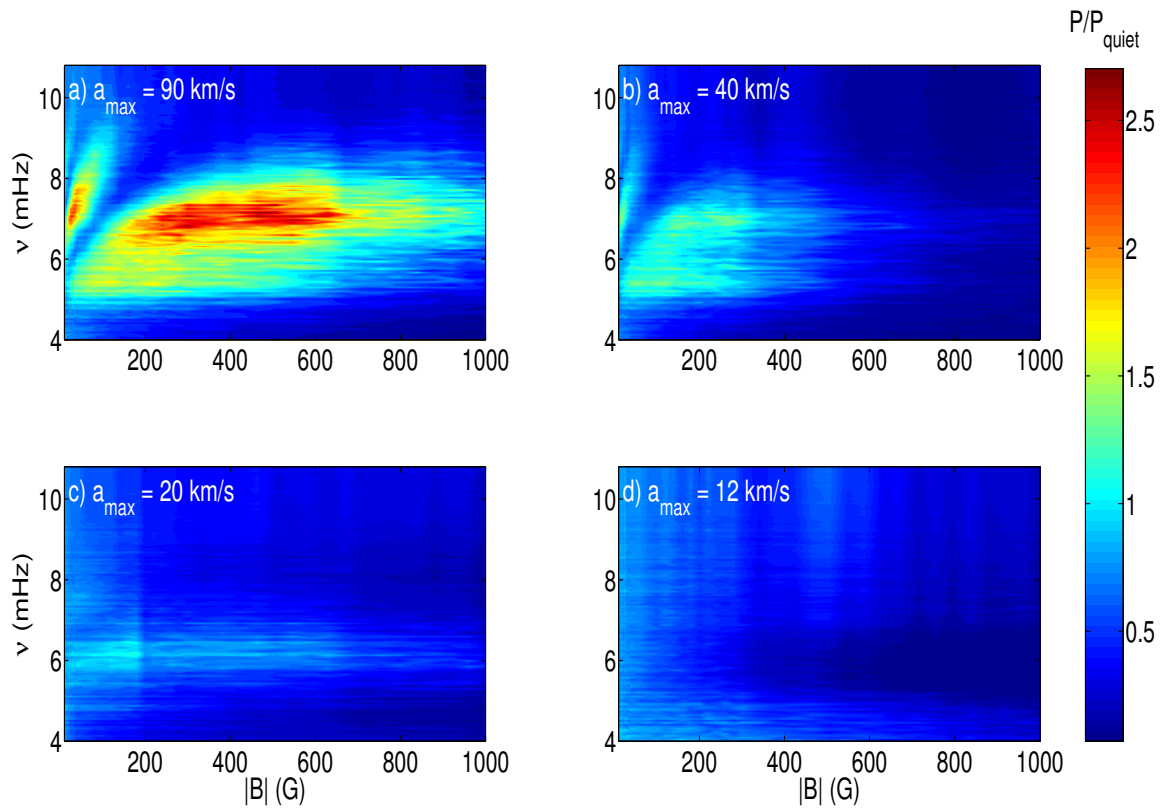


Figure 3.11: Panel a): Unfiltered  $v_z$  power halos in the case  $a_{\text{max}} = 90$  km/s. Panels b), c) and d) show the same quantity from simulations with progressively stricter values of  $a_{\text{max}}$ .

## 3.5 Fast-Alfvén Conversion and Halo Structure

Finally, and perhaps most importantly, we attempt to explain the dual-ring power enhancement structure examined earlier and seen in observations (albeit weakly).

In figure 3.12 we compare  $v_z$  power (once again at the standard observational height of 140 km) for both the 1.4 kG and the 2.7 kG simulations with the phase shifts at the same height. The phase shifts in this case are those calculated at  $z = 140$  km height, with respect to waves at  $z = 0$ , so we are only looking at the phase shifts that the waves experience over a height change of 140 km in the simulation (as opposed to the phase shifts of figure 3.10). The black curves have been added simply by eye to aid in the comparisons here. In both simulations there is a similar phase shift pattern to that observed in both the simulated and observed intensities at greater heights, however the magnitude is less here as the waves have travelled a shorter vertical distance.

The key fact to note is that the strong branch of positive phase shifts in the left panels corresponds precisely to the region between the dual rings of power enhancement. This enhancement gap in  $|\mathbf{B}|, \nu$  space is the dark ‘moat’ seen between the two halo rings at high frequency in the simulation power maps. The halo enhancement region itself shows no real phase shift which most likely indicates a mixture of upwards and downwards travelling waves. This is to be expected at high, non-trapped frequencies as waves rise upwards towards the  $a = c$  layer and are refracted back downwards. The halo structure itself does not appear to change too significantly with respect to the peak magnetic field strength of the model, apart from the noted correlation with the  $a = c$  layer. We certainly do not see any noticeable change in the peak halo frequency as a function of field strength.

The pertinent question to ask then is: why are there only upwards travelling waves (denoted by the positive phase shifts) in the moat between the concentric halos? The answer would appear to lie in the process of fast-Alfvén mode conversion, the basics of which are described in Cally (2011) and Cally & Hansen (2011) and which we spend some time explaining in the opening pages of chapter 4.

Fast-Alfvén mode conversion has been well studied in both sunspot-like (Moradi & Cally, 2014; Moradi et al., 2015) and simple magnetic field geometries;

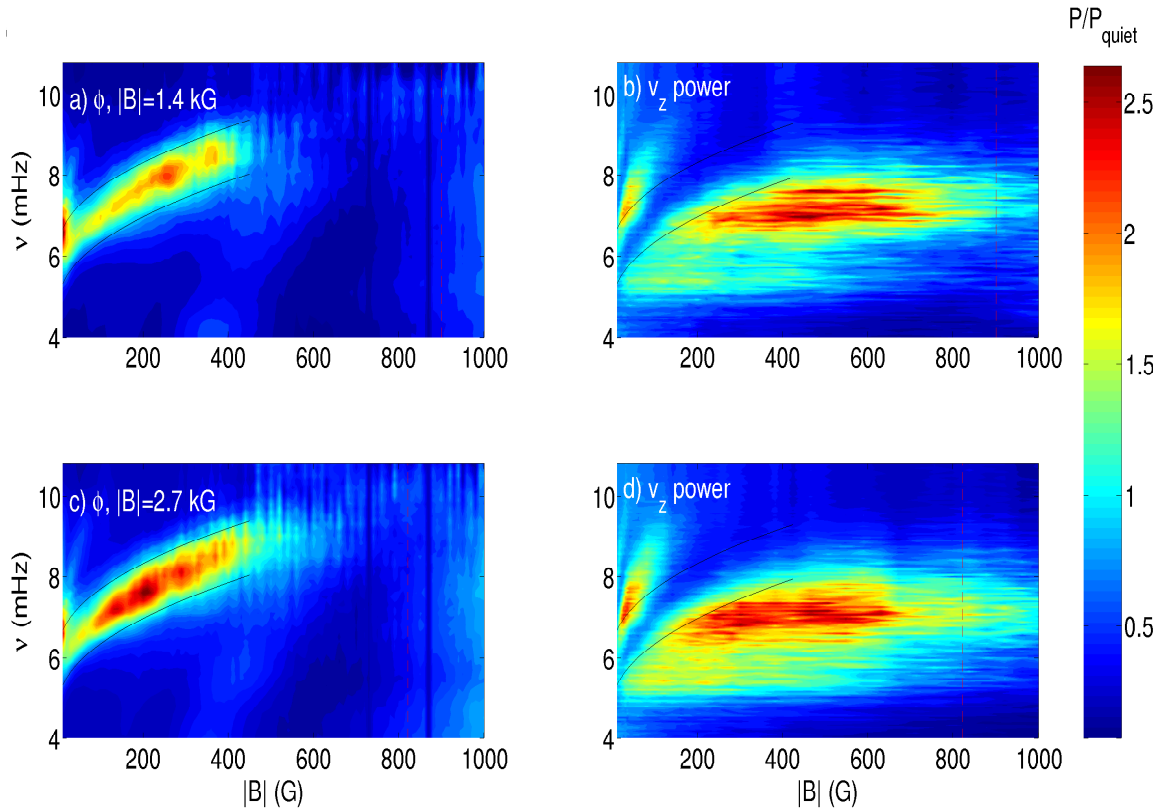


Figure 3.12: The top row corresponds to the weak field simulation, with peak field strength 1.4 kG, and the bottom row is from the strong field case (2.7 kG peak). On the left are phase shifts calculated at  $z = 140$  km in height. On the right are the standard binned and unfiltered  $v_z$  power distributions. The black curves are drawn by eye to denote where the phase shifts would be in the power plots. Once again, the dashed vertical line is the position of the  $a = c$  for the  $z = 140$  km observational height.

Several works (Verth et al., 2010; Terradas et al., 2010; Pascoe et al., 2011, 2012; Goossens et al., 2013) have studied the damping of transverse kink waves in terms of the associated Alfvén resonance and Cally & Goossens (2008) and later Khomenko & Cally (2012) have conducted parameter studies with monochromatic wave sources and simple inclined field magnetic structures. The findings of the latter two works were that fast wave energy is converted to the field-aligned Alfvén wave at favoured field inclinations and wavevector-to-field attack angles. The process is also strongly dependent on both  $\nu$  and  $k_h$ .

In the case of our distributed source simulations, waves exhibit a distribution of wavenumbers and frequencies in a similar manner to the quiet-Sun and so the picture is somewhat muddled in comparison to such simulations. We can however expect that fast-Alfvén conversion will in some way act on fast waves as they reach the Alfvén resonance near their upper turning point (on the order of a few hundred kilometres above the  $a = c$ , depending on  $k_h$ ). As the halo appears to be generated by downwards turning fast waves, we would anticipate that some of this returning energy may be lost to the field aligned Alfvén wave, which will follow the local field lines until reaching the top (or the side) of the simulation domain and being absorbed there.

By examining power maps we noted the strong concentric halos and the gap of power enhancement in between them. Figure 3.12 shows this more comprehensively and associates this dark ring with a strong positive phase shift. We suggest that the reason that the halo is not one continuous region of enhancement is that for specific field inclinations, fast mode energy is lost to the Alfvén wave; fast-Alfvén mode conversion depletes the returning fast wave at locations where the conversion is most efficient and the fast wave is therefore unable to return to observation heights.

Figure 3.13 suggests this to be the case. Each panel of the figure corresponds to a specific frequency filtering. The top halves of the panels are the same as the panels in the middle row of figures 3.4 and 3.5, i.e. filtered power maps corresponding to the 2.7 kG simulation at the Doppler velocity observational height of 140 km. The bottom halves of the panels show the magnetic energy associated with the Alfvén

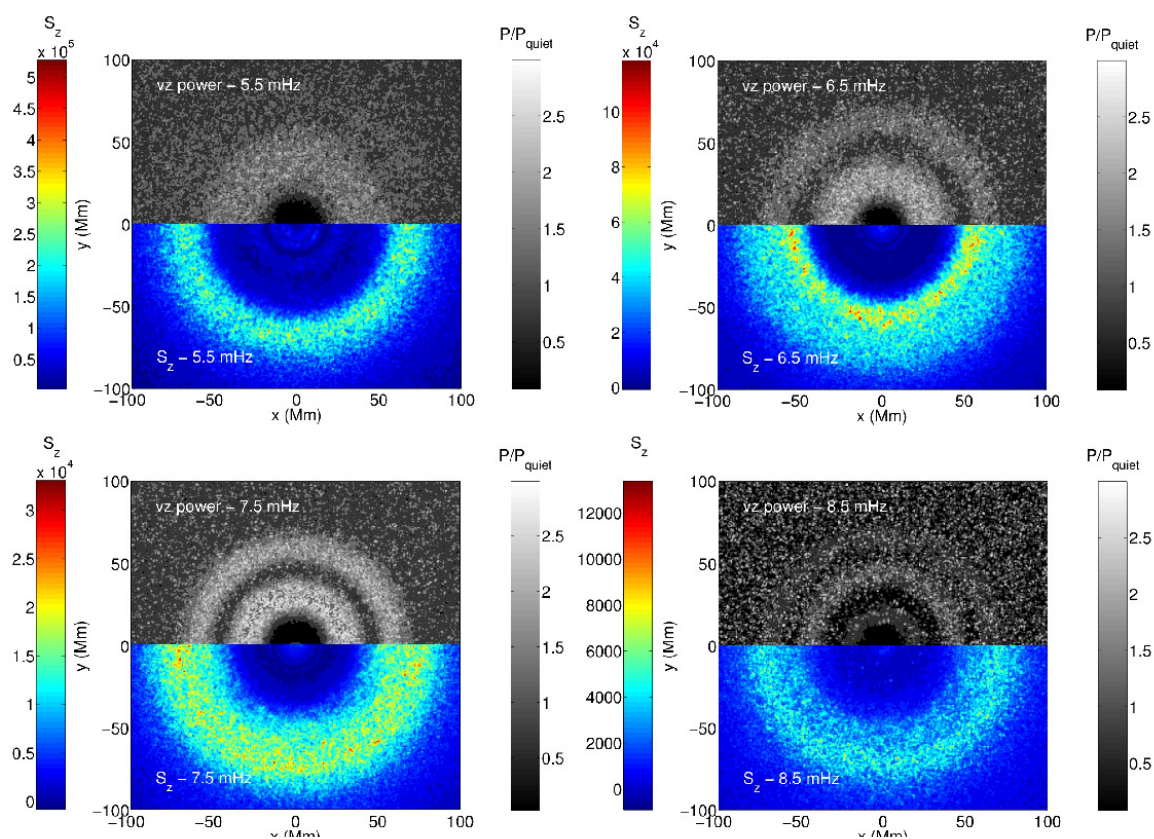


Figure 3.13: Power map - Poynting vector composites. The top halves are  $x$ - $y$  power maps at  $z = 140$  km, filtered around the respective frequencies. Bottom halves are  $S_z$  in units of  $\text{ergs}/\text{m}^2\text{s}$ , calculated at  $z = 2$  Mm. Note that the Poynting vector scaling is not consistent from plot to plot, as there is significantly less energy arriving at the top of the box for each subsequently higher non-trapped frequency range.

wave in the form of the Poynting vector,  $\mathbf{S}$ , where

$$\mathbf{S} = \frac{1}{4\pi}(-\mathbf{v} \times \mathbf{B}) \times \mathbf{b}, \quad (3.2)$$

where  $\mathbf{v}$  and  $\mathbf{b}$  indicate the perturbations to the velocity and the background field respectively. The bottom panels show the vertical component of the vector,  $S_z$ , corresponding to the upcoming Alfvén flux, and are calculated at the very top of the simulation domain, at a height  $z = 2$  Mm, just before the PML comes into effect at the top of the box. In each case the velocity has been pre-filtered around the associated frequency range prior to the calculation of  $S_z$  to match the power maps.

It is worth remembering that we have applied a cap to  $a$  above  $a = 90$  km/s in the atmosphere and so any upwards travelling Alfvén waves will encounter our modified atmosphere and travel at a constant speed to the top of the box, instead of being subject to a rapidly increasing Alfvén speed. The correlation between the Alfvén flux and the position of the dark ring is immediately noticeable, especially in the 5.5 and 6.5 mHz cases. Note that upwards travelling Alfvén waves will follow the field and that there is some field spreading with height in this MHS atmosphere which is why  $S_z$  is diffuse and does not align precisely with the dark ring at observation heights. It seems clear that this Alfvén wave energy is responsible for the strong band of positive phase shifts (and thus upwards travelling waves) in the dark moat; there is no fast wave energy left to return downwards and contribute to the halo at these radii and field inclinations. Furthermore this provides support for the fast-slow mode conversion halo mechanism rather strongly as the two processes are critically interlinked.

## 3.6 Discussion and Ramifications

Linear forward modelling in realistic MHS sunspot atmospheres has yielded acoustic halos that match up quite well with observations, both spatially and spectrally. Apart from the magnitudes of the enhancements themselves, most observed features seem to be reproduced in our simulations, not just when comparing Doppler and vertical velocities, but also intensity halos at multiple heights in the chromosphere. As in the observations we see no power enhancement in calculations of the time-averaged

intensity continuum power.

We have also presented convincing evidence that the mechanism responsible for halo formation is the refraction and return of magneto-acoustic fast waves at non-trapped frequencies. The halo appears very sensitive to the position of the  $a = c$  layer in the atmosphere, which is the critical location for fast-wave mode conversion. With our realistic distributed wave source, we see a strong relationship between the strength of the halo and the extent to which fast waves are allowed to return downwards. This suggests that the halo is completely governed by the overlying  $a > c$  atmosphere and the extra energy injected to observable heights by these returning fast waves.

The theory also predicts that an enhancement should be present in the power of  $v_h$ , as this component will also interact with the field, and that this enhancement should be concentrated toward more vertical field (as the horizontal component makes a larger attack angle with vertical field); this was shown to be the case as well. Unfortunately center-to-limb observational studies of the halo do not yet exist and so we cannot compare this horizontal velocity halo to the real thing.

Our simulations are performed in a MHS atmosphere, solving the linear MHD equations and using a wave excitation mechanism that approximates the wave bath of the solar photosphere. The fact that we see halos in such simulations (which are of course, entirely non-radiative and do not in any way include convective effects) suggests that the halo is not created by any convective cell-magnetic field interaction as suggested by Jacoutot et al. (2008). Similarly, the idea of Kuridze et al. (2008) that  $m > 1$  waves may become trapped in magnetic canopy structures cannot occur in our simulations as the field configuration is horizontally enforced at the boundaries and there is therefore no downwards oriented canopy. The scattering mechanism of Hanasoge (2009) also cannot explain why the magnitude of the halo is determined entirely by the structure of the overlying atmosphere, as we have seen here.

As noted throughout chapters 2 and 3, the primary difference between our simulated halos and those actually observed in the photosphere and chromosphere is the magnitude of the enhancement itself. Observed Doppler velocity halos have magnitudes up to 60% (over the quiet sun average at the same height). Our simulated  $v_z$  halos are greater than this by a factor of 2 or even 3, depending on frequency. There

are several possible explanations for this discrepancy. As we have postulated, the halo enhancement most likely occurs as a result of fast waves interacting with the sunspot magnetic field at large attack angles. This yields a large conversion fraction to the fast magnetic wave which refracts and deposits additional energy in the photosphere and chromosphere. The penumbral field structure of active regions differs significantly from the simple MHS model used here however. Our atmosphere does not explicitly include an umbra or penumbra, but rather consists of a smoothly decreasing field strength and vertical inclination component, yielding significant regions of smooth, nearly-horizontal field. Non-trapped waves that reach the  $a = c$  equipartition layer will have a large vertical component and so we would expect these waves to interact strongly with primarily horizontal field. In nature, penumbrae contain fine structure, with bright and dark filaments giving rise to the now well-observed combed magnetic field configuration (Scharmer et al., 2002; Bellot Rubio et al., 2004). At the outer penumbral boundary, studies have shown up to a  $60^\circ$  difference in field inclination between dark (largely horizontal) and light (largely vertical) filaments (Weiss et al., 2004; Thomas et al., 2006). Energy corresponding to waves interacting with nearly vertical field at these radii would therefore be lost, transmitting primarily to the slow magneto-acoustic mode. This would have an overall effect of weakening the halo, and as these features are not represented in our model, they may be a contributing factor for our high halo magnitudes.

Another factor to consider is the non-ideal nature of the photosphere, which contains a large neutral component (Krasnoselskikh et al., 2010; Khomenko & Collados, 2012). In our ideal MHD assumption we assume full ionization, and thus neglect any dissipative effects brought about by ion-neutral collisions. It is conceivable that these partial ionization dissipative effects (as well as any other dissipation brought about by small scale magnetic structure) in the real photosphere and chromosphere may reduce the observed velocity and intensity halos.

With regards to intensity halos, figures 3.8 and 3.9 show a good agreement between the magnitudes of the observed and simulated AIA 1700 Å halo. However the observed AIA 1600 Å halo is very weak, in contrast to the simulation. This may be due to the larger height range over which observational intensities are calculated. In particular, the height over which the AIA 1600 Å intensity band is determined

observationally is some 185 km (centered at 430 km in height) (Fossum & Carlsson, 2005), which may have the effect of smoothing out the 1600 Å intensity power, given that the corresponding synthetic intensities encompass a much narrower height range.

In our final discovery of note, we have shown that fast-Alfvén conversion also plays a considerable role in the formation of the halo. This conversion of the fast wave at preferential field inclinations takes energy away along the field lines in the form of the transverse Alfvén wave, resulting in the dual-ring halo structure seen at high frequency. In our simulations this is visible at 6.5 mHz and above – the halo is essentially being broken up into two concentric rings by this Alfvénic energy loss. Observationally this may help to explain the underlying process responsible for the 8-9 mHz dual-ring power halo structure (Hanson et al., 2015; Rajaguru et al., 2013), with its spatially localized zone of enhancement, dark moat and diffuse structure.

Monash University

### Declaration for Thesis Chapter 4

#### Declaration by candidate

In the case of Chapter 4, the nature and extent of my contribution to the work was the following:

Nature of contribution	Extent of contribution (%)
Key ideas, development of code, modelling, production of all results, writing of paper	70

The following co-authors contributed to the work. If co-authors are students at Monash University, the extent of their contribution in percentage terms must be stated:

Name	Nature of contribution	Extent of contribution (%) for student co-authors only
Paul Cally	Supervision and guidance	

The undersigned hereby certify that the above declaration correctly reflects the nature and extent of the candidate's and co-authors' contributions to this work\*.

Candidate's Signature  Date 30/08/16

Main Supervisor's Signature  Date 24/8/16

\*Note: Where the responsible author is not the candidate's main supervisor, the main supervisor should consult with the responsible author to agree on the respective contributions of the authors.

## Part III

# Fast-Alfvén Conversion - A Twisted Approach

## Chapter 4

# Alfvén Waves in a Twisted Magnetic Field

In chapters 2 and 3 the process of fast-slow mode conversion and transmission was examined. We concluded that this wave conversion mechanism appears to play an almost-total role in the production of the acoustic halo at photospheric and chromospheric heights. We also showed that the spatial structure of the halo appears to be modified not only by fast-slow interactions but also by fast-Alfvén conversion. Specifically energy appears to be removed from the fast wave branch and converted to the field-aligned, incompressible Alfvén wave at favoured field inclinations. This Alfvén wave signal was found in simulations at heights well above the photosphere, manifesting itself in terms of the Poynting flux.

In this chapter we examine the fast-Alfvén conversion mechanism in the context of a gravitationally stratified cold plasma atmosphere threaded by a uniformly *twisted* (non-azimuthally symmetric) force-free magnetic field. The model is reasonably idealised and simple as we do not have a realistic MHS model of a twisted field to model in SPARC at this time. It is sufficient for our purposes however, as we shall show.

Our aim is to determine the extent to which the various magnetic field and wave parameters affect the efficiency of the conversion, with the goal being to help us to understand how twisted chromospheric fields may produce Alfvén waves which are known to exist in the high atmosphere and corona of the sun.

## 4.1 Background Discussion

In the following section we introduce and briefly discuss a little of what is known about waves in the upper-chromosphere and corona, in particular focusing on the magnetic field-aligned Alfvén waves and how they may be generated and reach such heights. Whilst the efficiency of fast-Alfvén conversion amongst uniform field has been well studied, there has been less work in a twisted field context.

We also introduce the theory behind the fast-Alfvén conversion process itself, which differs distinctly from the already discussed fast-slow conversion/transmission process.

### 4.1.1 Coronal wave observations

The properties of the three basic MHD wave-types (the compressional fast and slow MHD waves and the incompressible, transverse Alfvén wave) so familiar in a uniform plasma are somewhat more complicated at coronal heights where the atmosphere is magnetically dominated and the magnetic structure is focused into strong loops and filaments. In this tenuous low- $\beta$  atmosphere, magneto-acoustic waves interacting with magnetic structure, such as loops, are observed as either the axi-symmetric sausage ( $m = 0$ ) mode or the non-axi-symmetric kink ( $m = 1$ ) or fluting ( $m \geq 2$ ) modes (Spruit, 1982; Edwin & Roberts, 1983).

The *Transition Region and Coronal Explorer* spacecraft yielded detections of both flare-induced standing waves (Nakariakov et al., 1999; Schrijver et al., 2002; Aschwanden et al., 2002) and propagating oscillations (Berghmans & Clette, 1999; De Moortel et al., 2000; O’Shea et al., 2001) of coronal magnetic loops. The loop oscillations have been shown to decay quite quickly, on a time scale of only a few wave periods (approximately 10 to 15 minutes) (Nakariakov et al., 1999), yielding prolonged speculation as to the nature of the wave damping mechanism (De Pontieu et al., 2001; Goossens et al., 2002; Ofman & Aschwanden, 2002; Aschwanden, 2003; Van Doorselaere et al., 2004; Nakariakov & Verwichte, 2005).

More recently, via the *Coronal Multi-channel Polarimeter*, evidence was found of not only the above ephemeral oscillations, but also of an ever-present bath of coronal waves (Tomczyk et al., 2007; Tomczyk & McIntosh, 2009). These perturbations were

shown to be non-existent in measurements of intensity, leading to the conclusion that the waves are incompressible and therefore can be interpreted as Alfvén waves, although this conclusion is somewhat disputed (Van Doorselaere et al., 2008). The study of Van Doorselaere et al. (2008), which assumes a uniform plasma flux tube, does not take into account the fact that incompressible waves need not necessarily be axisymmetric however, a possibility which was uncovered by Goossens et al. (2009).

The detection of what may be Alfvén waves at these heights is intriguing as they are often invoked as a mechanism for coronal heating (Erdélyi & Fedun, 2007; Jess et al., 2009; van Ballegooijen et al., 2011; Asgari-Targhi et al., 2013; van Ballegooijen & Asgari-Targhi, 2016). It is well known that slow magneto-acoustic waves, which are prominent amongst coronal field, have only a small fraction of the necessary energy to heat the corona to observed temperatures (De Moortel et al., 2000) and in any case are prone to shock dissipation at lower heights. The Alfvén wave is sufficiently energetic however (see Browning (1991); Zirker (1993); Narain & Ulmschneider (1996) for some of the earlier discussion on possible coronal heating mechanisms, including heating by Alfvén waves).

There are difficulties involved in pinning coronal heating solely on the shoulders of Alfvén waves however. The first being to show that they can be generated in sufficient quantity to provide the necessary flux for the heating. Second, Alfvén waves do not dissipate their energy amongst loops easily, a property that is required in order for heating to occur.

It is also known that Alfvén waves generated at photospheric heights can be very efficiently reflected by the steep Alfvén speed gradient of the transition region. Cranmer & van Ballegooijen (2005) notably performed photospheric driving of thin-tube kink waves which merged into transverse Alfvén waves at some height *below* the transition region and found that some 95% of upwards travelling Alfvén wave energy flux was reflected downwards, returning to interact with the photospheric wave field.

The issue of the generation mechanism (and the height of generation) of the Alfvén wave itself however is an important one. Vranjes et al. (2008), modelling the photospheric plasma (in the single-fluid approximation) showed that the ionisation at such heights is insufficient for Alfvén waves of any reasonable strength to be generated as predicted in the ideal MHD approximation. Tsap et al. (2011) however

argue that the low ionization ratio of the photosphere does not hinder the generation of the waves provided wave periods are not too small ( $> 10^{-4}$  s). Zaqrashvili et al. (2011b) notes that the single-fluid approximation fails to model high-frequency waves with variations over timescales less than the ion-neutral collision time. For higher frequency magneto-acoustic and Alfvén waves two-fluid approximation yields a significant decrease in the damping of generated Alfvén waves. Additionally Soler et al. (2013) points out that the study of Vranjes et al. (2008) fails to include the neutral plasma component, which is significant in the strongly collisional photosphere. Ultimately the issue is at present still undecided.

Alternately, much analysis suggests that active region *chromospheres* may generate substantial Alfvén flux as fast waves hit their resonance height and undergo fast-Alfvén mode conversion (Cally & Andries, 2010; Cally & Hansen, 2011; Cally, 2011; Cally & Moradi, 2013). By virtue of not being forced to reflect in the presence of a steep stratification, the long-wavelength Alfvén oscillation can then reach coronal heights, following the shape of whatever field structure is present.

Verth et al. (2010); Terradas et al. (2010); Pascoe et al. (2011, 2012); Hood et al. (2013) and Goossens et al. (2013) have also modelled the spatial damping profiles of propagating and standing fast waves as they travel through cylindrical magnetic structures in low- $\beta$  plasmas, with the study of Goossens et al. (2013) specifically quantifying the energy flow of the damped waves. The works have also quantified the decay of the kink mode and found a correlation with the generation of an azimuthal Alfvén oscillation.

In regards to the issue of dissipation, there have been numerous mechanisms suggested in an attempt to describe how the Alfvén wave energy is expended in heating the field loops along which the waves travel. Studies using both monochromatic and pseudo-realistic frequency-distributed footpoint drivers, (De Groof & Goossens (2000); De Groof et al. (2002); De Groof & Goossens (2002) for example) have shown that resonant Alfvén waves produced by driven fast waves at the base of magnetic loops can dissipate effectively and contribute to the loop heating.

### 4.1.2 Fast-Alfvén mode conversion and resonant absorption

We begin with a clarification; what we refer to as fast-Alfvén mode conversion throughout is in general the same process as resonant absorption, a fact established by Cally & Andries (2010). A fast magneto-acoustic wave undergoing mode conversion and losing some energy to the Alfvén oscillation is essentially absorbed by an Alfvén resonance. We will be quantifying this lost energy and so in our case it makes more sense to speak in the context of mode conversion.

The study of fast-to-Alfvén conversion is unlike that of fast-to-slow conversion/transmission in that it is necessarily 3D in nature, requiring a wavevector angle that is out of the magnetic field plane. We can show this by considering a cold plasma atmosphere in  $(x, y, z)$  cartesian coordinates with a density stratification  $\rho(z)$  decreasing monotonically in the  $z$  direction and some uniform magnetic field  $\mathbf{B}$  oriented in say the  $x$  direction.

In a cold plasma the only restoring force is perpendicular to the field, and thus there can be no field-parallel displacement component ( $\xi_x = 0$ ). We can therefore write a linear wave displacement vector as

$$\boldsymbol{\xi}(x, y, z, t) = (0, \xi_y, \xi_z)e^{i(k_x x + k_y y - \omega t)},$$

after taking out the explicit  $t$  and  $y$  dependencies. The associated wave differential equation system is therefore

$$\begin{aligned} \frac{\partial^2 \xi_z}{\partial z^2} + \left( \frac{\omega^2}{a^2} - k_x^2 \right) \xi_z &= -ik_y \frac{\partial \xi_y}{\partial z}, \\ \left( \frac{\omega^2}{a^2} - k_x^2 - k_y^2 \right) \xi_y &= -ik_y \frac{\partial \xi_z}{\partial z}. \end{aligned} \tag{4.1}$$

It is clear to see that when there is no wavevector component out of the field plane ( $k_y = 0$ ) the two oscillations  $\xi_y$  and  $\xi_z$  (corresponding in this case to the Alfvén and the fast wave respectively) are separated and will not interact. In this case there is a separate fast wave and Alfvén wave solution corresponding to each equation. Energy may not be exchanged between the two wave types when they are in phase at the Alfvén resonance and no fast-Alfvén mode conversion can occur in this case. When  $k_y \neq 0$  the wave solutions will be of a mixed type, with properties either more akin

to an Alfvén or a fast wave depending on the position of the wave. One can easily derive the WKB dispersion relation for the above system,

$$\left(\frac{\omega^2}{a^2} - k^2\right) \left(\frac{\omega^2}{a^2} - k_x^2\right) = 0, \quad (4.2)$$

which corresponds to the system 4.1 with the first term representing the fast wave and the second term the Alfvén wave.

The upwards travelling fast wave will begin to refract as it moves through a monotonic density stratification, until it reaches the classical FWRH. This point is defined as the height at which  $k_z = 0$  for the fast wave, and as such must reflect where  $k_h^2 = \omega^2/a^2$  (in order for equation 4.2 to be satisfied). At this height the fast and Alfvén waves will share the same phase speeds and energy can be channelled between the two wave types. Specifically a portion of the fast wave will tunnel through to undergo resonant absorption at the height where  $\omega = k_{\parallel}a$  (located slightly beyond the classical FWRH) with a remnant of the tunnelled fast wave continuing as an evanescent wave. Only the classical reflection will occur however if  $k_y = 0$ .

### Studies in uniform magnetic fields

Note that in this thesis chapter we make a slight change in notation. We now denote the background field inclination (from the vertical) as  $\theta$  instead of  $\gamma$  to adhere to the notation used in the related literature!

A quantitative study of the effects of fast-to-Alfvén mode conversion in a stratified *warm plasma* atmosphere was first carried out semi-analytically in an inclined uniform field by Cally & Goossens (2008). By driving monochromatic acoustic waves from the boundary of a stratified atmosphere (with an inbuilt acoustic cut-off frequency), the magnetic flux corresponding to the Alfvén wave was measured near the opposing boundary of the atmosphere for a variety of field inclinations ( $\theta$ , where  $0^\circ$  is vertical field) and wavevector plane-to-field plane attack angles ( $\phi$ , where  $\phi = 90^\circ$  implies a perpendicularity between wavevector and field).

A sample of the results of this parameter study are shown in figure 4.1, which is taken from Cally & Goossens (2008); a clear and pronounced maximum in magnetic flux at the top of the box for  $(\theta, \phi) \approx (40^\circ, 60^\circ)$ . The magnetic flux is of course a proxy for the upwards travelling Alfvén wave which has been created at the resonant

atmospheric layer (just above the FWRH). Importantly, it is clear that there is no mode conversion when the field is vertical ( $\theta = 0^\circ$ ) or when the plane containing the wavevector is aligned with the magnetic field plane ( $\phi = 0^\circ$ ). Evidently, when the fast wave begins to move away from the field plane, the mode conversion is enabled.

Cally & Hansen (2011) undertook similar calculations in a *cold plasma* (plasma  $\beta = 0$ ) atmosphere, which is an adequate approximation to the tenuous upper solar atmosphere, where hydrodynamical effects are weak and  $a \gg c$ . The slow wave is frozen out in this approximation, leaving only the Alfvén and the fast magneto-acoustic modes. The authors prescribed a uniform inclined magnetic field of the form  $\mathbf{B} = (B \cos \theta, 0, B \sin \theta)$  in the  $x$ - $z$  plane and an exponential Alfvén speed profile  $a(x)$  in order to set up and solve the equation of motion for the dilatation,

$$\left( \partial_{\parallel}^2 + \frac{\omega^2}{a^2} \right) \boldsymbol{\xi} = -\nabla_p \chi.$$

$\partial_{\parallel}$  indicates a derivative in the direction of the field in the  $x$ - $z$  plane,  $\nabla_p$  is the spatial gradient perpendicular to the field (and in the plane) and  $\chi = \nabla \cdot \boldsymbol{\xi}$ , the dilatation, corresponds to the fast wave. In a cold plasma, the displacement,  $\boldsymbol{\xi}$ , represents contributions from both the Alfvén and the fast wave. However in the above formulation one can see how the fast wave acts like a source term (on the right hand side) to the Alfvén operator (left hand term). The work describes a parameter study in the field orientation variables  $\theta$  and  $\phi$  and also in the normalised wavenumber of the fast wave source,  $\kappa$ , where  $\kappa$  is a scaled horizontal wavenumber ( $\kappa = (\kappa_y^2 + \kappa_z^2)^{1/2}$ , with  $\kappa_y = k_y h = \kappa \sin \phi$  and  $\kappa_z = k_z h = \kappa \cos \phi$  where  $h$  is the scale height in the direction of the inhomogeneity,  $x$  in this case). A time snap-shot of one of the simulations is shown in figure 4.3. Rightwards propagating fast waves are visible as perturbations to  $\chi = \nabla \cdot \boldsymbol{\xi}$  (dark and light green contour shading). Alfvén waves can be seen as perturbations to the ambient field lines, becoming extremely long in wavelength as the local Alfvén speed increases.

Figure 4.2 shows the calculation of the same magnetic flux quantity in the same parameter range of  $\theta$  and  $\phi$  for the cold plasma atmosphere. It can be seen in this case that the conversion continues to be prominent for much lower values of  $\theta$  than seen in the warm plasma. Evidently the ramp effect inhibits the conversion for more vertical field in the warm plasma atmosphere.

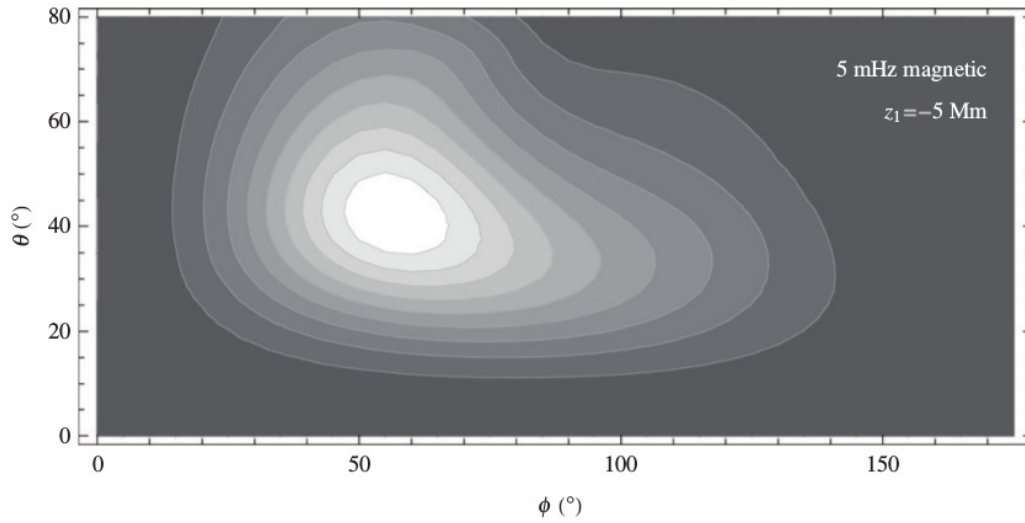


Figure 4.1: Magnetic flux at the right-most boundary of the domain as a function of magnetic field angles  $\theta$  and  $\phi$  for a 5 mHz wave in a 2 kG uniform inclined field *warm plasma* atmosphere. Contours and shading indicate wave energy flux on a linear scale, with white being the greatest flux. The acoustic source is set off at  $z = -5$  Mm corresponding to  $k = 1.37 \text{ Mm}^{-1}$ , or  $\ell \approx 955$  (Cally & Goossens, 2008; Cally & Hansen, 2011).

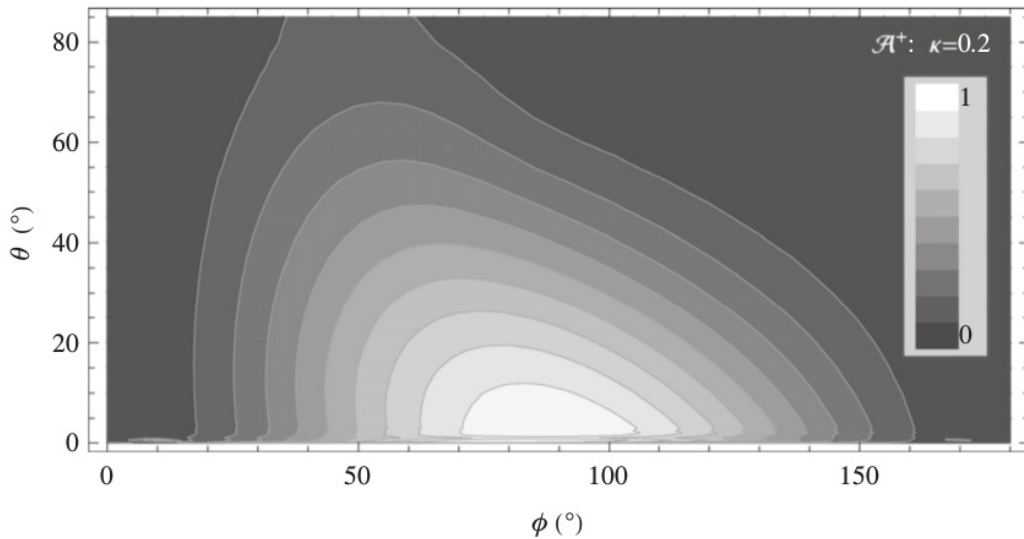


Figure 4.2: Magnetic flux instead from a *cold plasma*. Note that the magnetic flux is 0 at  $\theta = 0^\circ$  (Cally & Hansen, 2011).

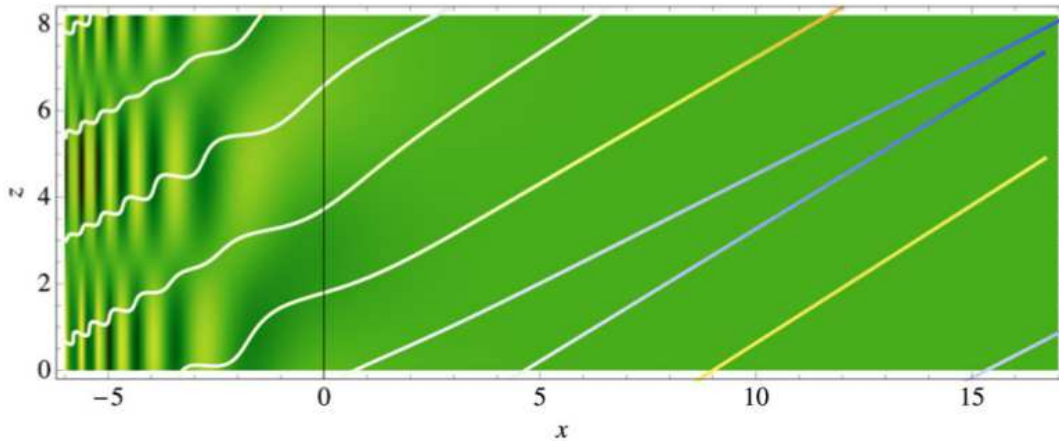


Figure 4.3: snapshot for the case  $\theta = 30^\circ, \phi = 40^\circ$ . The shading is  $\chi = \nabla \cdot \xi$ , the fast wave, which reflects when  $\omega^2 = a^2 k_h^2$  (the vertical black line). Some magnetic field lines are overplotted. In equilibrium they are all inclined at  $\theta = 30^\circ$  but when perturbed they oscillate up and down due to the Alfvén wave. They remain almost straight due to the increasingly long Alfvén wavelength with height in the atmosphere (Cally & Hansen, 2011).

By examining the dispersion curves for the fast, slow and the Alfvén waves in  $k_z$ - $z$  space, Cally & Hansen (2011) were able to determine that much of the upwards-travelling Alfvén wave is reflected before reaching the measurement layer in the warm plasma atmosphere, rather than the conversion itself being less efficient than in the cold plasma case.

The primary result (to which we shall be comparing our own results) from this study is shown as figure 4.4. Contour plots of the *forward* and *reverse* Alfvén coefficients are shown as functions of  $\phi$  and  $\kappa$ , where  $\kappa$  is defined as above. The coefficients denote the fraction of fast wave energy converted to the Alfvén wave in either the field-aligned (forward coefficient) or anti-aligned (reverse coefficient) direction. There is a clear maximum in fast-to-Alfvén conversion efficiency for small values of  $\kappa$ , at  $\phi \approx 90^\circ$  and with a near vertical field. For greater values of  $\theta$  the maximum shifts to more acute attack angles but is decreased in magnitude. Key here also is that the anti-aligned Alfvén wave is generally favoured when  $\phi > 90^\circ$  and conversely, the field aligned Alfvén wave is favoured for angles on the acute side of  $90^\circ$ .

Importantly, Khomenko & Cally (2012) found results to be in close agreement

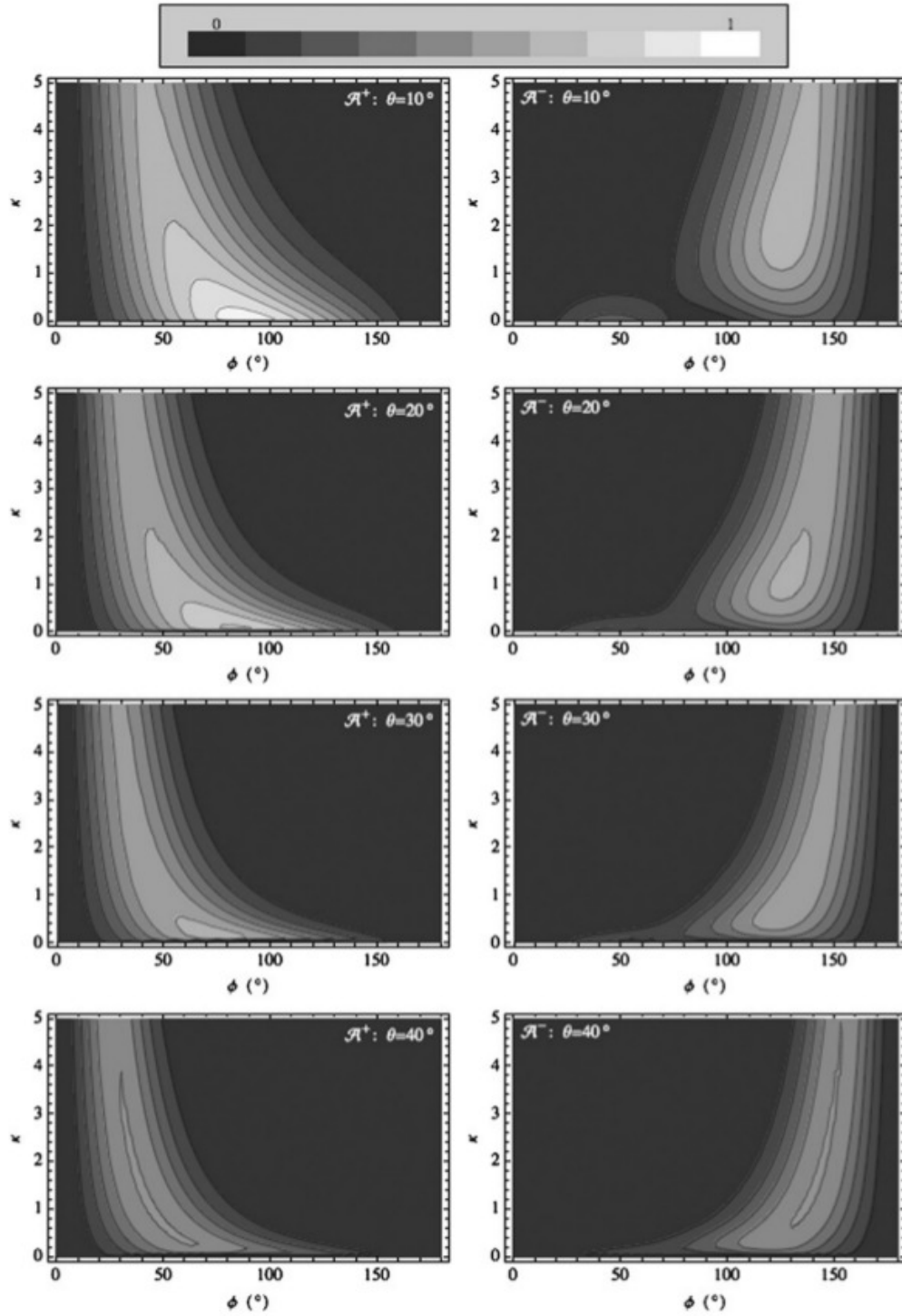


Figure 4.4: Left column: the forward Alfvén conversion coefficient as a function of  $\phi$  and  $\kappa$  for various values of  $\theta$ . Right column: the reverse Alfvén coefficient for the same cases (Cally & Hansen, 2011).

with those above when performing similar simulations using a 2.5D MHS sunspot atmosphere (Khomenko & Collados, 2008) instead of a uniform inclined field. This was later also confirmed in 3D simulations by Felipe (2012). The agreement suggests that the properties of fast-to-Alfvén mode conversion uncovered in the above work are seen in more realistic sunspot-like geometries also and that the orientation of the field and its relationship with the fast wave direction are key drivers of the production of Alfvén waves.

We would like to ascertain whether these basic properties regarding fast-Alfvén conversion efficiency are reproduced in a uniformly twisted magnetic field. Will conversion still be favoured at perpendicularity between  $\mathbf{B}$  and  $\mathbf{k}$ ? Can we expect the directionality of the produced Alfvén waves to be also dependent on the attack angle? What role does the field inclination play in the conversion?

## 4.2 A Twisted Field Atmospheric Model

Sunspot magnetic field has been known to exhibit twist for almost a century (Hale, 1925, 1927), initially having been identified in  $H_\alpha$  filaments. In the pre-spectropolarimetric era, ‘Hale’s rule’ seemed to hold: The direction of azimuthal field twist seemed almost entirely dependent on the hemisphere in which the sunspot was located, although there have been exceptions (Nakagawa et al., 1971). This pattern has also been backed up by helicity analysis studies of potential field (Pevtsov et al., 1994; Abramenko et al., 1996). Recent spectropolarimetric studies however have shown many examples of twist direction which does not follow Hale’s rule (Pevtsov et al., 2005; Tiwari et al., 2009), as well as a variation in the vertical twist direction between photosphere and chromosphere (Socas-Navarro, 2005). Magnetic fields can also be somewhat twisted in the extremely low- $\beta$  environment of the corona, and so it is clear that incorporating an azimuthal variation into any magnetic field structure that we model is a worthwhile pursuit. We now detail our attempts at modelling such a field in a semi-analytic manner.

On top of a twisted magnetic field, we wish to examine fast-to-Alfvén mode conversion in a cold magnetic plasma (as in Cally & Hansen (2011)). Effectively this is a plasma in which  $P_g \ll P_m$  and so we choose  $\beta = P_g/P_m = 0$ . A cold

plasma is a reasonable representation of the upper atmosphere, where the plasma is magnetically dominated. In such an atmosphere the slow magnetoacoustic wave essentially decouples and all oscillations (both the Alfvén and the fast magnetoacoustic waves) are forced such that they are perpendicular to any magnetic field lines ( $\mathbf{B} \cdot \mathbf{v} = 0$ ).

In this section we describe the model that we have used for our atmosphere – the uniform twist force free magnetic field. We will then describe the wave equations that govern our simulations and the various boundary/initial conditions imposed on them as well as performing some preliminary ray path calculations.

### 4.2.1 The uniform twist magnetic field

For our magnetic field, we use the uniform twist force-free field formulation, described in cylindrical coordinates. Each field line rotates the same number of radians per unit height azimuthally. The field is invariant in both the  $z$  and  $\Phi$  directions (where we use  $\Phi$  here to denote the standard cylindrical azimuthal angle) and of course has no radial component.

Mathematically the field vector can be expressed as  $\mathbf{B} = (0, B_\Phi(r), B_z(r))$ , with variations only in the radial direction. Field structure is regularly force-free in a very low- $\beta$  environment and so imposing  $(\mathbf{J} \times \mathbf{B}) \times \mathbf{B} = \mathbf{0}$  on our expression for  $\mathbf{B}$  yields

$$(\mathbf{J} \times \mathbf{B}) \times \mathbf{B} = \left( -B_z \frac{\partial B_z(r)}{\partial r} - \frac{B_\Phi(r)}{r} \frac{\partial}{\partial r} (r B_\Phi(r)) \right) \hat{\mathbf{e}}_r = \mathbf{0},$$

where we have absorbed the magnetic permeability,  $\mu$  (or  $4\pi$  in cgs units) into  $\mathbf{B}$  for convenience. Therefore

$$\begin{aligned} B_z \frac{\partial B_z(r)}{\partial r} + B_\Phi \frac{\partial B_\Phi(r)}{\partial r} + \frac{B_\Phi^2(r)}{r} = \\ \frac{\partial}{\partial r} \left( \frac{B_\Phi^2(r) + B_z^2(r)}{2} \right) + \frac{B_\Phi^2(r)}{r} = 0. \end{aligned}$$

However  $(B_\Phi^2(r) + B_z^2(r))/2$  is simply the magnetic pressure,  $P_m(r) = B^2/2$ , leaving us with

$$\frac{\partial P_m(r)}{\partial r} + \frac{B_\Phi^2(r)}{r} = 0. \tag{4.3}$$

We may simply re-arrange (4.3) to read off our constraints on the field components:

$$B_\Phi = \sqrt{-rP'_m(r)}, \quad (4.4)$$

$$B_z^2 = 2P_m(r) - B_\Phi^2, \quad (4.5)$$

where  $P'_m(r) = \partial P_m(r)/\partial r$ . We are free therefore to choose any radial magnetic pressure distribution  $P_m(r)$  provided that  $P'_m(r) > 0$  for  $r > 0$ .

We choose the following pressure distribution:

$$P_m(r) = \frac{B_0^2}{2 + 8\pi^2 r^2/L^2} \quad (4.6)$$

which describes the uniform twist field which twists through  $2\pi$  radians over a height change  $L$ .  $B_0$  is a constant which determines the Alfvén speed at the centre base of the cylindrical domain. The severity of the field twist is controlled by the parameter  $L$ , with field becoming untwisted and purely vertical in the limit as  $L \rightarrow \infty$ . Conversely a small value of  $L$  indicates a full rotation of the field lines in only a small height change (severe twist). With this choice of  $P_m(r)$  the field components are determined by equations (4.4) and (4.5).

For reasons of numerical simplicity, we have chosen the radial domain of our simulations to exclude  $r = 0$  (discussed later) and to solve the equations of motion some distance away from this centre point. The field itself is purely vertical at the axis anyway and so is of no interest to us. Thus all further discussion takes place in the arbitrary dimensionless radial range  $6 \leq r \leq 30$ . For the parameter study we look at 4 different twist cases corresponding to purely vertical field ( $L \rightarrow \infty$ ), a slightly twisted field ( $L = 4000$ ), moderate twist ( $L = 700$ ) and a strongly twisted field ( $L = 300$ ). The resultant radial profiles for the field inclination,  $\theta$  and the field strength,  $|\mathbf{B}|$  are shown in figures 4.5 and 4.6 for the 4 different twist cases.

With the parameters chosen above, one can see how the field quantities vary radially. The angle ranges in brackets on the plots denote the ranges over which the field inclination increases for the different twist cases for  $B_0 = 1$  in equation (4.6). There is not a great deal of variation in either the field strength or inclination over the range  $6 \leq r \leq 30$  when  $L = 4000$  for instance, whereas we get inclinations up to and above  $30^\circ$  from the vertical in the most twisted ( $L = 300$ ) case. The field

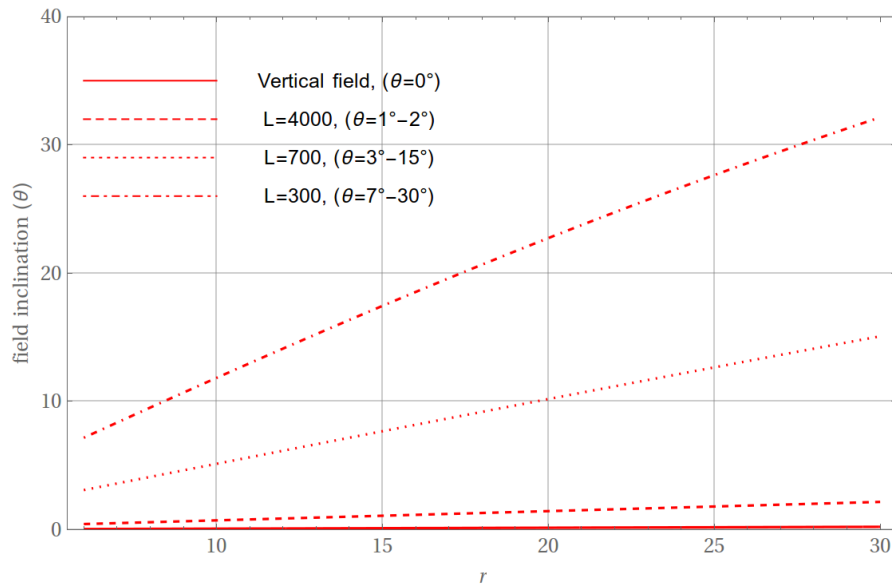


Figure 4.5: Radial profiles of  $\theta$  for 4 different twist cases: Untwisted vertical field (solid red,  $L \rightarrow \infty$ ), Slightly twisted (dashed red,  $L = 4000$ ), moderately twisted (dotted red,  $L = 700$ ) and strongly twisted (dash-dotted red,  $L = 300$ ). All field structure is invariant with height.

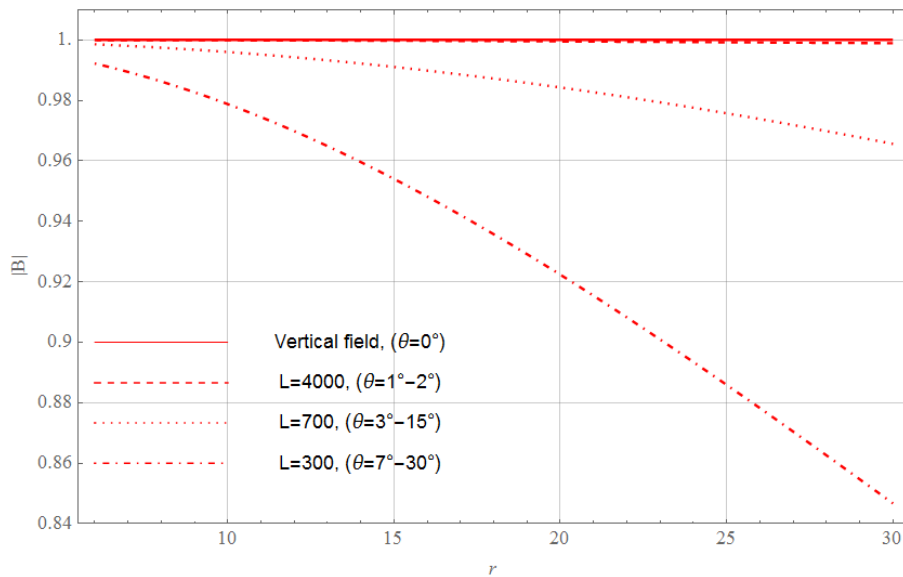


Figure 4.6: Radial profiles of  $|\mathbf{B}|$  for the same 4 twist cases. The value of  $|\mathbf{B}|$  is scaled to the dimensionless value of 1 at  $r = 0$  by choosing  $B_0 = 1$ .

strength on the other hand decays very little even in the  $L = 300$  field, with only a maximum 10 – 15% decrease over our radial domain. This is not so much an issue as we are primarily interested in the variation of the Alfvén speed and the relationship between  $\mathbf{k}$ ,  $\theta$  and  $\phi$ , with  $|\mathbf{B}|$  playing a less important role in the mode conversion process.

### 4.2.2 Density stratification and Alfvén speed

Because the plasma is assumed cold, the gas pressure is zero irrespective of density. The density  $\rho$  may therefore be chosen arbitrarily, with an effect only on the Alfvén speed. It is appropriate to introduce a density that decreases roughly exponentially before tailing off to a constant value at the top of the simulation domain. As such we introduce a density profile of the form

$$\rho(z) = A \tanh(z/h) + C, \quad (4.7)$$

with suitable choices for the parameters  $A$ ,  $h$  and  $C$ . This density stratification decreases in an exponential manner which in turn leads to an exponentially increasing Alfvén speed profile (as  $a \propto |\mathbf{B}|/\sqrt{\rho(z)}$ ) which tails off to a roughly constant value

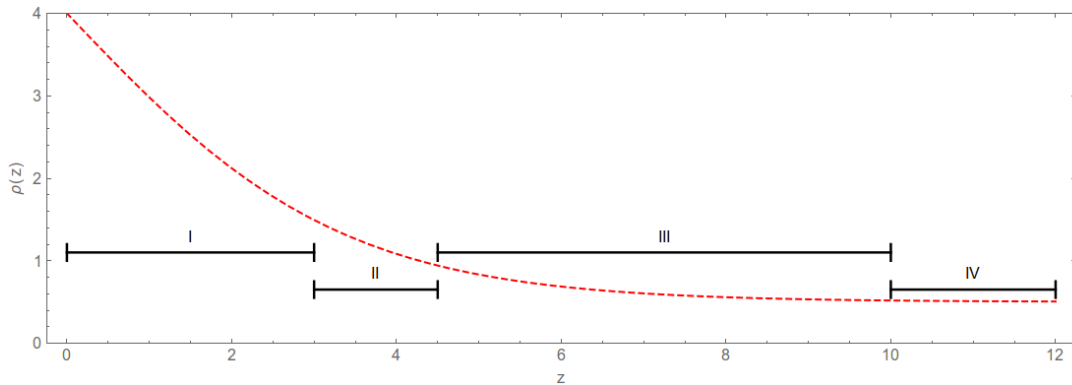


Figure 4.7:  $\rho(z)$  from bottom to top of the  $z$  domain with  $A = -3.5$ ,  $h = 3.3$  and  $C = 4$ . Each of the approximate regions I-IV are distinct in terms of wave behaviour (assuming a  $B_0 = 1$  low-twist atmosphere). Region I:  $a < \omega/k_h$  and fast waves are refracting (still upwards travelling), II: The classical FWRH where  $a \approx \omega/k_h$ , III: The resonance layer where we expect fast-Alfvén conversion to occur ( $a > \omega/k_h$ ), IV: Isothermal top where we will attempt to quantify the mode conversion.

at the top of the simulation domain. The isothermal region at the top is required for the upper boundary condition (described later). The rapid rise of the Alfvén speed profile effectively models the top of the photosphere and chromosphere where the dynamics swiftly become magnetically dominated.

It is our intention to drive fast waves with angular frequency  $\omega$  and horizontal wavenumber  $k_h$  from the bottom boundary of the annular cylindrical domain, where  $k_h$  is the horizontal component of the wavenumber,  $k$ , which is defined in cylindrical coordinates as,

$$k_h^2 = k_r^2 + k_\Phi^2 = k_r^2 + m^2/r^2,$$

where  $m$  is the azimuthal wavenumber. With the above density profile, appropriate values of  $\omega$  and  $k_h$  for the driven fast waves and the field scaling parameter  $B_0 = 1$  (from equation 4.6), we can expect the following situation, shown schematically in figure 4.7: Driven fast waves will rise while refracting in region I. The waves will undergo classical reflection somewhere around region II, where the horizontal phase speed equals the Alfvén speed. A certain amount of fast wave energy will tunnel into region III and mode conversion will take place here, manifesting itself as an enhancement in Alfvén flux. As mentioned previously, above this point the fast wave is still present but exhibits an exponentially decreasing magnitude of order  $\exp(-kz)$  (Cally, 2011). In reality, the thickness of this region can extend many atmospheric scale heights and for typical helioseismic waves may extend over the majority of the chromosphere (Cally & Hansen, 2011). However we are only interested in ensuring that there is enough room (vertically) in our simulation domain for some form of resonance to take effect. We then ideally wish to measure the effect in the isothermal heights well above the FWRH. We are not attempting to model the thickness of the resonance layer. Region IV is the isothermal area where we will perform measurements of the Alfvén wave in order to quantify the mode conversion.

Unlike  $\rho(z)$ ,  $a$  is a function of  $r$  and  $z$  and its profile is very much altered by the field twist. Figure 4.8 shows the profile of  $a(r, z)$  for the 3 twisted field cases  $L = 4000, 700$  and  $300$ . In the  $L = 4000$  case, it is clear that the Alfvén speed profile is almost unchanging in  $r$ , as we have a situation not too dissimilar from an untwisted vertical field where  $a = a(z)$ . The dashed contours (contours of constant  $a$ ) begin to take a more irregular shape as the twist increases; there will be a radial

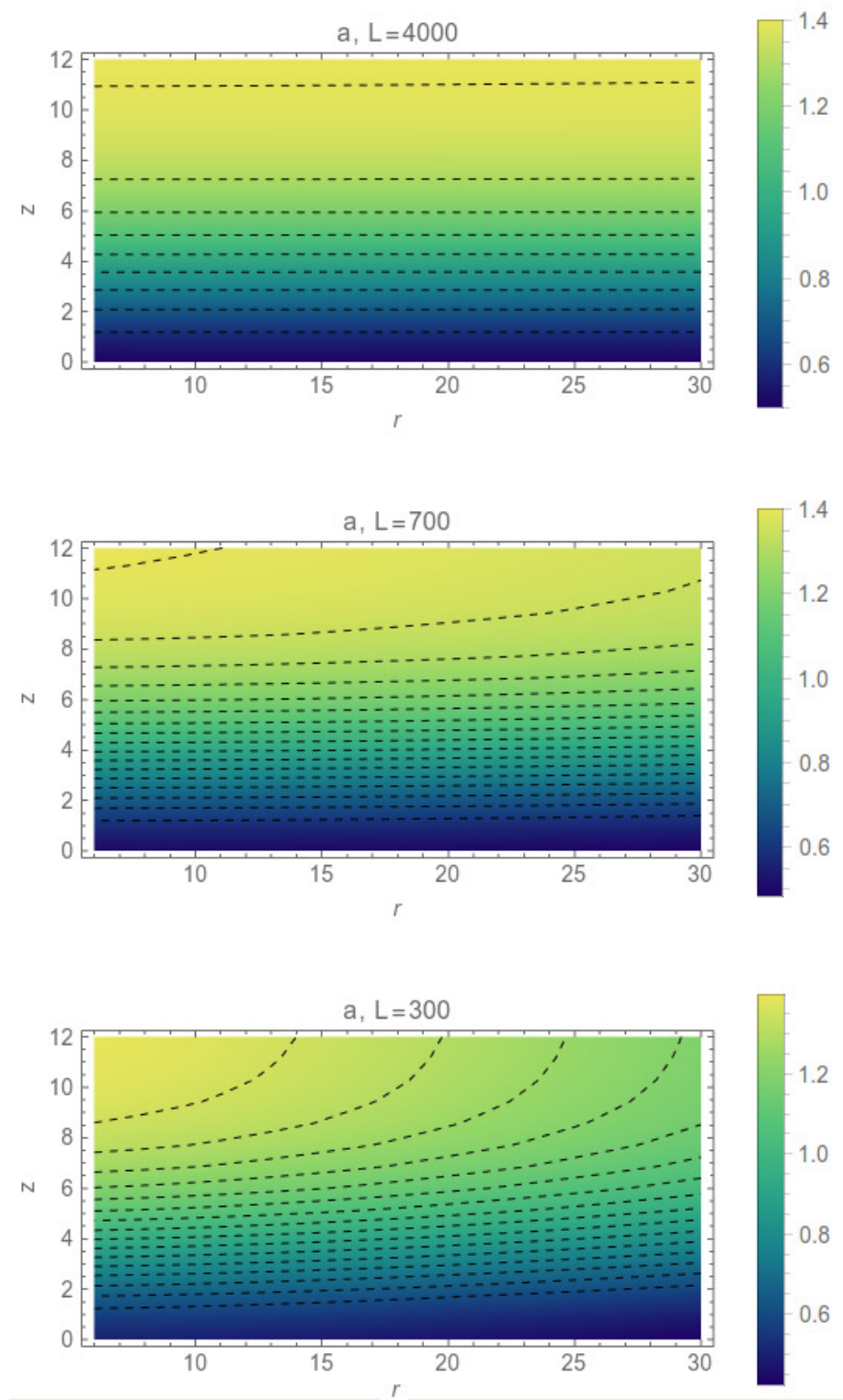


Figure 4.8: Density plots of the Alfvén speed profiles for the 3 differently twisted atmospheres corresponding to the parameters  $L = 4000, 700$  and  $300$  for  $B_0 = 1$ . Dashed contours are contours of constant  $a$ .

difference in the wave speed for the upwards travelling fast and Alfvén waves in these cases.

### 4.2.3 Solving the equations of motion

Our first step is to initiate a wave driver at the bottom of the atmosphere. In order to accomplish this we define a vector displacement  $\boldsymbol{\xi}(r, z, \Phi, t) = \boldsymbol{\xi}(r, z, t)e^{im\Phi}$  in cylindrical coordinates, where we have taken out the intrinsic  $\Phi$  dependence. The vector  $\boldsymbol{\xi}$  has 3 orthogonal components corresponding to the Frenet-Serret coordinate system; one component in the inward radial direction ( $\xi_r$ ), one component tangent to the magnetic field ( $\xi_f$ ) and the third perpendicular to the field, but aligned with the cylinder ( $\xi_\perp$ ).

Things are simplified considerably however as any displacements are necessarily perpendicular to the field lines in a  $\beta = 0$  plasma. We are free therefore to express the displacement in terms of just 2 linearly independent components,  $\eta(r, z, t)$  (the radial component,  $\xi_r$ ) and  $\zeta(r, z, t)$  (the perpendicular to field but in-cylinder component,  $\xi_\perp$ ). The component  $\xi_f$  tangent to the field will simply be equal to 0 due to the cold plasma assumption. The unit vector perpendicular to  $\mathbf{B} = (0, B_\Phi, B_z)$  (where  $\mathbf{B}$  is the uniform twist field) is simply  $\hat{\mathbf{B}}_\perp = \frac{1}{|\mathbf{B}|}(0, -B_z, B_\Phi) = (0, -\hat{B}_z, \hat{B}_\Phi)$ . We therefore express the vector displacement as

$$\boldsymbol{\xi} = e^{im\Phi}(\eta(r, z, t), 0, 0) + \zeta(r, z, t)\hat{\mathbf{B}}_\perp = e^{im\Phi}(\eta(r, z, t), \zeta(r, z, t)\hat{B}_z, \zeta(r, z, t)\hat{B}_\Phi),$$

and we need only solve for the two displacement components  $\eta$  and  $\zeta$  in cylindrical coordinates  $r, z$  and  $t$  for a given choice of  $\Phi$ .

With the choice of background field, density stratification and displacement formulation made we then need only solve the necessary equations of motion for the displacements. In this case the linearised wave momentum equation is simply expressed as

$$\rho(z)\frac{\partial^2 \boldsymbol{\xi}}{\partial t^2} = (\mathbf{J}_0 \times \mathbf{B}_1) + (\mathbf{J}_1 \times \mathbf{B}_0), \quad (4.8)$$

where as usual  $\mathbf{J} = \nabla \times \mathbf{B}$  is the current density and the subscripts refer to background quantities or linear perturbations to those background quantities ('0' and '1' respectively). As the field is force free there is no pressure gradient against which

the Lorentz force must be balanced, therefore the Lorentz force is the only force term on the right hand side of the momentum equation. The gravitational stratification makes itself known only through the density profile  $\rho(z)$ .

We solve for the two linearly independent components of the displacement using a standard explicit forward differences scheme with a method of lines numerical approach implemented in Mathematica (Ascher & Petzold, 1998).

#### 4.2.4 Geometry and boundary/initial conditions

The two equations for  $\eta(r, z, t)$  and  $\zeta(r, z, t)$  corresponding to equation (4.8) are solved in a slice of a cylindrical domain. As mentioned earlier we choose not to include the centre of the cylinder at  $r = 0$  due to the fact that there are singularities in the differential equation at this point. As such our domain is chosen to be some cylindrical region  $R_1 < r < R_2$  with  $R_1 > 0$  and  $0 < z < Z_{top}$  (the size of which we will discuss shortly). The initial conditions on the displacement variables are zero everywhere:

$$\begin{aligned}\eta(r, z, 0) &= \zeta(r, z, 0) = 0, \\ \frac{\partial}{\partial t}\eta(r, z, 0) &= \frac{\partial}{\partial t}\zeta(r, z, 0) = 0.\end{aligned}$$

Boundary conditions are prescribed on the radial boundaries for  $\eta$  as

$$\eta(R_1, z, t) = \eta(R_2, z, t) = 0,$$

while the boundary conditions for  $\zeta$  are specified at the top and bottom of the box, at  $z = 0$  and  $z = Z_{top}$ .

##### **A wave driving boundary condition at the bottom.**

The  $\zeta$  bottom boundary condition is the periodic wave driver, which will drive oscillations corresponding to both the Alfvén and the fast modes up and into the atmosphere. We have implemented this driver as a simple spatio-temporal sinusoid:

$$\zeta(r, 0, t) = \tanh(100t) \sin(k_r[r - \alpha]) \sin(\omega t), \quad (4.9)$$

where  $\omega$  is the standard angular frequency,  $k_r$  is the radial component of the wavenumber and  $\alpha$  the spatial shift if required (depending on  $R_1$  and  $R_2$ ). The  $\tanh(100t)$

term simply enforces compliance with the  $\frac{\partial}{\partial t}\zeta(r, z, 0) = 0$  initial condition but in all other regards has no effect on the source, rising quickly to a constant value of unity.

With this prescription we have control over all parameters of the wave source and can drive monochromatic sinusoidal waves of any spatial or temporal profile.

### **An absorbing boundary at the top.**

At the top boundary, we prescribe an absorbing boundary condition which relies on two assumptions:

1. The wave speed along field lines becomes constant at the top of the box. This is the reason that we have chosen the particular density profile described by equation 4.7.

2. Any wave at the top of the box is almost certainly an Alfvén wave, as the fast waves have returned back downwards at the fast wave reflection height, leaving only an evanescent tail which will decay exponentially.

Under these conditions, the wave equation describing Alfvén waves travelling along field lines is simply

$$\frac{\partial^2 \xi_*}{\partial t^2} = a^2 \frac{\partial^2 \xi_*}{\partial s^2},$$

where  $a$  is the constant Alfvén speed,  $s$  is the arc-length along field lines and  $\xi_*$  is the Alfvén wave displacement (with no fast wave contribution). As  $a$  is constant, we can therefore decompose the above expression as

$$\left(\frac{\partial}{\partial t} - a \frac{\partial}{\partial s}\right) \left(\frac{\partial}{\partial t} + a \frac{\partial}{\partial s}\right) \xi_* = 0,$$

which we can split into the two equations

$$\begin{aligned} \left(\frac{\partial}{\partial t} - a \frac{\partial}{\partial s}\right) \xi_*^\downarrow &= 0, \\ \left(\frac{\partial}{\partial t} + a \frac{\partial}{\partial s}\right) \xi_*^\uparrow &= 0. \end{aligned}$$

$\xi_*^\downarrow = \xi_*^\downarrow(s + at)$  is the downwards-travelling Alfvén wave and  $\xi_*^\uparrow = \xi_*^\uparrow(s - at)$  the upwards-travelling wave. In order to ensure no downwards-travelling reflected waves from the top we simply set

$$\frac{\partial \xi_*}{\partial t} + a \frac{\partial \xi_*}{\partial s} = 0$$

as the top boundary condition at  $z = Z_{top}$ . Therefore if  $\xi_* = \xi_*^\uparrow + \xi_*^\downarrow$  then

$$\left(\frac{\partial \xi_*^\uparrow}{\partial t} + a \frac{\partial \xi_*^\uparrow}{\partial s}\right) + \left(\frac{\partial \xi_*^\downarrow}{\partial t} + a \frac{\partial \xi_*^\downarrow}{\partial s}\right) = 0,$$

where the first term is 0 automatically and the second term enforces  $\xi_*^\downarrow = 0$ , which cuts off any reflecting Alfvén waves.

### 4.2.5 Preliminary ray-path calculations

The plane-cylindrical domain must be of sufficient size to allow fast waves to refract and reflect. As a check we therefore perform some initial ray-path calculations based on our wave and field parameters to map the approximate paths that the waves will take when driven from the bottom boundary. This is important as we require the fast waves to fully turn over in order to interact with the Alfvén resonance.

In order to do this we make use of the Hamiltonian ray path formulation which describes the evolution of the position,  $\mathbf{r}$ , and the wavevector,  $\mathbf{k}$ , in terms of the fast wave dispersion relation,  $\mathcal{D}$  (Barnes & Cally, 2001; Schunker & Cally, 2006).

For fast waves  $\mathcal{D} = \omega^2 - a^2(k_r^2 + k_\Phi^2 + k_z^2)$  when expressed in terms of the 3 components of the wavevector in cylindrical coordinates. The Hamiltonian differential relations are expressed as

$$\frac{d\mathbf{r}}{d\tau} = \frac{\partial \mathcal{D}}{\partial \mathbf{k}}, \quad \frac{d\mathbf{k}}{d\tau} = -\frac{\partial \mathcal{D}}{\partial \mathbf{x}}, \quad \frac{dt}{d\tau} = -\frac{\partial \mathcal{D}}{\partial \omega} = -2\omega \quad (4.10)$$

where  $\tau$  is simply a frequency-scaled time-like variable. We solve the first two terms of (4.10) as a system of six differential equations for the vector positions  $\mathbf{r} = (r, \Phi, z)$  and wavenumbers  $\mathbf{k} = (k_r, k_\Phi, k_z)$  given the initial  $\mathbf{k}$  and  $\mathbf{r}$  which we plan to use when initiating the full simulation.

As shown in figures in previous sections we choose a domain  $6 \leq r \leq 30$  and  $0 \leq z \leq 12$  in arbitrary normalised units, where the radial domain is shifted away from the  $r = 0$  axis for numerical reasons. For the wave driver given by equation (4.9) (and for the Hamiltonian system above) we choose values for  $k_r$  and  $\omega$  which allow for a reasonable fast wave turnover height. There are severe constraints on the combination of field parameters ( $B_0$  and  $L$ ) and wave parameters ( $\omega$ ,  $k_r$  and  $m$ ) which we can use together and still obtain useful results. Changing any of the above parameters alters the FWRH and structure of the atmosphere. We must reach a

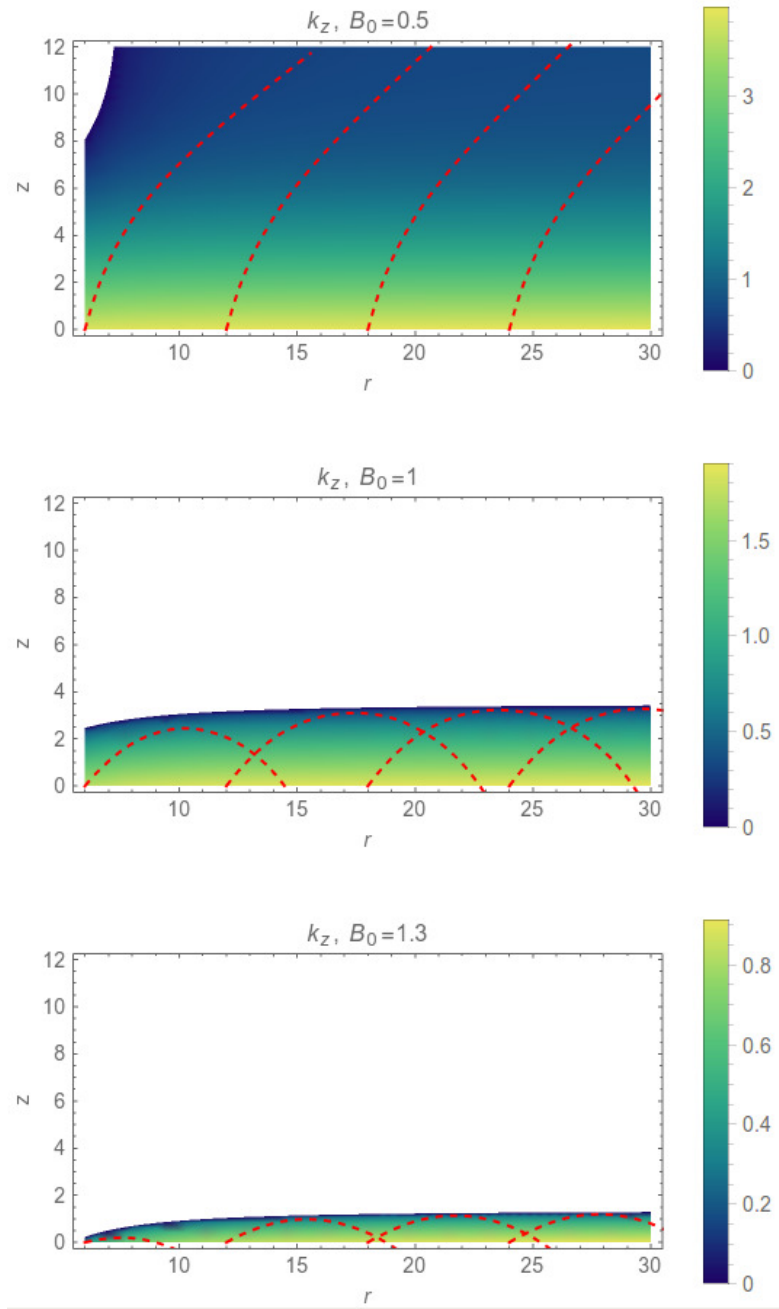


Figure 4.9: Green-blue coloured background density plots indicate the value of  $k_z$  of upwards travelling fast waves. The fast wave cannot classically enter the white regions as it has already reflected. Red dashed curves are the fast wave ray paths launched from various positions at  $z = 0$ . The three panels correspond to the 3 cases  $B_0 = 0.5, 1$  and  $1.3$ .

compromise which provides room for fast waves to reflect while giving us ample room above that for the fast-Alfvén mode conversion process to take effect and for us to be able to measure that effect.

Figure 4.9 shows the results of the solution of the system of equations (4.10) with an appropriate choice of  $\omega$  and  $k_h$ , for  $L = 4000$ ,  $m = 5$  and for  $B_0 = 0.5, 1$  and  $1.3$ . The background contour is the value of  $k_z$  for the driven wave. Given the fast wave dispersion relation  $k^2 = k_r^2 + k_\Phi^2 + k_z^2 = \omega^2/a^2$ ,  $k_z$  can easily be calculated at all points in a given atmosphere, as  $a(r, z)$ ,  $\omega$ ,  $k_r$  and  $k_\Phi = m/r$  are all prescribed. The dashed red contours are the paths of rays launched from the positions  $(r, z) = (6, 0), (12, 0), (18, 0)$  and  $(24, 0)$  and show the evolution of  $k_r$  and  $k_z$  for the rays with respect to the time-like variable  $\tau$ . The point at which  $k_z = 0$  is the classical FWRH and we can see that the solution of the Hamiltonian equations for the ray paths agrees with this  $k_z = 0$  height found from the dispersion relation. Importantly the combination of the geometry, field and wave parameters chosen provides sufficient room for most of the fast waves to turn over in the  $B_0 = 1$  atmosphere (middle panel). The effect of changing the  $B_0$  value is also evident. In the  $B_0 = 0.5$  atmosphere we expect no mode conversion to occur, as the FWRH is somewhere well above the top of the box - the fast waves will never reflect. Conversely by increasing  $B_0$  the fast waves will turn over increasingly quickly which should lead a mode conversion effect being observable more rapidly.

## 4.3 Simulation Results

In this section we elaborate on the plan for our parameter study, detailing what we hope to achieve, presenting our results and then discussing our conclusions.

### 4.3.1 The parameter study and its goal

Our tasks will be as follows:

1. To ensure that the lower-boundary driven fast waves are turning over correctly at the FWRH.

2. To quantify the fast-Alfvén mode conversion and ensure that it is actually taking place as we would theoretically expect.
  
3. To examine the effectiveness of the fast-Alfvén conversion process as a function of field inclination ( $\theta$ ) and wave-to-field attack angle ( $\phi$ ). We will then compare our findings for the twisted field to those found in Cally & Hansen (2011) for a uniform inclined field, while hopefully being able to make some statements about the generation of Alfvén waves at chromospheric heights amongst twisted field.

In order to perform these tests we undertake a parameter study with respect to the aforementioned field orientation parameters  $\theta$  and  $\phi$ . The goal here is to measure the effectiveness of the fast-Alfvén mode conversion with the variation of these parameters.

Table 4.3.1 describes the variation of the relevant parameters and lists some of the effects that these parameter changes have on the atmosphere. For each combination of parameters we perform a separate simulation with the same wave driving source function. We keep the values for  $\omega$  and  $k_h$  constant throughout this study.

The first row of the table shows the various values of the parameter  $L$ , describing the field twist, with the field approaching an untwisted vertical field as  $L \rightarrow \infty$ . The case  $L = \infty$  in the table simply corresponds to a plain vertical field. In this case, as already mentioned, no fast-Alfvén mode conversion can take place. Successively lower values of the parameter result in a greater twist, such that the field twists through an azimuthal angle of  $2\pi$  radians over a shorter height range. The second row shows the field inclination range as a function of  $r$  as described in figure 4.5.

Atmospheric and field parameters												
Field twist parameter $L$ :	300			700			4000			$\infty$		
Field $\theta$ range (radially):	7°-30°			3°-15°			1°-2°			0°		
Central base Alfvén speed $B_0$ :	0.5	1	1.3	0.5	1	1.3	0.5	1	1.3	0.5	1	1.3
Classical reflection?	No	Yes		No	Yes		No	Yes		No	Yes	
Mode conversion?	No	Yes		No	Yes		No	Yes		No		

Table 4.1: A range of atmospheric and field twist parameters

The third row shows the value of  $B_0$  applied to the atmosphere, while the last two rows tell us whether we expect classical fast wave reflection and/or mode conversion with the chosen parameters.

As can be seen in figure 4.9, for  $a_0 = 0.5$  (the weak field case), the FWRH is beyond the top of the simulation domain; neither fast wave reflection nor fast-Alfvén mode conversion can occur in such a simulation regardless of the field twist. In the vertical field case for  $a = 1$  and  $1.3$  (moderate and strong field cases respectively) we expect to see fast wave reflection but no mode conversion and for all other cases for  $a = 1$  and  $a = 1.3$  the layer is present, at different heights in the  $r, z$  domain and we would expect to see some sign of the conversion. Even though mode conversion is not present, the  $a = 0.5$  and vertical field cases serve as very useful comparison atmospheres. When we measure the presence of the Alfvén oscillation above the FWRH we can compare with these atmospheres to quantify the conversion.

#### Deriving some useful physical quantities

As already thoroughly explained, our simulation outputs are  $\eta(r, z, t)$  and  $\zeta(r, z, t)$ , the radial and perpendicular-to-field (but in-cylinder) components of the vector displacement,  $\boldsymbol{\xi}(r, z, t)$ . Unfortunately the fast and the Alfvén perturbations are entwined together and an analytical method of disentangling the two wave types prior to solution of the wave equations is not known to us (see Cally & Andries (2010) and Cally & Hansen (2011) for instance for some discussion on this matter). Instead we calculate proxies for the fast and Alfvén waves after solving equation 4.8 for the displacements. In quantifying the fast wave, we calculate  $\chi(r, z, t) = \nabla \cdot \boldsymbol{\xi}$ . Any non-zero dilatation  $\chi$  must be related solely to the fast wave as the incompressive, field-orthogonal Alfvén wave must satisfy  $\nabla \cdot \boldsymbol{\xi} = 0$  for all  $(r, z, t)$ .

We can track the Alfvén wave in two ways. The first way is by calculating  $\psi(r, z, t) = \hat{\mathbf{B}} \cdot (\nabla \times \boldsymbol{\xi})$ , which is simply the component of the rotation of the displacement in the direction of the background field. We can also track the Alfvén wave by the electro-magnetic energy being transported by it, i.e. by calculating the Poynting vector (as in chapter 3),  $\mathbf{S} = \mathbf{B}_1 \times (-\mathbf{v} \times \mathbf{B})$ , where  $\mathbf{v} = \partial \boldsymbol{\xi} / \partial t$  and  $\mathbf{B}_1$  is the perturbation to the equilibrium background field,  $\mathbf{B}$ . We can assume that the Alfvén wave is solely responsible for any Poynting flux at heights well above the

FWRH and so this serves as perhaps the best tool to infer the presence of the Alfvén oscillation.

### 4.3.2 Examining the fast wave

Above the FWRH we expect to observe an exponential decrease in the magnitude of the fast wave. The majority of the fast wave reflects as  $k_z^2$  changes sign, however a portion of the wave energy is channeled into the field-aligned Alfvén mode. Thus the fast wave has an evanescent structure above this height. This fast wave decay should be observable by tracking the magnitude of  $\chi$  as it progresses upwards through the atmosphere. The true Alfvén wave cannot contribute to  $\chi$  as it must satisfy  $\nabla \cdot \xi = 0$  at all times. However, in the mode conversion region, a hybrid fast/Alfvén wave is to be expected.

We choose a near-vertical slightly twisted ( $L = 4000$ ) field and measure the magnitude of the leading wavefront of  $\chi$  at 4 different heights ( $z = 1, 3, 6$  and  $10$ ) through the 3 different atmospheres corresponding to  $B_0 = 0.5, 1$  and  $1.3$ . We have driven oscillations at the lower boundary until several wave-fronts have travelled all the way to the top of the box at  $z = 12$  and essentially averaged over a small height range around the different  $z$  values corresponding to the vertical extent of the leading wavefront for a small duration as the wave passes. These measurements are shown in figure 4.10. The values have been normalised to the peak value of  $\chi$  at  $z = 10$  for simplicity of analysis in each case. One can see where the four sample heights ( $z = 1, 3, 6$  and  $10$ ) lie with respect to the FWRH by examining figure 4.9. In the weak field case ( $B_0 = 0.5$ ), all sample heights lie in the  $a < \omega/k_h$  region, whereas in the moderate and strong field cases our upper sampling heights are above the FWRH and hence in the zone where vertically propagating fast waves are prohibited (evanescent decay).

As can be seen in the top panel of figure 4.10, we observe only a small decay in the magnitude of  $\chi$  for the weak field atmosphere, which makes sense as the fast wave never reaches the FWRH and simply propagates upwards, slowly turning over but never reaching horizontality. In the moderate field ( $B_0 = 1$ ) case the FWRH sits at about  $z = 3-4$  (as can be seen in figure 4.9). We see a steep drop off in  $\chi$

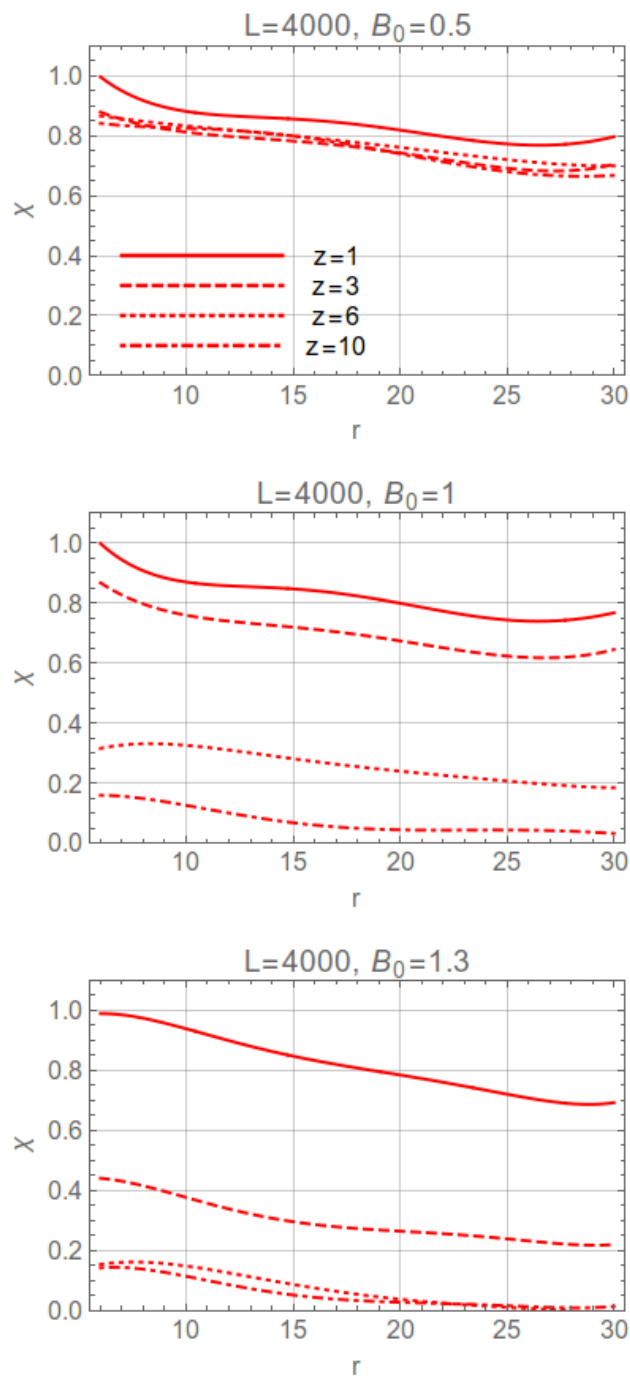


Figure 4.10: Normalized values for  $\chi = \nabla \cdot \xi$ , which we use as a proxy for the fast wave. Each curve is a measure of the leading wave front of  $\chi$  taken at increasing heights for an  $m = 0$  wave in the  $L = 4000$  (near-vertical) field. In essence we are following the amplitude of the fast wave as it travels upwards.

above these heights which corresponds to the fast wave turn-over and decay. The  $B_0 = 1.3$  atmosphere FWRH sits nearer the bottom of the domain and so the decay is steeper and occurs earlier as fast waves have turned over soon after their creation at  $z = 0$ . We conclude that the fast waves are behaving as expected. As predicted by our ray path analysis, they appear to decay above the classical FWRH.

### 4.3.3 Alfvén wave production

Our next task is to attempt to quantify the mode conversion effect itself - the production of Alfvén waves in the resonant layer above the FWRH. In a similar manner to how we analysed  $\chi(r, z, t)$ , we calculate the field-aligned rotational velocity component  $\psi(r, z, t) = \hat{\mathbf{B}} \cdot (\nabla \times \boldsymbol{\xi})$ , which is indicative of the transverse and incompressible Alfvén wave. We analyse this quantity for a series of heights, and as a function of  $L$  and  $B_0$ .

As the fast wave reaches the resonance layer and turns over, we expect to see some enhancement in  $\psi$  in the layers above the FWRH as Alfvén energy is created. We are *not* attempting to quantify the thickness of the resonance layer, which can extend many scale heights, and is dependant primarily on the wavenumber,  $k$  (Cally, 2011). All we wish to do is instead observe some increase in a quantity which is related to the Alfvén wave. As the wave driver does initially contain some mix of both the fast and the Alfvén oscillations, there is a quantity of  $\psi$  present before fast wave turnover corresponding to these driven Alfvén waves. However we are interested in the *change* in the quantity above the resonance height.

Figures 4.11 and 4.12 show the measurements of  $\psi$  at the top of the box as a function of  $L$  and  $B_0$ . Each panel of both of the figures corresponds to a different field twist parameter in that atmosphere. To re-iterate for clarity, we expect *no* mode conversion in the weak-field case of figure 4.11 (regardless of the field twist) or in any purely vertical field (regardless of  $B_0$ ).

There are several important conclusions to draw from these results. Firstly, as expected in figure 4.11 there does not seem to be any consistent, noticeable relationship between  $\psi$  and height for any level of field twist. In panel c there is roughly a 20% change in  $\psi$  but it is not a monotonic change with height. The lack of increase

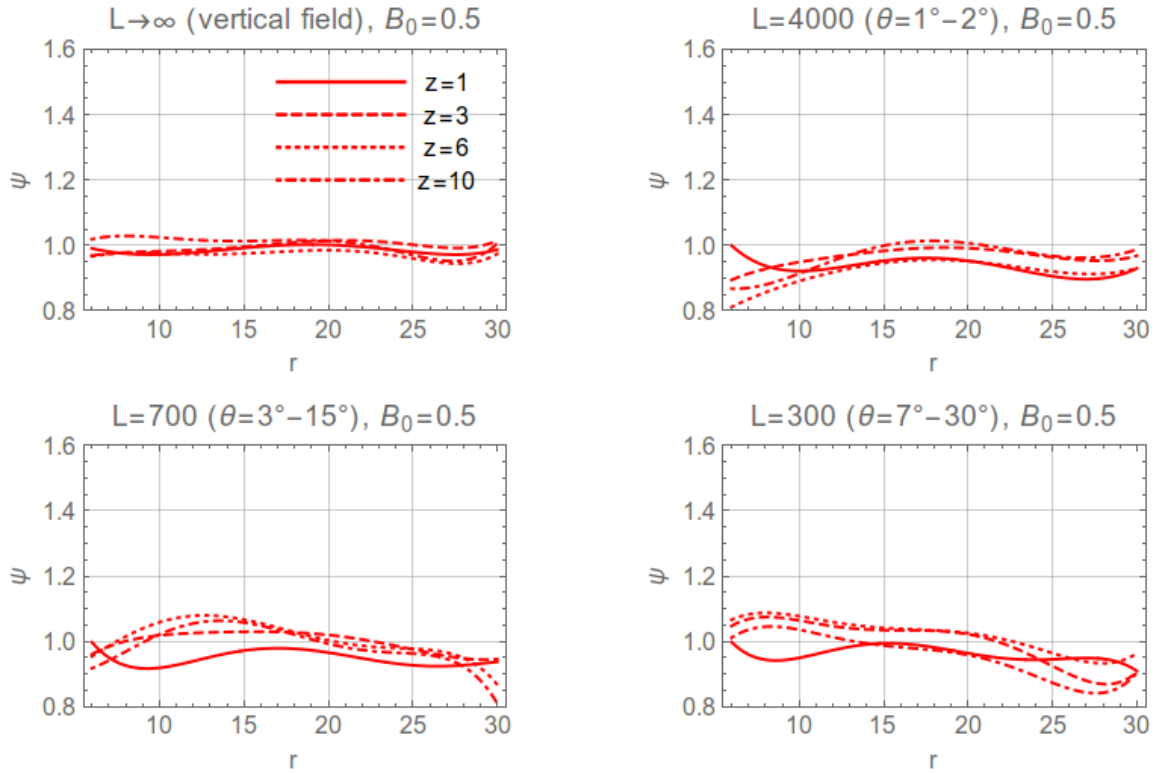


Figure 4.11: Normalized values for  $\psi(r, z, t) = \hat{\mathbf{B}} \cdot (\nabla \times \boldsymbol{\xi})$ , which we use as a proxy for the Alfvén wave. Each curve is a measure of the leading wave front of  $\psi$  taken at increasing heights. We are tracking the amplitude of the Alfvén wave as it travels upwards. Field is purely vertical in the top-left panel and becomes increasingly twisted in the other panels. Curves are roughly normalised to the average value of  $\psi$  at  $z = 1$ .

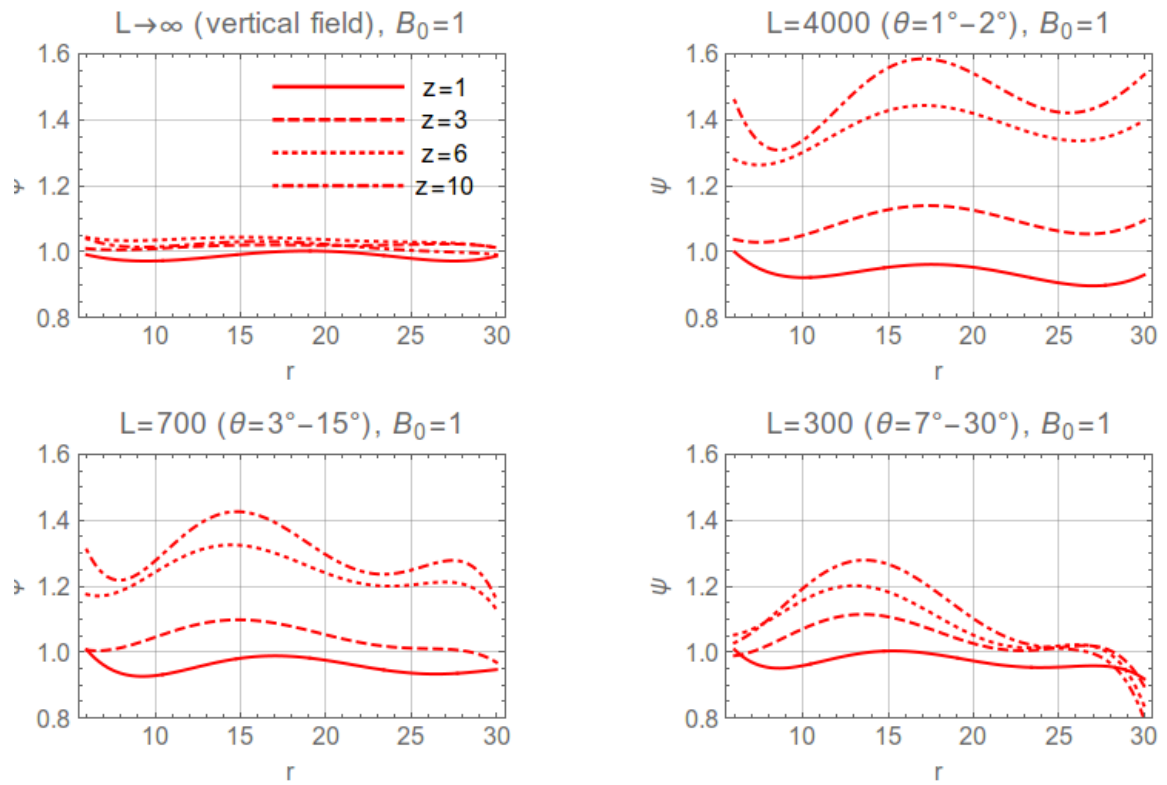


Figure 4.12: Similarly to figure 4.11, normalized values for  $\psi(r, z, t)$ . This time in the moderate-field atmosphere, where the FWRH lies at around  $z = 3-4$ , as per figure 4.9. In this atmosphere we do expect mode conversion to occur.

in  $\psi$  suggests that no Alfvén waves have been created, which is what we had originally anticipated; a mixture of Alfvénic and fast magneto-acoustic oscillations are travelling to the top of the box without mutual interaction.

In the moderate field atmosphere of figure 4.12 however we see a clear signal of the resonance taking effect. Once again we see exactly what is expected for the vertical field case (no mode conversion); however when the field starts to become twisted with an inclination from the vertical, the mode conversion becomes apparent. There is a small increase in  $\psi$  at  $z = 3$  (approximately at the FWRH), while the most noticeable growth occurs between  $z = 3$  and  $z = 6$ . Clearly the resonance kicks in at this height range, while the Alfvén speed profile is still somewhat exponential in its growth. The production seems to slow down in the near-uniform field near the top of the box at  $z = 10$ .

Significantly, the Alfvén wave production appears to be most efficient at lower twist and field inclination, with up to a 60% increase seen in this case (top-right panel of figure 4.12). The amplitude of enhancement drops by around 20% when the field is at its most inclined and twisted ( $L = 300$ ,  $\theta = 7^\circ - 30^\circ$ ). This basic behaviour seems to match the cold-plasma, uniform field findings of Cally & Hansen (2011) quite well. In that work (as well as in the work of Khomenko & Cally (2012)) it was found that the upwards Alfvén conversion coefficient was at a maximum for lower values of  $\theta$ , even approaching total conversion for low  $\theta$ ,  $\phi \approx 90^\circ$  and for small  $k_h$ .

It is interesting to note that we see the same cold-plasma behaviour in the uniformly twisted field as in the uniform inclined field even though in our domain,  $\theta$  is a function of  $r$ , and we have a spread of inclinations brought about by the twisted field. The production of Alfvén waves are still strongly influenced by the field inclination, with a maximum at more vertical field, even though conversion is identically 0 in the purely vertical case.

#### **The Alfvén wave as a function of $\phi$ .**

The wave-to-field attack angle is another important piece of the puzzle which we have so far neglected in our analysis. In the uniform inclined field study of Cally & Hansen (2011) (figure 4.4 in this chapter) one can see that for field inclinations of between

$10^\circ \leq \theta \leq 30^\circ$  (the first 3 panels) the maximum in the forward (upwards in our case) Alfvén coefficient occurs at around  $\phi = 80^\circ\text{--}90^\circ$ , with the maximum shifting towards lower values of  $\phi$  with a smaller magnitude for greater field inclinations. Also the production of field-aligned (upwards) travelling Alfvén waves is very much shifted to the  $\phi < 90^\circ$  side of the contour plots whereas the anti-aligned (downwards in our case) Alfvén wave is preferred for  $\phi > 90^\circ$ . Fast-Alfvén mode conversion occurs because the phase velocities of the two wave types match at the FWRH (just below the resonance layer) and so it is no surprise that when the fast wave has a component in the field direction, Alfvén waves with field-aligned wavevectors will be created preferentially.

In our case the twisted field that we have prescribed could, in a simple way, represent the upper-atmospheric field above and around a sunspot in the low- $\beta$  chromosphere and corona. It is therefore natural to ask whether we might see a similar effect in such a twisted field as we would in the uniform field case. In other words could the creation of Alfvénic waves at chromospheric heights (by fast-Alfvén mode conversion) be filtered by not only by the field inclination but also by the attack angle between the fast wave (at the FWRH) and the field. We attempt to answer this question by varying the azimuthal wavenumber,  $m$ , of the wave driver source, which results in a corresponding change in  $\phi$ .

The quantities we have examined so far have corresponded to the  $m = 0$  azimuthally symmetric wave. The reader will recall that we extracted the  $m$  dependence from our displacements via a simplification of the form  $\xi(r, \Phi, z, t) = \xi(r, z, t)e^{im\Phi}$ , which reduces the dimensionality of the problem and essentially turns  $\Phi$  and  $m$  into parameters of our choosing. Choosing a value of  $\Phi$  corresponds to taking a slice through the cylinder and solving on that  $r, z$  plane. The  $m = 0$  wave is invariant to the choice of  $\Phi$  as it is azimuthally symmetric, however for non-zero  $m$  the value of  $\Phi$  can be important. In this work we have found that while altering the choice of  $\Phi$  alters the characteristics of the wave noticeably (as would be expected for non-zero  $m$  values), the properties of the mode conversion remain relatively consistent. Therefore all of our analysis proceeds with the choice  $\Phi = 0^\circ$ .

The point to varying the value of  $m$  is that in doing so, we are actually varying the wavevector-to-field attack angle,  $\phi$ , since  $k_\Phi = m/r$ . In the case of a uniform

inclined field it would be much simpler to alter  $\phi$  in or out of the wavevector plane by simply rotating the field. However with the uniform twist formulation we are much more constrained as to how we can alter the field. The most readily achievable way of altering  $\phi$  is by varying  $m$ . We can describe how this variation affects  $\phi$  by firstly considering the uniform twist field itself. The field prescription is of the form  $\mathbf{B} = (0, B_\Phi(r), B_z(r))$  and thus has no radial component. At the FWRH the waves we drive have become completely horizontal as they begin to turn over and so have wavevectors of the form  $\mathbf{k} = (k_r, k_\Phi, 0)$ , where once again  $k_r$  is chosen initially and  $k_\Phi = m/r$  is determined by our choice of  $m$  and by the range of  $r$  in the domain. If  $m = 0$  the wave will be purely radial (at the FWRH) with wavevector  $(k_r, 0, 0)$  and will strike the field at exactly  $\phi = 90^\circ$ . However for non-zero  $m$ , waves will be incident on the field at some angle other than perpendicular, as they will have a component  $k_\Phi = m/r$  in the  $\Phi$  direction which varies as a function of  $r$ .

With our choice of field parameters, performing simulations with  $-10 \leq m \leq 10$  for integer  $m$  produces a reasonable variation in  $\phi$ , such that we can analyse the mode conversion as a function of attack angle. To be clear,  $\phi$  in this case will correspond to the angle between the wavevector and field *at the FWRH*, when  $k_z = 0$ . Thus  $\phi$  measures the attack angle when resonance occurs, which is of most importance. Figure 4.13 displays the range of values of  $\phi$  that we achieve with these choices of  $m$  for the 4 different field twist atmospheres. In general it can be seen in the figure that the attack angle becomes more acute as  $|m|$  increases in all fields except for the purely vertical field.

In terms of directionality, azimuthal wavenumbers  $m < 0$  are striking at an angle that is anti-aligned with the field (signified by values of  $\phi > 90^\circ$ ) whereas the  $m > 0$  waves have a field-aligned component. Importantly however, the figure shows that varying the field twist,  $L$ , also modifies the relationship between  $m$  and  $\phi$  significantly. We can see that with a more twisted field the spread in  $\phi$  caused by altering  $m$  is much greater. If the field becomes untwisted and vertical, variation in  $m$  produces little change in  $\phi$ . In the vertical field case all values of  $m$  produce an attack angle of  $90^\circ$ . In the more twisted field cases we get a reasonable spread of attack angles (up to  $\approx 40^\circ$  on either side of perpendicularity for the  $L = 300$  case) with which to conduct our parameter study.

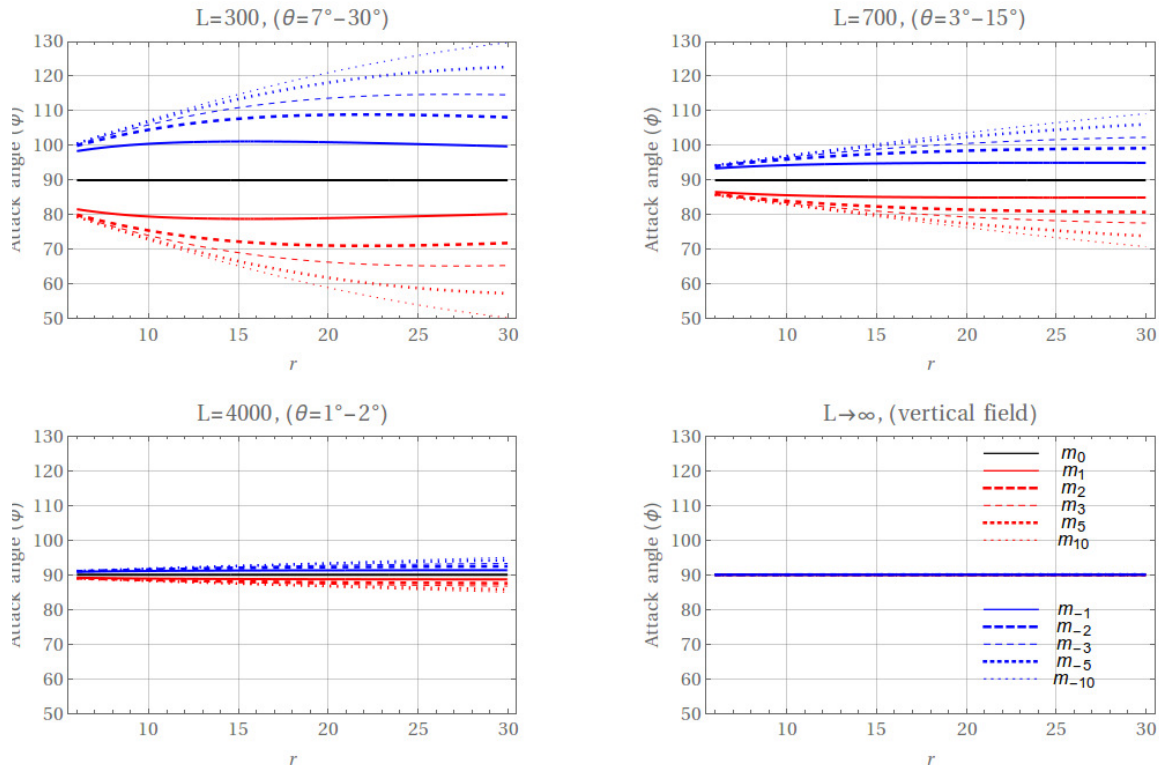


Figure 4.13: Values of  $\phi$  (at the FWRH) over the radial domain for a variety of  $m$  waves. Top left panel: Field twist case  $L = 300$ , top right:  $L = 700$ , bottom left:  $L = 4000$ , bottom right: vertical field.

With the range of field inclinations determined by  $L$  (shown in figure 4.5), variations in  $\phi$  (figure 4.13) and a small value of  $\kappa$  (defined as the density-scaled horizontal wavenumber as discussed earlier) we are in some sense in a similar parameter space to the first three panels of figure 4.4, specifically the region of the figures where  $\kappa \ll 1$ .

We begin by quantifying the Alfvén wave signal as a function of  $\phi$ , comparing the Poynting flux of the  $m = 0$  wave to waves with varying  $m$  values. From the full Poynting vector  $\mathbf{S}(r, z, t)$  we have calculated the time-averaged values of the field-aligned component of the Poynting flux,  $S_f$  (where  $S_f = \hat{\mathbf{B}} \cdot \mathbf{S}$ ), over a period of time around the height  $z = 10$ , which is well above the FWRH. The time period for averaging is long enough for several wavefronts to pass through the measurement height, before passing through the top of the box (where they are absorbed by the radiative boundary conditions at  $z = 12$ ). It is worth noting that we could just

### 4.3. SIMULATION RESULTS

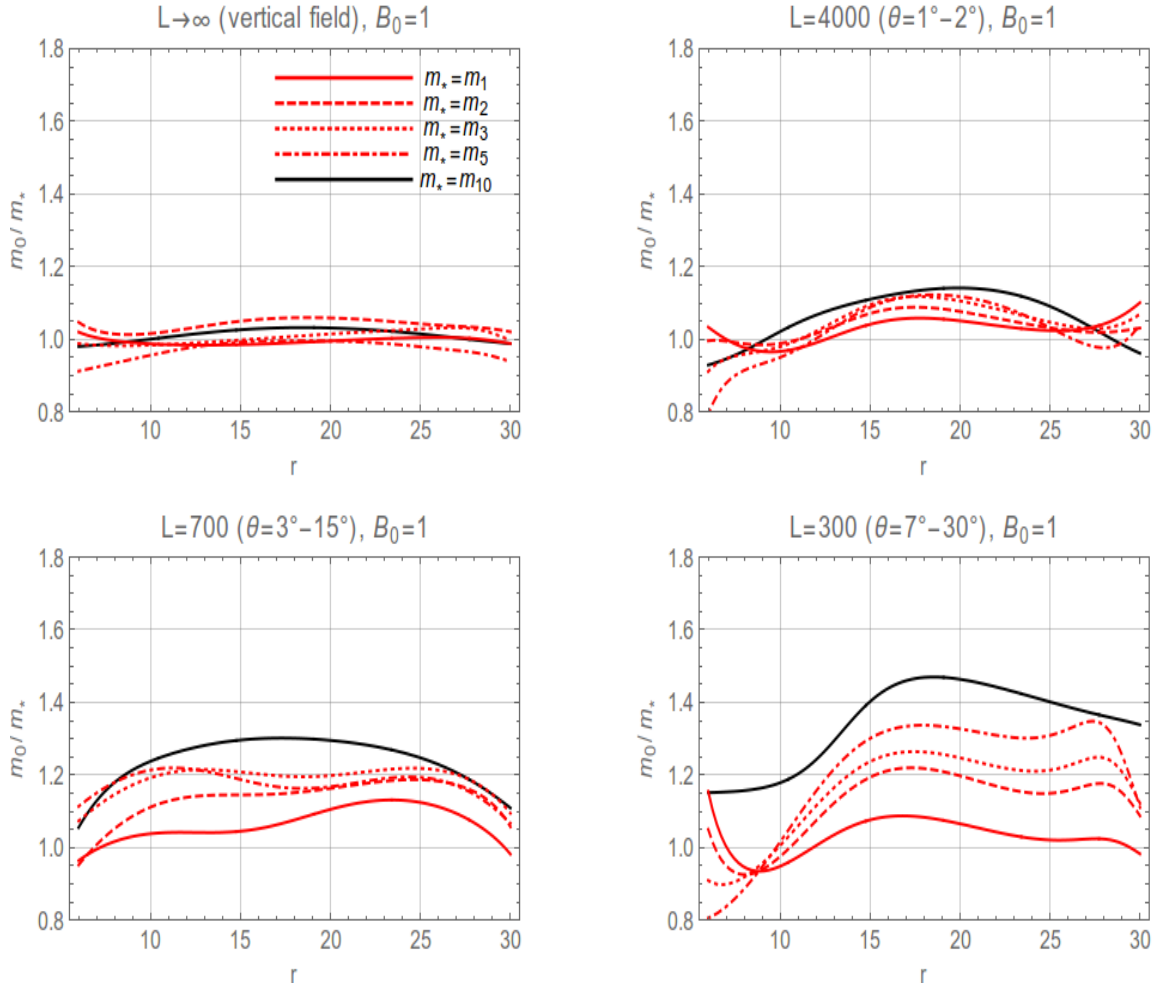


Figure 4.14: Radial ratios of  $S_f$  for the  $m = 0$  wave with respect to  $S_f$  for other positive  $m$  value waves for  $1 \leq m \leq 10$ . In this atmosphere  $B_0 = 1$  and each panel corresponds to a different twist parameter. A value of 1 indicates parity with the  $m = 0$  wave.

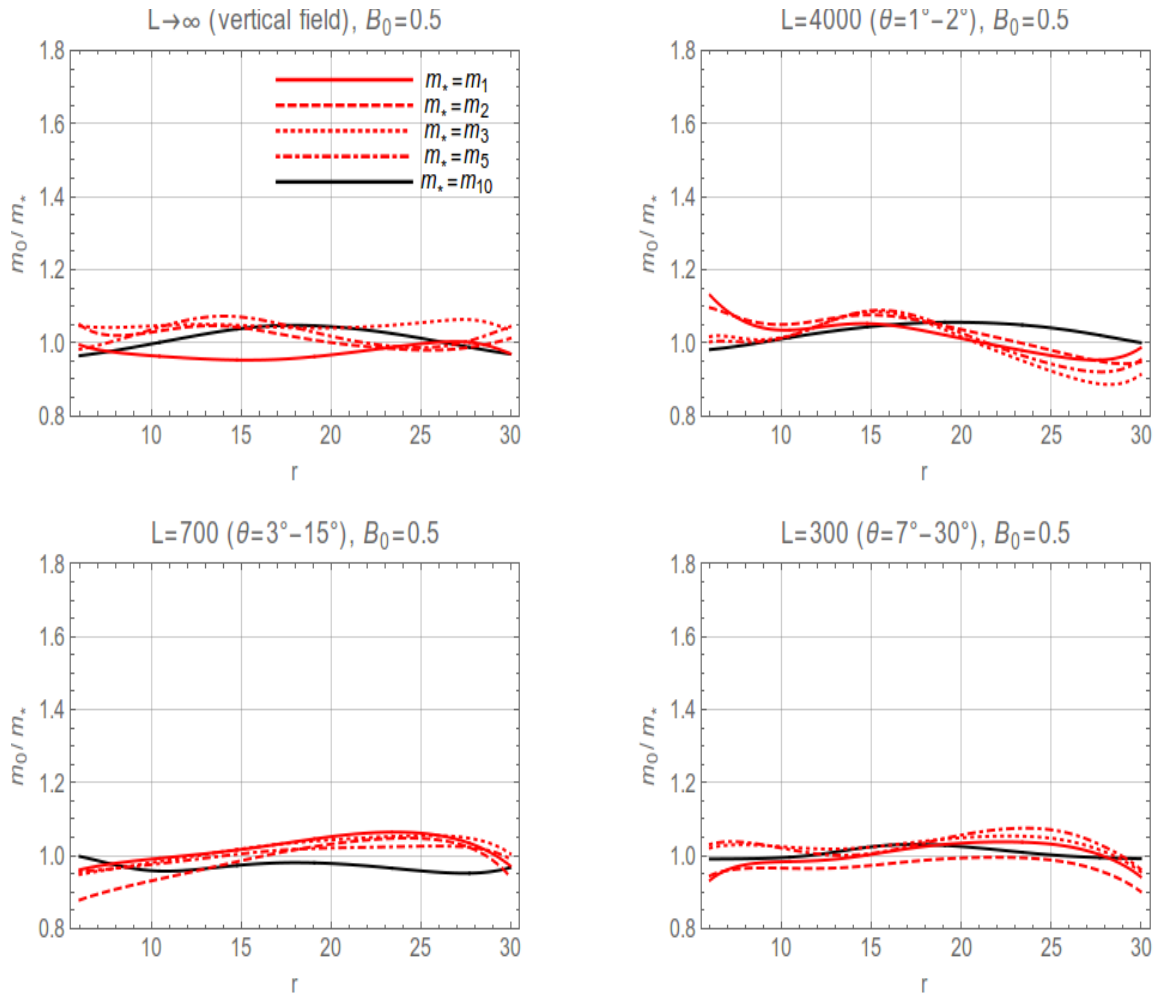


Figure 4.15: The same quantities as the previous figure, except  $B_0 = 0.5$  in this case. As such the FWRH is above the top of the box and no mode conversion can occur.

as easily have kept using the quantity  $\psi$  to track the Alfvén wave from this point, however the field aligned component of the Poynting flux serves as a more intuitive proxy for Alfvén waves travelling out of the top of the box (and the results are quite similar in any case).

Figures 4.14 and 4.15 show the ratios of  $S_f$  for the  $m = 0$  wave with respect to positive  $m$  waves for  $1 \leq m \leq 10$ . Figure 4.14 corresponds to the  $B_0 = 1$  atmosphere whereas the latter figure is  $B_0 = 0.5$  (no mode conversion). Each panel corresponds to a differently twisted field similarly to the figures in the previous section, and as per figure 4.13 we know that these twist parameters correspond to a range of FWRH attack angles depending on the field twist and the value of  $m$  possessed by the driven wave.

In the vertical field case for the  $B_0 = 1$  atmosphere there is no mode conversion and as we would expect there does not appear to be any consistent relationship between the magnitude of the Alfvén waves and the attack angle at the FWRH. The Poynting flux measured in this case is a result purely of the mixed Alfvén-fast waves driven at the bottom boundary. The attack angle at the FWRH is still relevant of course as fast waves will turn over and undergo reflection. However no Alfvén production will occur. Looking at the near-vertical field case (top-right panel) next, we can tentatively suggest a hint of a pattern developing. The  $m = 0$  wave is slightly greater in magnitude (at most points) than the  $m = 1$  wave. In fact for each successive value of  $m$  the Poynting flux decreases slightly, with a total difference in flux of around 10% between the  $m = 0$  and  $m = 10$  waves. The difference between the flux for the various values of  $m$  increases dramatically for greater values of field twist (bottom panels), increasing to around a 50% difference for the  $L = 300$  maximum twist case.

Figure 4.12 in the previous section showed that the mode conversion appears strongest in the near-vertical (low  $\theta$ ) field case. However when we examine the mode conversion here as a function of  $\phi$  we find that there is a noticeable sensitivity to the attack angle that is much more pronounced at greater field twist (higher values of  $\theta$ ). This is a direct consequence of figure 4.13; at greater twist there is a much larger difference in the attack angle of the fast waves as a function of  $m$ , and we have shown that this is manifested directly in the fast-Alfvén conversion. It appears that

conversion is clearly maximised at  $\phi = 90^\circ$  (the  $m = 0$  wave) with a noticeable drop off as fast waves reflect at more acute angles. The fact that we do not see this in the near-vertical field ( $L = 4000$ ) case makes perfect sense, as there is very little change in fast wave  $\phi$  as a function of  $m$  for this field, even though fast-Alfvén conversion is at its most efficient and pronounced in this field configuration.

At this point one might ask whether this  $m$ -dependent behaviour really is a consequence of fast-Alfvén mode conversion. How can we be sure? Figure 4.15 provides some surety to our claim that the flux we are measuring is a result of Alfvén waves created in the resonant layer. In the weak-field  $B_0 = 0.5$  atmosphere it is clear that the same behaviour is not repeated. There is no significant change in  $S_f$  as a function of  $m$  in any field configuration as no fast-Alfvén mode conversion can take place in these atmospheres. Both the fast and the Alfvén waves travel to the top of the box, and so there is no real variation in the strength of the Alfvén oscillation.

Of further interest are the results when we examine the conversion for  $\phi > 90^\circ$ . The results of Cally & Hansen (2011) (figure 4.4) show that the maximum in field-aligned Alfvén wave production occurs at around  $\phi = 90^\circ$  for near-vertical field, however the maximum shifts towards lower magnitudes and lower  $\phi$  values for greater inclinations.

We can see from figure 4.16 the difference when we compare the  $m = 0$  to the negative  $m$  waves, over the same attack angles for the  $B_0 = 1$  atmospheres. These waves correspond to  $\phi > 90^\circ$ . It can be seen that there is an even more significant drop off in the upper atmospheric Alfvén wave presence for these obtuse attack angles. In the highly twisted case we can see an approximate doubling of  $S_f$  for the  $m = 0$  wave as compared to the  $m = -10$  wave (as compared to a 50% difference between  $S_f$  for  $m = 0$  and  $m = 10$ ). This suggests that the fast-Alfvén conversion efficiency drops off more rapidly for  $\phi > 90^\circ$  than it does for  $\phi < 90^\circ$ . In other words the production of field-aligned Alfvén waves at the resonance is not symmetrically favoured about  $\phi = 90^\circ$ . The creation of these Alfvén waves is favoured for  $\phi < 90^\circ$  (positive  $m$ ) fast waves. Once again figure 4.17 shows us no such relationship in the weak-field atmosphere case, which is again reassuring.

These result are perhaps brought out more clearly by figure 4.18, which is a more compact summary of figures 4.14 – 4.17. In the figure we have taken the

### 4.3. SIMULATION RESULTS

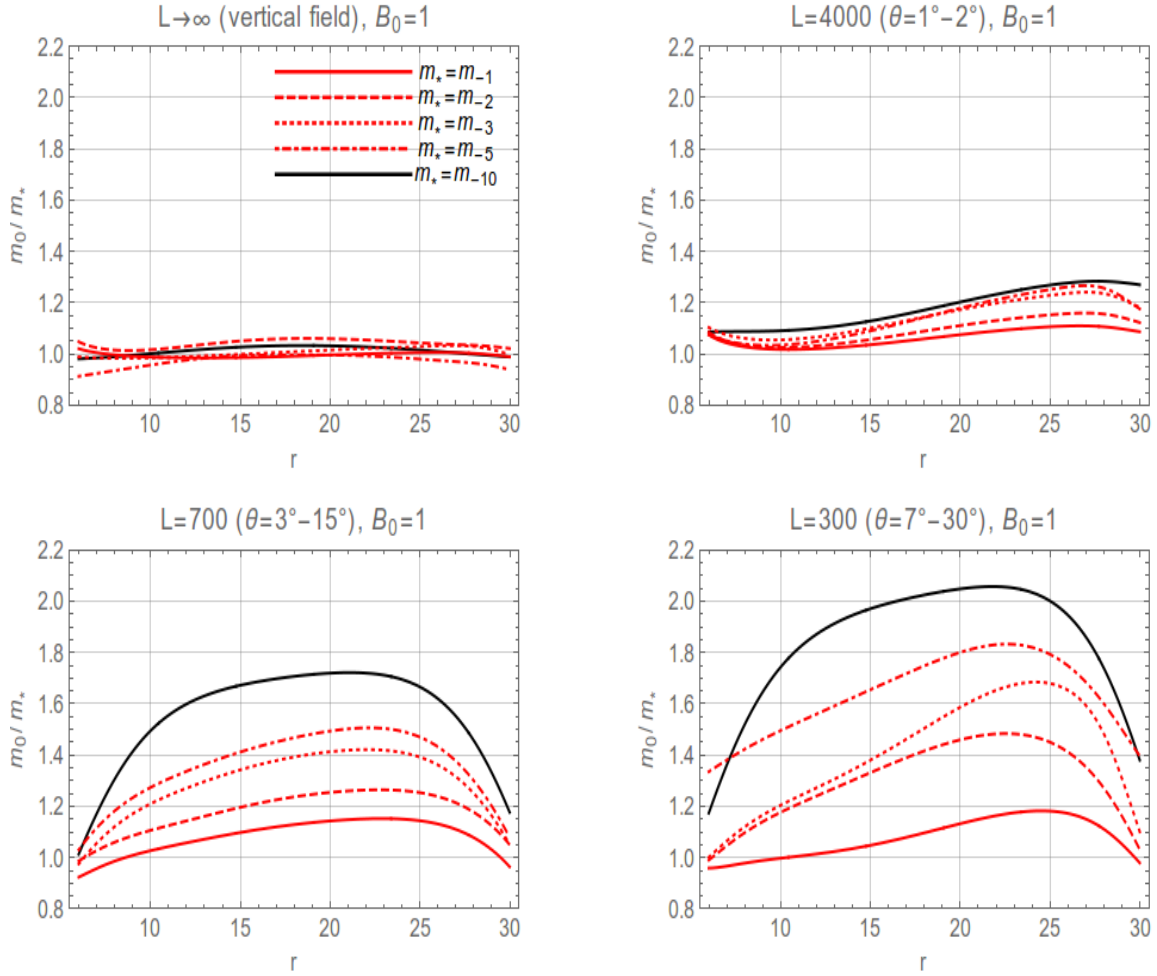


Figure 4.16: Similarly to figure 4.14, radial ratios of  $S_f$  for the  $m = 0$  wave with respect to  $S_f$  for other *negative*  $m$  value waves for  $-10 \leq m \leq -1$ . In this atmosphere  $B_0 = 1$  and each panel corresponds to a different twist parameter. A value of 1 indicates parity with the  $m = 0$  wave.

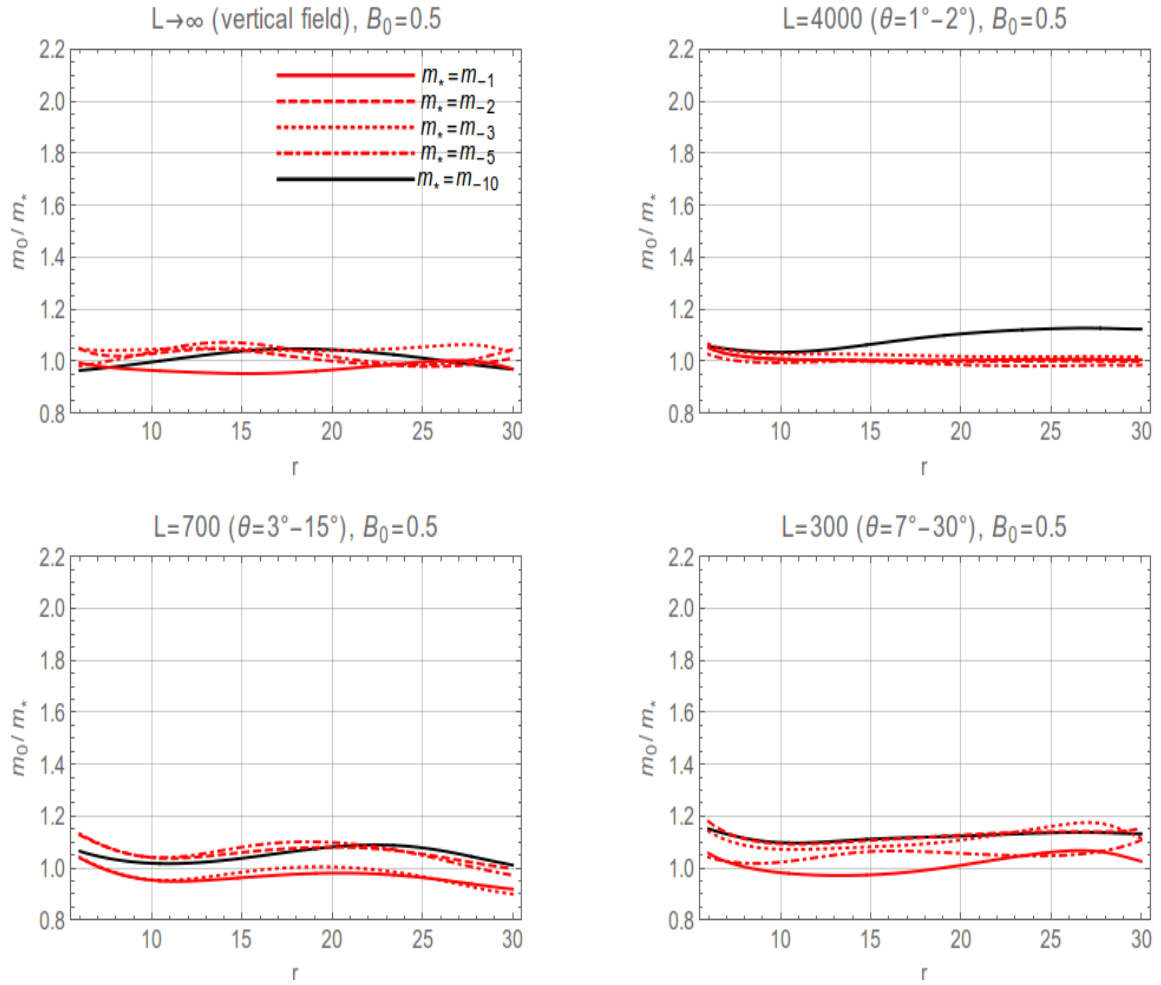


Figure 4.17: The same quantities as the previous figure, except  $B_0 = 0.5$  in this case. As such the FWRH is above the top of the box and no mode conversion can occur.

### 4.3. SIMULATION RESULTS

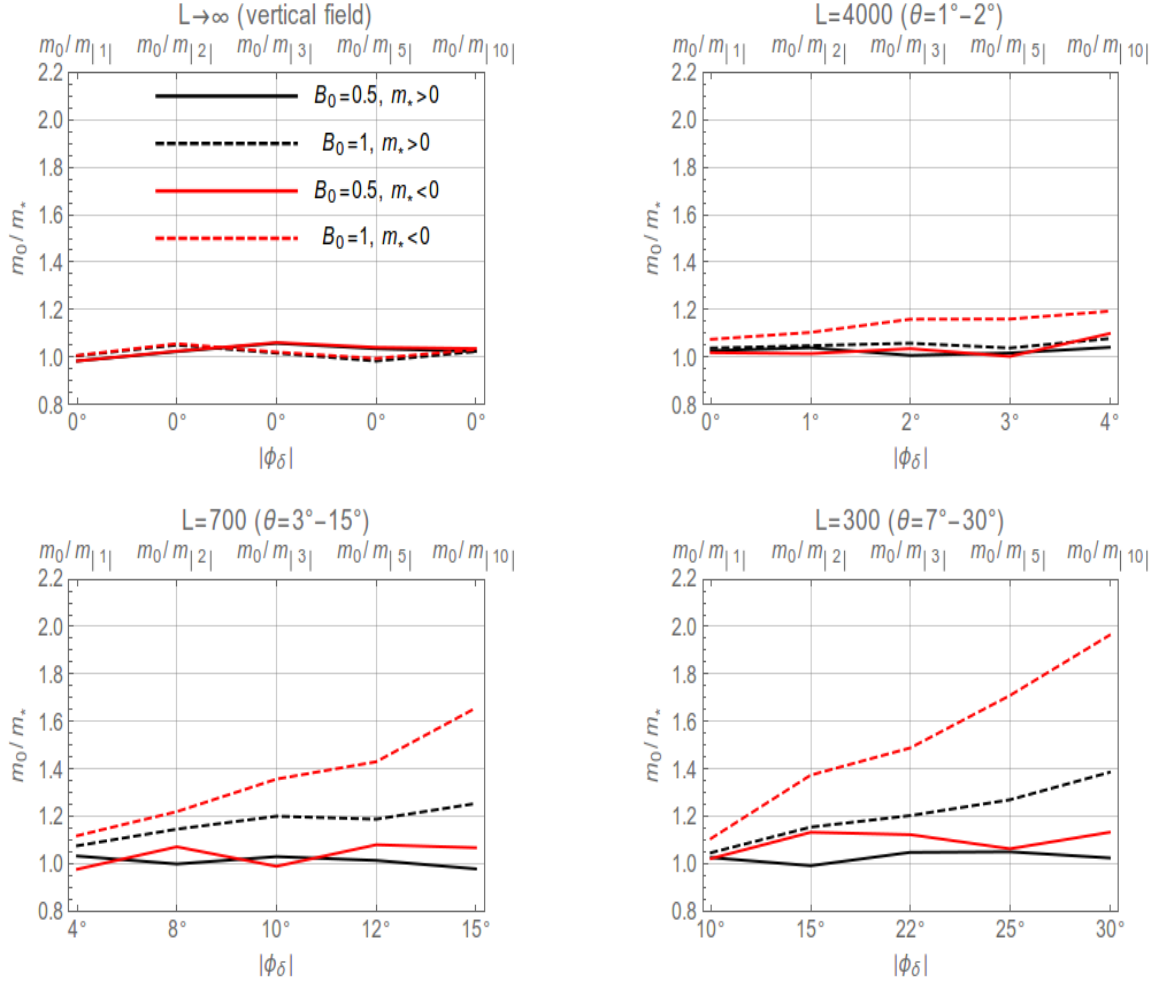


Figure 4.18: Each curve in these plots represents the  $r$ -averaged  $S_f$  ratio of  $m_0$  to  $m_*$  (at the Alfvén measurement height  $z = 10$ ) as a function of the  $r$ -averaged attack angle which the fast wave exhibits at the FWRH.  $\phi_\delta$  is the average unsigned deviation from  $90^\circ$  for that particular wave.

radial average of each of the  $m$  curves from figures 4.14 – 4.17. We have then plotted this averaged  $S_f$  as a function of the average  $|\phi|$  which each  $m$  value corresponds to (where we are ignoring the sign of  $\phi$  which is determined by the sign of  $m$ ) - recalling of course that each  $m$  value corresponds to a *range* of  $\phi$  values over  $r$ . The black curves correspond to the ratios between  $m_0$  and positive  $m$  value waves (as in figures 4.14 and 4.15) whereas the red curves correspond to figures 4.16 and 4.17 (negative  $m$  value ratios). Solid curves are the  $B_0 = 0.5$  atmospheres with no mode conversion, while the dashed curves are the  $B_0 = 1$  atmospheres. One can clearly see here the decrease in  $S_f$  as a function of  $\phi$  and  $m$  in the more twisted fields (bottom two panels) for the  $B_0 = 1$  atmosphere. Once again there is very little variation in the  $L = 4000$  slightly twisted field case or in any  $B_0 = 0.5$  atmosphere.

It is clear that the conversion efficiency for the forwards travelling Alfvén wave is much more efficient for  $m > 0$ . In exploring this further we directly compare the  $S_f$  ratio between positive and negative  $m$  waves for the same two atmospheres ( $B_0 = 0.5$  and 1) ignoring the  $m = 0$  wave. In the vertical field case of figures 4.19 and 4.20 we observe very little difference in the flux based only on the sign of  $m$ . This is to be expected as the vertical untwisted field is azimuthally symmetric and so the sign of  $m$  will not alter the character of the wave. Indeed this difference should analytically be 0 but as we are taking spatial and temporal averages over a numerical simulation we see some negligible difference. The panels of increasing twist in figure 4.19 show a ratio between positive and negative  $m$  value waves which grows as a function of field twist. This corroborates the earlier figures and indicates that we are seeing a greater Alfvén wave signal at the top of the box for positive  $m$  waves (by up to 40% in the  $L = 300$  case). Once again these features are not present in the  $B_0 = 0.5$  atmosphere (figure 4.20), as we expect.

## 4.4 A Summary and Discussion of Results

In this chapter we have carried out a thorough analysis characterising the efficiency of fast-Alfvén mode conversion in a simplified, force-free, azimuthally twisted, cold plasma ( $\beta = 0$ ) atmosphere with a stratification. In accomplishing this we have

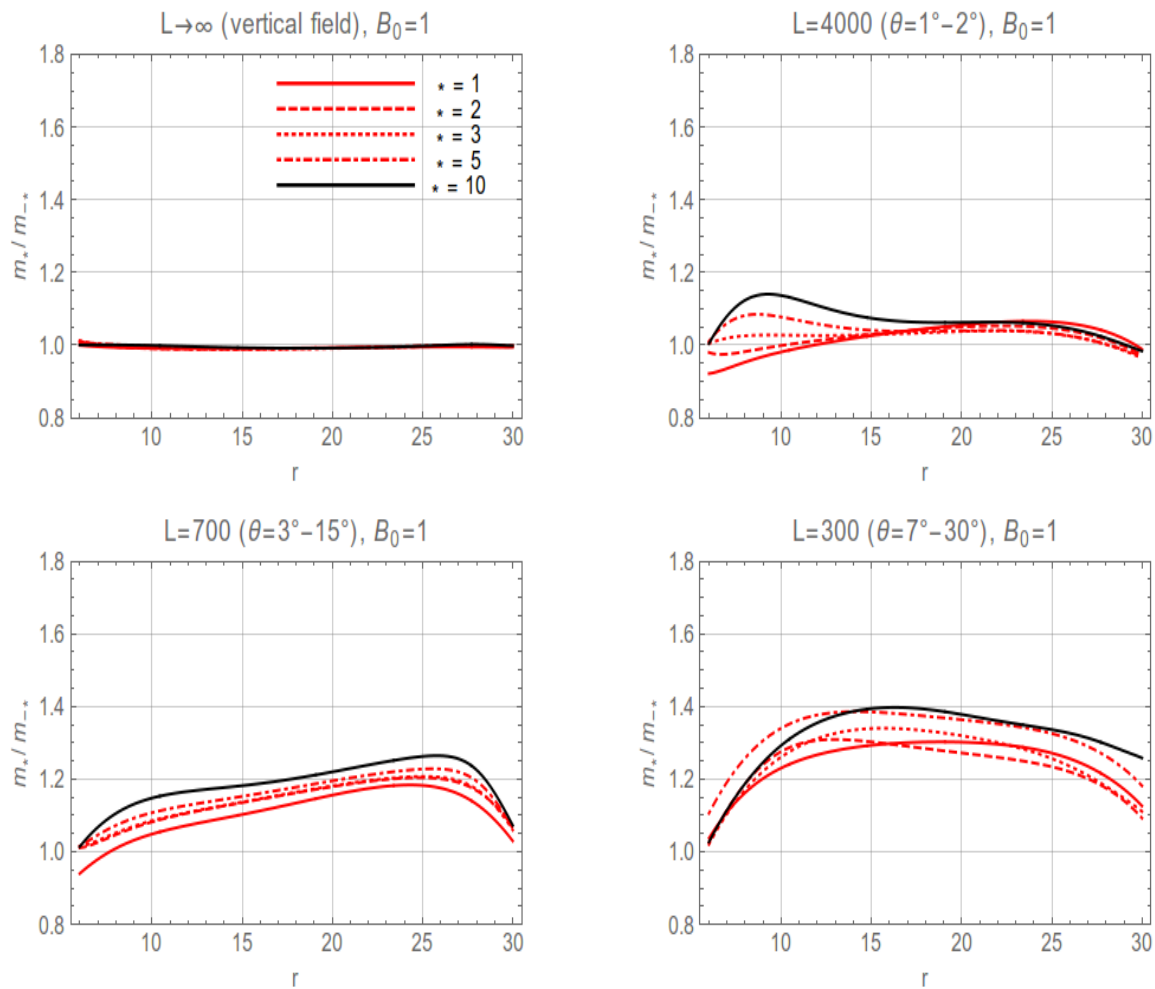


Figure 4.19: Radial ratios of  $S_f$  for positive  $m$  wave with respect to  $S_f$  for negative  $m$  value waves, for  $10 \leq |m| \leq 1$ . In this atmosphere  $B_0 = 1$  and each panel corresponds to a different twist parameter. A value of 1 indicates parity between the positive and negative  $m$  waves.

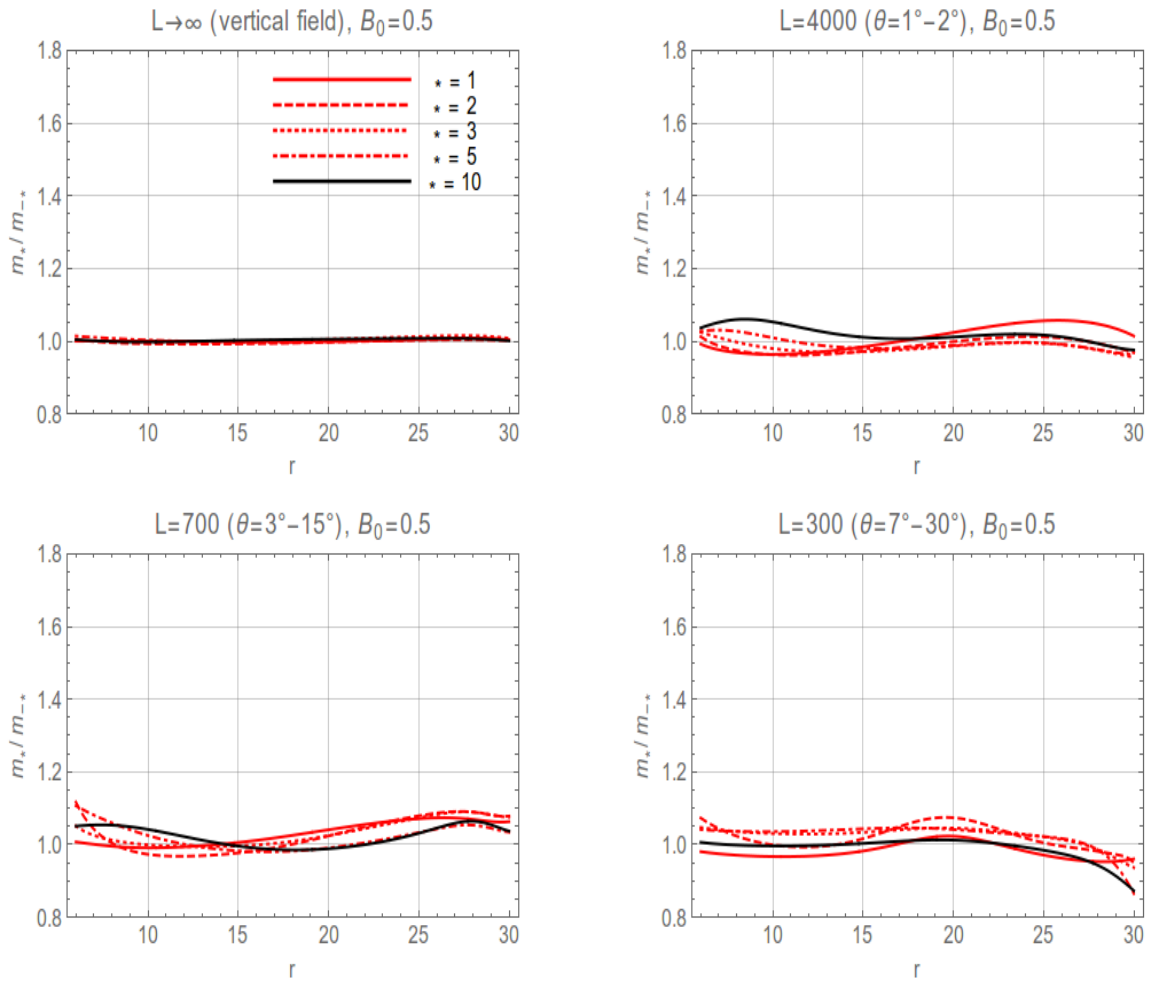


Figure 4.20: The same quantities as the previous figure, except  $B_0 = 0.5$  in this case. As such the FWRH is above the top of the box and no mode conversion can occur.

driven a perturbation in a single component of the vector displacement at the bottom boundary of a semi-cylindrical domain. The perturbation represents a combination of fast magneto-acoustic waves and Alfvén waves (the slow wave is frozen out in a cold plasma atmosphere) which propagate upwards in the direction of increasing Alfvén speed. We have then measured the strength of the Alfvén wave at a sampling height at the top of the box via calculation of the Poynting flux (as an Alfvén wave proxy) in a range of atmospheric configurations, essentially conducting a parameter study in the field twist, inclination and the wavevector-to-field attack angle parameters.

Key to our analysis is that the bottom boundary lies below the FWRH and therefore below the Alfvén resonance where the mode conversion begins to take place. Above the FWRH the fast waves will only exhibit an exponentially decaying (evanescent) presence and as such at the upper sampling height the only wave type present will be the Alfvén wave. We have compared the Alfvén wave strength to that in similar simulations where fast-Alfvén mode conversion is prohibited from occurring, such as in precisely vertical field or in the case where the FWRH is well above the box top. We summarise the relevant findings of this study as follows:

1. Fast waves (measured via the dilatation  $\chi = \nabla \cdot \boldsymbol{\xi}$ ) decay as expected at their classical reflection height in the twisted field atmosphere, leaving only an exponentially decaying tail above the FWRH.
2. There is a significant increase in the magnitude of the Alfvén wave energy which is generated above the FWRH. In a comparison weak-field atmosphere, where the FWRH (and hence the resonance layer) is located well above the top of the box, this increase is not present. The enhancement in the Alfvén wave is generated from fast-Alfvén mode conversion and in the case of the  $m = 0$  fast wave studied here resulted in a 20 – 60% increase (depending on the background field twist) in field-aligned Alfvén flux.
3. We have shown that the mode conversion in this field structure is broadly similar to the uniform field study of Cally & Hansen (2011) and Khomenko & Cally (2012). The conversion efficiency to the field aligned Alfvén wave is strongly

dependent on the field inclination ( $\theta$ ), being strongest as  $\theta \rightarrow 0^\circ$ . However the conversion is non-existent when the field is identically vertical, at  $\theta = 0^\circ$ .

4. The conversion is maximised when the attack angle between the fast wave and the background field at the FWRH ( $\phi$ ) is  $90^\circ$  as evidenced by the fact that the  $m = 0$  wave always seems to produce the strongest Alfvén signal. Subsequently changing the  $m$  value of the fast waves alters  $\phi$  away from this value and weakens the conversion. Atmospheres with a greater twist yield a greater radial spread of  $\phi$  as  $m$  is varied, and we have shown that this results in a strong difference in the Alfvén wave signal.
5. The upwards (field-aligned) Alfvén wave is strongly preferred by fast waves with  $\phi < 90^\circ$ , i.e. with a component in the direction of the field, rather than against it. Put simply, as summarised in figure 4.18, positive  $m$  ( $\phi < 90^\circ$ ) fast waves produce more upwards travelling Alfvén waves than negative  $m$  fast waves. We make no attempt to quantify the downwards travelling Alfvén wave as is done in Cally & Hansen (2011).

The complexity and limitations of the uniform twist field has meant that we have been limited to a smaller parameter space than Cally & Hansen (2011). We have not really been able to explore the mode conversion for field inclinations approaching horizontality or for a range of initial fast wave wavevectors. In addition we have not attempted to decompose the Alfvén wave generation into upwards and downwards travelling components.

The properties that we have uncovered however are significant and show us that the generation of upwards-travelling chromospherically generated Alfvén waves can be significant provided  $\mathbf{k}$ ,  $\phi$  and  $\theta$  are in an agreeable configuration.

# Chapter 5

## Concluding Remarks

To conclude this thesis we present this brief chapter summarising the key findings detailed in chapters 2, 3 and 4 and discussing their context.

We begin by presenting a short summary of the SPARC forward wave modelling which we have pursued as well as the results obtained from these simulations in chapters 2 and 3; In particular we discuss where our simulations succeed and fail in capturing the halo effect and where progress could be made in the future.

To finish we discuss the conclusions derived from modelling fast-Alfvén mode conversion in a semi-analytic twisted field atmosphere (chapter 4) and compare our results to previous studies.

## 5.1 The Acoustic Halo

Chapters 2 and 3 have detailed our efforts to address the uncertainty surrounding a very specific solar physics problem; that of the acoustic (or seismic) halo. The phenomenon has been well known for several decades now, with Braun et al. (1992b) providing the initial observations. The halo manifests itself as a curious enhancement in the time-averaged Fourier power of Doppler velocity time-series observations at frequencies above the acoustic cut-off (non-trapped oscillations). This enhancement occurs outside of the penumbra of sunspots and active regions amongst relatively weak-to-moderate and horizontally inclined magnetic field and exhibits a frequency-dependent magnitude in the range 20-70% over quiet-Sun values.

Various halo-formation mechanisms have been proposed, which we have summarised at the beginning of chapter 2. We have also discussed the validity of these mechanisms based on our numerical results in the discussion at the end of chapter 3. Based on the original assertion of Khomenko & Collados (2009), our goal has been to argue that the halo is entirely governed by processes occurring in the *overlying* magnetically dominated atmosphere. Specifically we have argued that the halo enhancement is manifested as additional energy deposited onto observational heights by the refraction and return of fast magnetic and acoustic waves, as described by the theory of fast-slow mode conversion. We will not delve again into the mechanics behind this process as it has been sufficiently covered in chapter 2; instead we will summarise our findings and conclusions.

In chapter 2 we modelled a localised halo enhancement by setting off a pulse in  $v_z$  at depth below the surface of the photosphere of a realistic MHS sunspot atmosphere and allowing the resulting oscillations to propagate upwards and through the sunspot. In characterising a power enhancement we calculated the  $v_z$  Fourier power at every grid point in the simulation domain and compared with the power at every grid point of a similar quiet-Sun simulation. We showed a significant enhancement in 6.5 mHz frequency-filtered power, while there was no enhancement in the low-frequency (3.5 mHz) equivalent power.

Further analysis revealed that the spatial structure of the enhancement follows the position of the  $a = c$  equipartition layer extremely closely, which indicates a

connection between the physics of fast-slow mode conversion and the generation of an enhancement. Furthermore the enhancement occurs at quite inclined field at moderate-to-weak field strength, which is a key property of observed halos.

A striking feature which we uncovered was also that the 6.5 mHz power enhancement magnitude appears to be a function of how much room is left *above* the equipartition layer for upwards-travelling fast waves to refract in. When we do not permit fast waves to refract and return after undergoing mode conversion at the  $a = c$  layer, the enhancement disappears completely.

The results of the chapter showed, quite unexpectedly, that a halo-like power enhancement can be produced from the simple interaction between a wave and a magnetic field. The enhancement is not reliant on the photospheric physics that we we have neglected to model, such as active region fine structure. Instead we have shown that the formation of the enhancement is governed by the structure of the sunspot  $a = c$  equipartition layer, the inclination of the magnetic field and the characteristics of the waves incident upon that field.

In chapter 3 we showed a little more rigorously that the enhancements found in chapter 2 are indeed acoustic halos. Here we modelled the solar photospheric  $p$ -mode bath with a spatially distributed source function wave driver. The driver was initiated at a depth of 150 km below the photosphere and allowed to saturate the simulation domain. The reasoning behind applying such a driver was that we would be able to compare simulated halos with actual Doppler velocity observations and compare the simulated and observed characteristics. Our 6-hour time averaged  $v_z$  halos are in broad agreement with those observed around the active region NOAA 11092. In particular the enhancement occurs around similarly inclined field at approximately the same field strengths.

We found that the halos in both chapters 2 and 3 exhibited a consistently larger magnitude than the observed halo by a factor of 2 or even 3. We attribute this to several factors (which we have discussed in chapter 3): the first being that we do not model any filamentary fine structure around the outer extent of our sunspots. As studies have shown (Weiss et al., 2004; Thomas et al., 2006), there is a combed structure with great variation in field inclination at outer penumbral distances which may significantly lessen the effectiveness of the fast-slow mode conversion process, due

to the verticality of field in the lighter filamentary lanes. Secondly we have performed these studies under the framework of ideal MHD. The actual solar photosphere is far from fully ionized and so there may be ion-neutral dissipation in play which could significantly reduce halo magnitudes. Finally our sunspot atmosphere contains greater expanses of uninterrupted nearly-horizontal field than NOAA 11092, which is more conducive to the conversion to the fast magnetic MHD wave.

Features like the dual-ring halo structure in our simulated halos are definitely present in observations, however they are not as pronounced. We have shown quite clearly that the dark gap (corresponding to a lack of enhancement) between the dual halo rings (in simulations) correlates to the generation of upwards-travelling Alfvén waves. Presumably fast magnetic wave energy is lost to the Alfvén wave at these radii, where the fast-Alfvén mode conversion is effective. The distributed source halos also show a complete reliance on the overlying atmosphere in order to be generated, as we have shown that enhancements at *all* frequencies disappear when the return of the fast wave is restricted.

Through the results of these studies, we are confident that fast-slow mode conversion is responsible for the acoustic and intensity halos seen around active regions. It can satisfactorily explain the vast majority of observed halo properties, and provides the most believable framework for the creation of the enhancement.

## 5.2 Fast-Alfvén Mode Conversion

The discussion at the end of chapter 4 details the major findings from this study, where we have determined the range of parameters under which the conversion of fast wave energy to (upwards-travelling) Alfvén wave energy is most efficient in this particular twisted magnetic field geometry. The bulk of the results seem to conform to the uniform inclined field study of Cally & Hansen (2011) as well as the later studies of Khomenko & Cally (2012) and Felipe (2012) which did not incorporate azimuthal twist into magnetic field structure.

As discussed, the transverse oscillations observed in the corona are quite likely Alfvén waves. This possibility has led to much discussion implicating the waves as carriers of the necessary energy for coronal heating. In order for Alfvén waves to

fulfil this heating role, it is first necessary to determine both an energy dissipation mechanism, and (just as importantly), a theory must be developed explaining the generation of the Alfvén waves which also describes how those waves reach coronal heights.

Direct generation of Alfvén waves via photospheric processes is contentious, with many studies discussing the propensity with which these waves may be damped and/or reflected before crossing the transition region (Vranjes et al., 2008; Zaqarashvili et al., 2011a,b).

The FWRH for non-trapped waves originating in the photospheric  $p$ -mode wave field can lie many hundreds of km (or even on the order of several Mm) above the photosphere. Thus mode conversion may well overcome some of these difficulties, as much of the prohibitive photospheric physics does not inhibit the fast-Alfvén mode conversion at these chromospheric heights. It is therefore much easier for these resonantly generated waves to escape and reach the corona.

Active regions can exhibit significant twist at chromospheric heights which is why we have examined the fast-Alfvén conversion in this twisted field context. Although our model is fairly simple, the cold plasma approximation is reasonable in the low- $\beta$  chromosphere and the fact that we reproduce many of the properties of earlier studies suggests that the semi-analytic uniform twist field we have used is a reasonable approximation. Our results show that the conversion is extremely sensitive to the field inclination and wavevector-to-field attack angle of the fast waves at the FWRH. As such, sunspot fields may well be extremely effective at both generating the Alfvén waves and also filtering them, depending on the range of values of  $\phi$  and  $\theta$  that upcoming waves interact with.

In the future we would ideally like to see a MHS sunspot magnetic field atmosphere developed for use with fully numerical codes like SPARC. In this way a more thorough and realistic study of both fast-slow and fast-Alfvén conversion could be carried out, from photospheric to chromospheric heights. It would also be interesting to examine the effect that field twist may have on the generation of the acoustic halo, as well as other photospheric active region phenomena. Non-linear codes could also be employed to model fast shocks and non-linear counter-propagating Alfvén wave interactions in such field geometries.

# Bibliography

- Abramenko, V. I., Wang, T., & Yurchishin, V. B. 1996, *Sol. Phys.*, 168, 75
- Ascher, U., & Petzold, L. 1998, *Computer Methods for Ordinary Differential Equations and Differential-Algebraic Equations*. (SIAM Press)
- Aschwanden, M. J. 2003, *ArXiv Astrophysics e-prints*
- Aschwanden, M. J., de Pontieu, B., Schrijver, C. J., & Title, A. M. 2002, *Sol. Phys.*, 206, 99
- Asgari-Targhi, M., van Ballegooijen, A. A., Cranmer, S. R., & DeLuca, E. E. 2013, *ApJ*, 773, 111
- Avrett, E. H. 1981, in *The Physics of Sunspots*, ed. L. E. Cram & J. H. Thomas, 235–255
- Barnes, G., & Cally, P. S. 2001, *PASA*, 18, 243
- Basu, S., & Antia, H. M. 1997, *MNRAS*, 287, 189
- Beckers, J. M. 1969, *Sol. Phys.*, 9, 372
- Bellot Rubio, L. R. 2007, in *Highlights of Spanish Astrophysics IV*, ed. F. Figueras, J. M. Girart, M. Hernanz, & C. Jordi, 271
- Bellot Rubio, L. R., Balthasar, H., & Collados, M. 2004, *A&A*, 427, 319
- Bellot Rubio, L. R., Ruiz Cobo, B., & Collados, M. 1998, *ApJ*, 506, 805
- Berger, T. E., & Berdyugina, S. V. 2003, *ApJL*, 589, L117

## BIBLIOGRAPHY

---

- Berghmans, D., & Clette, F. 1999, *Sol. Phys.*, 186, 207
- Bharti, L., Jain, R., & Jaaffrey, S. N. A. 2007, *ApJ*, 665, L79
- Bogdan, T. J., & Cally, P. S. 1997, *Proceedings of the Royal Society of London Series A*, 453, 943
- Bogdan, T. J., Hindman, B. W., Cally, P. S., & Charbonneau, P. 1996, *ApJ*, 465, 406
- Borrero, J. M., & Ichimoto, K. 2011, *Living Reviews in Solar Physics*, 8, 4
- Braun, D. C. 1995, *ApJ*, 451, 859
- Braun, D. C., & Duvall, Jr., T. L. 1990, *Sol. Phys.*, 129, 83
- Braun, D. C., Duvall, Jr., T. L., & Labonte, B. J. 1987, *ApJL*, 319, L27
- . 1988, *ApJ*, 335, 1015
- Braun, D. C., Duvall, Jr., T. L., Labonte, B. J., Jefferies, S. M., Harvey, J. W., & Pomerantz, M. A. 1992a, *ApJL*, 391, L113
- Braun, D. C., Labonte, B. J., & Duvall, Jr., T. L. 1990, *ApJ*, 354, 372
- Braun, D. C., & Lindsey, C. 1999, *ApJL*, 513, L79
- Braun, D. C., Lindsey, C., Fan, Y., & Jefferies, S. M. 1992b, *ApJ*, 392, 739
- Brown, T. M., Bogdan, T. J., Lites, B. W., & Thomas, J. H. 1992, *ApJL*, 394, L65
- Brown, T. M., Christensen-Dalsgaard, J., Dziembowski, W. A., Goode, P., Gough, D. O., & Morrow, C. A. 1989, *ApJ*, 343, 526
- Browning, P. K. 1991, *Plasma Physics and Controlled Fusion*, 33, 539
- Cally, P. S. 2000, *Sol. Phys.*, 192, 395
- . 2006, *Royal Society of London Philosophical Transactions Series A*, 364, 333
- . 2007, *Astronomische Nachrichten*, 328, 286

- . 2009, *MNRAS*, 395, 1309
- Cally, P. S. 2011, in *Astronomical Society of India Conference Series*, Vol. 2, *Astronomical Society of India Conference Series*, 221–227
- Cally, P. S., & Andries, J. 2010, *Sol. Phys.*, 266, 17
- Cally, P. S., & Bogdan, T. J. 1993, *ApJ*, 402, 721
- . 1997, *ApJL*, 486, L67
- Cally, P. S., Bogdan, T. J., & Zweibel, E. G. 1994, *ApJ*, 437, 505
- Cally, P. S., Crouch, A. D., & Braun, D. C. 2003, *MNRAS*, 346, 381
- Cally, P. S., & Goossens, M. 2008, *Sol. Phys.*, 251, 251
- Cally, P. S., & Hansen, S. C. 2011, *ApJ*, 738, 119
- Cally, P. S., & Moradi, H. 2013, *MNRAS*, 435, 2589
- Charbonneau, P., Christensen-Dalsgaard, J., Henning, R., Larsen, R. M., Schou, J., Thompson, M. J., & Tomczyk, S. 1999, *ApJ*, 527, 445
- Chen, H.-R., Chou, D.-Y., Chang, H.-K., Sun, M.-T., Yeh, S.-J., LaBonte, B., & Team, t. T. 1998, *ApJL*, 501, L139
- Chou, D.-Y. 2000, *Sol. Phys.*, 192, 241
- Chou, D.-Y., Chang, H.-K., Sun, M.-T., LaBonte, B., Chen, H.-R., Yeh, S.-J., & Team, T. T. 1999, *ApJ*, 514, 979
- Christensen-Dalsgaard, J., Duvall, Jr., T. L., Gough, D. O., Harvey, J. W., & Rhodes, Jr., E. J. 1985, *Nature*, 315, 378
- Christensen-Dalsgaard, J., Gough, D. O., & Thompson, M. J. 1991, *ApJ*, 378, 413
- Christensen-Dalsgaard, J., et al. 1996, *Science*, 272, 1286
- Couvidat, S., Birch, A. C., & Kosovichev, A. G. 2006, *ApJ*, 640, 516

## BIBLIOGRAPHY

---

- Cranmer, S. R., & van Ballegooijen, A. A. 2005, *ApJS*, 156, 265
- Danielson, R. E. 1964, *ApJ*, 139, 45
- De Groof, A., & Goossens, M. 2000, *A&A*, 356, 724
- . 2002, *A&A*, 386, 691
- De Groof, A., Paes, K., & Goossens, M. 2002, *A&A*, 386, 681
- De Moortel, I., Ireland, J., & Walsh, R. W. 2000, *A&A*, 355, L23
- De Pontieu, B., Martens, P. C. H., & Hudson, H. S. 2001, *ApJ*, 558, 859
- Deubner, F.-L. 1975, *A&A*, 44, 371
- Donea, A.-C., Lindsey, C., & Braun, D. C. 2000, *Sol. Phys.*, 192, 321
- D’Silva, S. 1996, *ApJ*, 469, 964
- D’Silva, S., Duvall, Jr., T. L., Jefferies, S. M., & Harvey, J. W. 1996, *ApJ*, 471, 1030
- Duvall, Jr., T. L., Jefferies, S. M., Harvey, J. W., & Pomerantz, M. A. 1993, in *Bulletin of the American Astronomical Society*, Vol. 25, *Bulletin of the American Astronomical Society*, 1220
- Duvall, Jr., T. L., et al. 1997, *Sol. Phys.*, 170, 63
- Edwin, P. M., & Roberts, B. 1983, *Sol. Phys.*, 88, 179
- Erdélyi, R., & Fedun, V. 2007, *Science*, 318, 1572
- Evershed, J. 1909, *MNRAS*, 69, 454
- Fan, Y. 2004, *Living Reviews in Solar Physics*, 1, 1
- Felipe, T. 2012, *ApJ*, 758, 96
- Finsterle, W., Jefferies, S. M., Cacciani, A., Rapex, P., & McIntosh, S. W. 2004, *ApJL*, 613, L185
- Fleck, B., Couvidat, S., & Straus, T. 2011, *Sol. Phys.*, 271, 27

- Fossum, A., & Carlsson, M. 2005, *ApJ*, 625, 556
- Gizon, L., & Birch, A. C. 2005, *Living Reviews in Solar Physics*, 2, 6
- Gizon, L., et al. 2009, *SSR*, 144, 249
- Goldreich, P., & Keeley, D. A. 1977, *ApJ*, 212, 243
- Gonzalez Hernandez, I., Patron, J., Chou, D.-Y., & TON Team. 1998, *ApJ*, 501, 408
- Goossens, M., Andries, J., & Aschwanden, M. J. 2002, *A&A*, 394, L39
- Goossens, M., Terradas, J., Andries, J., Arregui, I., & Ballester, J. L. 2009, *A&A*, 503, 213
- Goossens, M., Van Doorselaere, T., Soler, R., & Verth, G. 2013, *ApJ*, 768, 191
- Grossmann-Doerth, U., Schmidt, W., & Schroeter, E. H. 1986, *A&A*, 156, 347
- Hale, G. E. 1908, *Contributions from the Mount Wilson Observatory / Carnegie Institution of Washington*, 30, 1
- . 1925, *PASP*, 37, 268
- . 1927, *Nature*, 119, 708
- Hanasoge, S., Birch, A., Gizon, L., & Tromp, J. 2012a, *Physical Review Letters*, 109, 101101
- Hanasoge, S. M. 2007, PhD thesis, Stanford University
- . 2009, *A&A*, 503, 595
- Hanasoge, S. M., Duvall, T. L., & Sreenivasan, K. R. 2012b, *Proceedings of the National Academy of Science*, 109, 11928
- Hanasoge, S. M., Duvall, Jr., T. L., & Couvidat, S. 2007, *ApJ*, 664, 1234
- Handy, B. N., et al. 1999, *Sol. Phys.*, 187, 229
- Hanson, C. S., Donea, A. C., & Leka, K. D. 2015, *Sol. Phys.*

## BIBLIOGRAPHY

---

- Hill, F. 1988, *ApJ*, 333, 996
- Hindman, B. W., & Brown, T. M. 1998, *ApJ*, 504, 1029
- Hirzberger, J., Bonet, J. A., Sobotka, M., Vázquez, M., & Hanslmeier, A. 2002, *A&A*, 383, 275
- Hood, A. W., Ruderman, M., Pascoe, D. J., De Moortel, I., Terradas, J., & Wright, A. N. 2013, *A&A*, 551, A39
- Ilonidis, S., Zhao, J., & Hartlep, T. 2013, *ApJ*, 777, 138
- Jacoutot, L., Kosovichev, A. G., Wray, A., & Mansour, N. N. 2008, *ApJL*, 684, L51
- Jahn, K. 1989, *A&A*, 222, 264
- Jahn, K., & Schmidt, H. U. 1994, *A&A*, 290, 295
- Jain, R., & Haber, D. 2002, *A&A*, 387, 1092
- Jensen, J. M. 2003, in *ESA Special Publication*, Vol. 517, GONG+ 2002. Local and Global Helioseismology: the Present and Future, ed. H. Sawaya-Lacoste, 61–70
- Jess, D. B., Mathioudakis, M., Erdélyi, R., Crockett, P. J., Keenan, F. P., & Christian, D. J. 2009, *Science*, 323, 1582
- Jess, D. B., Shelyag, S., Mathioudakis, M., Keys, P. H., Christian, D. J., & Keenan, F. P. 2012, *ApJ*, 746, 183
- Katsukawa, Y., Ichimoto, K., Sekii, T., Suematsu, Y., Tsuneta, S., Shine, R. A., & Tarbell, T. D. 2007, in *Astronomical Society of the Pacific Conference Series*, Vol. 369, *New Solar Physics with Solar-B Mission*, ed. K. Shibata, S. Nagata, & T. Sakurai, 43
- Khomenko, E., & Cally, P. S. 2012, *ApJ*, 746, 68
- Khomenko, E., & Collados, M. 2008, *ApJ*, 689, 1379
- . 2009, *A&A*, 506, L5

—. 2012, *ApJ*, 747, 87

Kontogiannis, I., Tsiropoula, G., & Tziotziou, K. 2014, *A&A*, 567, A62

Kosovichev, A. G. 2002, *Astronomische Nachrichten*, 323, 186

Kosugi, T., et al. 2007, *Sol. Phys.*, 243, 3

Krasnoselskikh, V., Vekstein, G., Hudson, H. S., Bale, S. D., & Abbett, W. P. 2010, *ApJ*, 724, 1542

Kuridze, D., Zaqarashvili, T. V., Shergelashvili, B. M., & Poedts, S. 2008, *Annales Geophysicae*, 26, 2983

Kurucz, R. 1993, *ATLAS9 Stellar Atmosphere Programs and 2 km/s grid*. Kurucz CD-ROM No. 13. Cambridge, Mass.: Smithsonian Astrophysical Observatory, 1993., 13

Ladenkov, O. V., Hill, F., Egamberdiev, S. A., & Chou, D. Y. 2002, *Astronomy Letters*, 28, 411

Leibacher, J. W., & Stein, R. F. 1971, *aplett*, 7, 191

Leighton, R. B., Noyes, R. W., & Simon, G. W. 1962, *ApJ*, 135, 474

Lemen, J. R., et al. 2012, *Sol. Phys.*, 275, 17

Lindsey, C., & Braun, D. C. 1990, *Sol. Phys.*, 126, 101

—. 2000, *Sol. Phys.*, 192, 261

Lindsey, C., Cally, P. S., & Rempel, M. 2010, *ApJ*, 719, 1144

Lites, B. W., Bida, T. A., & Scharmer, G. B. 1989, in *Bulletin of the American Astronomical Society*, Vol. 21, *Bulletin of the American Astronomical Society*, 854

Low, B. C. 1975, *ApJ*, 197, 251

—. 1980, *Sol. Phys.*, 67, 57

## BIBLIOGRAPHY

---

- Martens, P. C. H., Hurlburt, N. E., Title, A. M., & Acton, L. W. 1996, *ApJ*, 463, 372
- Meyer, F., Schmidt, H. U., & Weiss, N. O. 1977, *MNRAS*, 179, 741
- Moradi, H., & Cally, P. S. 2013, *Journal of Physics Conference Series*, 440, 012047
- . 2014, *ApjL*, 782, L26
- Moradi, H., Cally, P. S., Przybylski, D., & Shelyag, S. 2015, *MNRAS*, 449, 3074
- Moradi, H., et al. 2010, *Sol. Phys.*, 267, 1
- Moretti, P. F., Jefferies, S. M., Armstrong, J. D., & McIntosh, S. W. 2007, *A&A*, 471, 961
- Muglach, K. 2003, *A&A*, 401, 685
- Muglach, K., Hofmann, A., & Staude, J. 2005, *A&A*, 437, 1055
- Nagashima, K., et al. 2007, *PASJ*, 59, 631
- Nakagawa, Y., Raadu, M. A., Billings, D. E., & McNamara, D. 1971, *Sol. Phys.*, 19, 72
- Nakariakov, V. M., Ofman, L., Deluca, E. E., Roberts, B., & Davila, J. M. 1999, *Science*, 285, 862
- Nakariakov, V. M., & Verwichte, E. 2005, *Living Reviews in Solar Physics*, 2
- Narain, U., & Ulmschneider, P. 1996, *SSR*, 75, 453
- Neukirch, T., & Martens, P. C. H. 1998, *A&A*, 332, 1075
- Ofman, L., & Aschwanden, M. J. 2002, *ApJL*, 576, L153
- O'Shea, E., Banerjee, D., Doyle, J. G., Fleck, B., & Murtagh, F. 2001, *A&A*, 368, 1095
- Parchevsky, K. V., & Kosovichev, A. G. 2007, *ApJ*, 666, 547

- Pascoe, D. J., Hood, A. W., de Moortel, I., & Wright, A. N. 2012, *A&A*, 539, A37
- Pascoe, D. J., Wright, A. N., & De Moortel, I. 2011, *ApJ*, 731, 73
- Pevtsov, A. A., Canfield, R. C., & Metcalf, T. R. 1994, *ApJL*, 425, L117
- Pevtsov, A. A., Hagyard, M. J., Blehm, Z., Smith, J. E., Canfield, R. C., Sakurai, T., & Hagino, M. 2005, *Highlights of Astronomy*, 13, 140
- Pizzo, V. J. 1986, *ApJ*, 302, 785
- Priest, E. 1982, *Solar Magneto-hydrodynamics*. (D. Reidel Publishing)
- Przybylski, D., Shelyag, S., & Cally, P. S. 2015, *ApJ*, 807, 20
- Rajaguru, S. P., Couvidat, S., Sun, X., Hayashi, K., & Schunker, H. 2013, *Sol. Phys.*, 287, 107
- Reale, F. 2014, *Living Reviews in Solar Physics*, 11
- Rees, D. E., Durrant, C. J., & Murphy, G. A. 1989, *ApJ*, 339, 1093
- Rempel, M., & Schlichenmaier, R. 2011, *Living Reviews in Solar Physics*, 8, 3
- Rempel, M., Schüssler, M., & Knölker, M. 2009, *ApJ*, 691, 640
- Riethmüller, T. L., Solanki, S. K., & Lagg, A. 2008, *ApJL*, 678, L157
- Rijs, C., Moradi, H., Przybylski, D., & Cally, P. S. 2015, *ApJ*, 801, 27
- Rimmele, T. 2008, *ApJ*, 672, 684
- Rimmele, T. R. 2004, *ApJ*, 604, 906
- Roddi, F. 1975, *Academie des Sciences Paris Comptes Rendus Serie B Sciences Physiques*, 281, 93
- Roupe van der Voort, L., Bellot Rubio, L. R., & Ortiz, A. 2010, *ApJL*, 718, L78
- Ruedi, I., Solanki, S. K., Stenflo, J. O., Tarbell, T., & Scherrer, P. H. 1998, *A&A*, 335, L97

## BIBLIOGRAPHY

---

- Scharmer, G. B., Gudiksen, B. V., Kiselman, D., Löfdahl, M. G., & Rouppe van der Voort, L. H. M. 2002, *Nature*, 420, 151
- Scharmer, G. B., Henriques, V. M. J., Kiselman, D., & de la Cruz Rodríguez, J. 2011, *Science*, 333, 316
- Scherrer, P. H., et al. 1995, *Sol. Phys.*, 162, 129
- . 2012, *Sol. Phys.*, 275, 207
- Schlichenmaier, R., & Schmidt, W. 2000, *A&A*, 358, 1122
- Schlüter, A., & Temesváry, S. 1958, in *IAU Symposium*, Vol. 6, *Electromagnetic Phenomena in Cosmical Physics*, ed. B. Lehnert, 263
- Schrijver, C. J., Aschwanden, M. J., & Title, A. M. 2002, *Sol. Phys.*, 206, 69
- Schunker, H., & Braun, D. C. 2011, *Sol. Phys.*, 268, 349
- Schunker, H., & Cally, P. S. 2006, *MNRAS*, 372, 551
- Shelyag, S., Zharkov, S., Fedun, V., Erdélyi, R., & Thompson, M. J. 2009, *A&A*, 501, 735
- Simon, G. W., & Weiss, N. O. 1970, *Sol. Phys.*, 13, 85
- Simon, G. W., Weiss, N. O., & Nye, A. H. 1983, *Sol. Phys.*, 87, 65
- Sobotka, M., Bonet, J. A., & Vazquez, M. 1993, *ApJ*, 415, 832
- Socas-Navarro, H. 2005, *ApJL*, 631, L167
- Socas-Navarro, H., Martínez Pillet, V., Sobotka, M., & Vázquez, M. 2004, *ApJ*, 614, 448
- Solanki, S. K. 2003, *A&AR*, 11, 153
- Solanki, S. K., Walther, U., & Livingston, W. 1993, *A&A*, 277, 639
- Soler, R., Carbonell, M., Ballester, J. L., & Terradas, J. 2013, *ApJ*, 767, 171

- Spruit, H. C. 1976, *Sol. Phys.*, 50, 269
- , 1982, *Sol. Phys.*, 75, 3
- Spruit, H. C. 1991, in *Lecture Notes in Physics*, Berlin Springer Verlag, Vol. 388, Challenges to Theories of the Structure of Moderate-Mass Stars, ed. D. Gough & J. Toomre, 121–134
- Spruit, H. C., & Bogdan, T. J. 1992, *APJL*, 391, L109
- Stein, R. F., Lagerfjård, A., Nordlund, Å., & Georgobiani, D. 2012, in *Astronomical Society of the Pacific Conference Series*, Vol. 462, Progress in Solar/Stellar Physics with Helio- and Asteroseismology, ed. H. Shibahashi, M. Takata, & A. E. Lynas-Gray, 345
- Stenflo, J. O. 1971, in *IAU Symposium*, Vol. 43, Solar Magnetic Fields, ed. R. Howard, 101
- Terradas, J., Goossens, M., & Verth, G. 2010, *A&A*, 524, A23
- Thomas, J. H., & Stanchfield, II, D. C. H. 2000, *ApJ*, 537, 1086
- Thomas, J. H., Weiss, N. O., Tobias, S. M., & Brummell, N. H. 2006, *A&A*, 452, 1089
- Title, A. M., Frank, Z. A., Shine, R. A., Tarbell, T. D., Topka, K. P., Scharmer, G., & Schmidt, W. 1993, *ApJ*, 403, 780
- Tiwari, S. K., Venkatakrisnan, P., & Sankarasubramanian, K. 2009, *ApJL*, 702, L133
- Tomczyk, S., & McIntosh, S. W. 2009, *ApJ*, 697, 1384
- Tomczyk, S., McIntosh, S. W., Keil, S. L., Judge, P. G., Schad, T., Seeley, D. H., & Edmondson, J. 2007, *AGU Fall Meeting Abstracts*
- Toner, C. G., & Labonte, B. J. 1993, *ApJ*, 415, 847
- Tritschler, A., Schlichenmaier, R., Bellot Rubio, L. R., KAOS Team, Berkefeld, T., & Schelenz, T. 2004, *A&Aj*, 415, 717

## BIBLIOGRAPHY

---

- Tritschler, A., & Schmidt, W. 1997, *A&A*, 321, 643
- Tsap, Y. T., Stepanov, A. V., & Kopylova, Y. G. 2011, *Sol. Phys.*, 270, 205
- Ulrich, R. K. 1970, *ApJ*, 162, 993
- van Ballegooijen, A. A., & Asgari-Targhi, M. 2016, *ApJ*, 821, 106
- van Ballegooijen, A. A., Asgari-Targhi, M., Cranmer, S. R., & DeLuca, E. E. 2011, *ApJ*, 736, 3
- Van Doorselaere, T., Andries, J., Poedts, S., & Goossens, M. 2004, *ApJ*, 606, 1223
- Van Doorselaere, T., Nakariakov, V. M., & Verwichte, E. 2008, *ApJL*, 676, L73
- Vernazza, J. E., Avrett, E. H., & Loeser, R. 1976, *ApJS*, 30, 1
- . 1981, *ApJS*, 45, 635
- Verth, G., Terradas, J., & Goossens, M. 2010, *ApJL*, 718, L102
- Vranjes, J., Poedts, S., Pandey, B. P., & de Pontieu, B. 2008, *A&A*, 478, 553
- Weiss, N. O., Thomas, J. H., Brummell, N. H., & Tobias, S. M. 2004, *ApJ*, 600, 1073
- Wiegelmann, T., & Sakurai, T. 2012, *Living Reviews in Solar Physics*, 9
- Wiehr, E., & Degenhardt, D. 1993, *A&A*, 278, 584
- Woodard, M. F. 2016, *MNRAS*, 460, 3292
- Zaqarashvili, T. V., Khodachenko, M. L., & Rucker, H. O. 2011a, *A&A*, 534, A93
- . 2011b, *A&A*, 529, A82
- Zharkov, S., Shelyag, S., Fedun, V., Erdélyi, R., & Thompson, M. J. 2009, *ArXiv e-prints*
- Zirker, J. B. 1993, *Sol. Phys.*, 148, 43